MIXING AND SAMPLING IN A MICROFLUIDIC CHANNEL USING ROTATING MAGNETIC MICROBEADS

A Dissertation
Presented to
The Academic Faculty

by

Drew Owen

In Partial Fulfillment
of the Requirements for the Degree
Doctor of Philosophy in the
George W. Woodruff School of Mechanical Engineering

Georgia Institute of Technology
August 2016

MIXING AND SAMPLING IN A MICROFLUIDIC CHANNEL USING ROTATING MAGNETIC MICROBEADS

Approved by:

Dr. Peter Hesketh, Advisor
School of Mechanical Engineering
Georgia Institute of Technology

Dr. Hang Lu
School of Chemical and Biomolecular Engineering
Georgia Institute of Technology

Dr. Alexander Alexeev
School of Mechanical Engineering
Georgia Institute of Technology

Dr. Todd Sulchek
School of Mechanical Engineering
Georgia Institute of Technology

Dr. J. Brandon Dixon
School of Mechanical Engineering
Georgia Institute of Technology

Date Approved: May 05, 2016

To Boss, Poppa Owen, Grandma Owen, Pop Cook, Grandma Lil, Uncle Bobby, Kayler, and Kimani

ACKNOWLEDGEMENTS

I would like to thank my advisor and the members of my committee for the advice and guidance in bringing this work to fruition. I would like to thank Srinivas Kumar Hanasoge Gowaranga for tremendous assistance in overcoming obstacles in the creation of this device. I also extend thanks to Matthew Ballard for his work in modeling of this system created here. His modeling work was crucial for understanding and visualizing the fluid behavior exhibited by this device. I wish to thank Drs. Todd Sulchek and David Hu for the loan of their high speed cameras that were used in some of the experiments described in this work. I also must thank the Georgia Tech Institute for Electronics and Nanotechnology, specifically Charlie Suh, for the patience and help in developing the microfabrication protocols needed in this work. I must thank Dr. Ben Haaland of the School of Industrial and Systems Engineering of Georgia Tech for taking time out of his schedule to provide some guidance in the performance of the statistical analysis of my data.

TABLE OF CONTENTS

LIST OF TABLES

LIST OF FIGURES

LIST OF SYMBOLS AND ABBREVIATIONS

Re	Reynolds Number
ρ	density
μ	dynamic viscosity
LoC	lab on a chip
DNA	deoxyribose nucleic acid
AC	alternating current
DEP	dielectrophoresis
LED	light emitting diode
UV	ultraviolet
CTC	circulating tumor cells
NiFe	permalloy, an alloy of nickel and iron
rpm	revolutions per minute
NdFeB	neodymium-iron-boron, a permanent magnet material
DC	direct current
PDMS	poly-dimethylsiloxane
EOF	electro-osmotic flow
BSA	bovine serum albumen
B	magnetic flux density
H	magnetic field strength
EOF	electro-osmotic flow
e-beam	electron beam
SEM	scanning electron microscopy
EDS	energy dispersive X-ray spectroscopy

PECVD	plasma enhanced chemical vapor deposition
CVD	chemical vapor deposition
SE	standard error
SD	standard deviation
n	number of measured events
U_x	linear velocity of bulk fluid flow
V_b	linear velocity of magnetic bead
u	ratio of bulk fluid velocity to magnetic bead velocity
CCD	charge coupled device
θ_i	fluorescent intensity
CCD	charge coupled device
$\bar{\theta}$	average fluorescent intensity
h	ratio of diameter of magnetic bead to height of microfluidic channel
AFM	atomic force microscopy
CCD	charge coupled device

SUMMARY

This work presents a novel microsystem utilizing an array of rotating magnetic beads inside a microfluidic channel. The magnetic beads are actuated via an external rotating magnetic field dynamically magnetizing small (<10 μm) soft magnetic features. Presented here is the method for fabricating the soft magnetic features via electron beam evaporation. The physical operational limits of the device are demonstrated and quantified. The effectiveness of this system is experimentally evaluated in two separate common microfluidic operations, microfluidic mixing and particle capture or isolation. The hypothesis of the work is that the actuation of the magnetic beads will rapidly mix the system and the rapid mixing will increase the chance that a functionalized target particle will come into contact with the magnetic bead. The target could then be trapped via a protein-protein bond with the functionalization on the magnetic bead. The first operation, microfluidic mixing, is the ability for these beads to mix fluids inside a microfluidic channel. This is done by measuring the mixing of two streams of fluid as they flow over the rotating array of beads. This method demonstrated significant mixing (65%) in less than 300 μm of channel length if the magnetic beads are actuated at a high enough velocity relative to the bulk flow velocity. The second operation is the capacity to capture particles from the microfluidic channel. This capturing is accomplished via protein-protein bond between the surface functionalizations of the magnetic bead and the particle. This device demonstrated the capacity to capture >80% of particles that pass through the 400 μm array. This result was demonstrated in channels where the magnetic beads occupied less than 25% of the channel height.

CHAPTER 1

INTRODUCTION

Microfluidics & Lab on a Chip

Large scale fluid flow is a concept understood by the even the non-technical population. It is an easily observed phenomenon, whether pouring honey into a cup of tea or then stirring the tea to mix the two fluids. The concept of fluid flowing through a pipe is an easily observable phenomenon and as such a surface level understanding is available to all. Flow through macro-scale pipes are often characterized by their turbulent nature. However, if the size of the pipe is sufficiently small the fluid loses the turbulent behavior. The turbulent behavior is predicted by examining the Reynolds number (Re) of the fluid

$$Re = \frac{\rho V D}{\mu}$$

Where ρ is the density of the fluid, μ is the dynamic viscosity of the fluid, V is the average velocity of the fluid and D is the diameter of the pipe. The Re number essentially represents a ratio of the inertial force of the fluid, the numerator, to the viscous force in the fluid, the denominator. Typically when the Re of a liquid is very large it is because the numerator is very large. This is because the viscosity of the fluid is a property that while dependent on temperature, typically varies very little. Macro-scale flow, with its turbulent flow behavior is characterized by a large Re number.

As the Re number decreases, the flow becomes less and less turbulent. When Re < 2300 in most pipes, the flow begins to lose its turbulent behavior and is described as laminar flow.

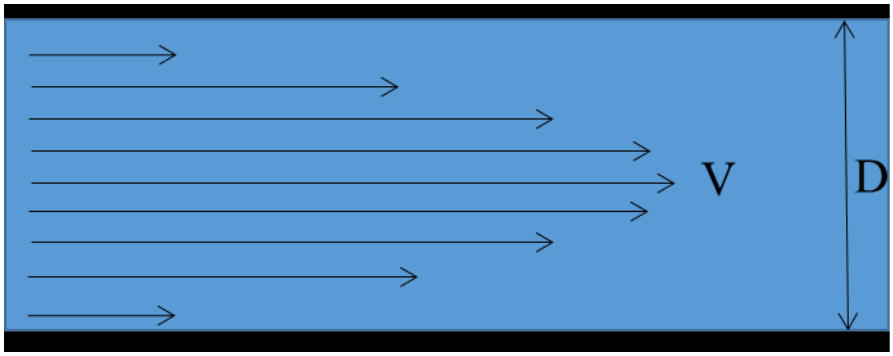

Figure 1.1 Laminar flow is characterized by minimal bending of streanlines. Fluid particles experience no lateral movement in a straight channel except through diffusion or browninan motion. This flow is highly predictable and in the case of low Re flows even reversible if there is no diffusion or brownian motion.

In laminar flow, all fluid particles travel along the path dictated by the fluid particle directly in front of it. This fluid flow is predictable and easily controlled and as such is useful for many laboratory processes. It is possible to achieve Re < 1 in flows by using high viscosity fluids like glycerol in macro-scale flow conditions, however the flow rates and pressures associated with such fluids makes their use impractical.

An alternative method to achieving Re < 1 is to decrease the numerator by either decreasing the velocity of the fluid or decreasing the diameter of the flow pipe. The latter method is referred to as microfluidics. This name derives from the fact that if the channel dimensions are on the order of micrometers, even a low viscosity fluid like water will exhibit this controlled laminar flow. The field of microfluidics is exciting for a number of reasons. First, low Re flow is very predictable and controllable and because of this can be used to essentially automate fluid processes. Individual control and monitoring of the fluid is not required because unless there is some outside aberration, the fluid will behave in the same manner at each step of the microchannel. Second, the small nature of the channel makes it portable and easily integrated with multiple microfluidic systems. These two reasons take together have given rise to the term lab on a chip (LoC), and much of the work in microfluidics has been to develop LoC tools and expand its application. The goal of LoC work is miniaturization of full laboratory processes onto a small, portable

and reliable system. Much work has been put into developing LoC technologies. This has included work in developing new materials and fabrication technologies as well as new methods for manipulating fluids inside microfluidic channels. This dissertation has studied the capacity of a new method for manipulating a fluid inside a microfluidic channel via actuation of magnetic microbeads. The manipulation studied in this work is the capacity to mix a fluid inside a microfluidic channel and the capacity to capture or isolate targets from the fluid. The remaining portion of this chapter will discuss some of the common uses of magnetic microbeads and address some already established LoC techniques to mix fluids and capture targets.

Magnetic Beads

In parallel development to the work done in LoC development, was the work to develop nanoparticles and nanomaterials. Of particular interest was a class of ferromagnetic nanoparticles. These nanoparticles could be left as individual nanoparticles or combined with a non-magnetic matrix such as latex, polystyrene or another inert polymer material. The incorporation of the non-magnetic matrix creates larger magnetic beads that exhibit superparamagnetic behavior. This superparamagnetic behavior is very useful for manipulation of samples in microfluidic systems. The superparamagnetic nature of the beads allows them to exhibit behavior between ferromagnetic materials paramagnetic materials. Ferromagnetic materials become strongly magnetized in the presence of a magnetic field, so much so that magnetization may persist after removal of the magnetic field. Paramagnetic materials become weakly magnetized in the presence of a magnetic field. The magnetization of paramagnetic materials aligns with the external magnetic field, creating an attraction between the external field and the induced paramagnetic material, in contrast to diamagnetic material which aligns to repel the external magnetic field. When the external magnetic field is removed, a paramagnetic material retains no residual magnetization. Superparamagnetic materials retain the strong

magnetization in an external magnetic field but retain zero magnetization in the absence of the magnetic field. This superparamagnetic behavior of magnetic beads makes them extremely useful because the beads can be manipulated independent of microfluidic, chemical, biological or inertial forces via magnetic forces. An additional benefit is that this manipulation can be activated independently by either engaging or removing the external magnetic field. The nature of the magnetic field can also play a role in the use of magnetic beads. A stationary magnetic field can be used to immobilize magnetic beads while a dynamic magnetic field can be used to actuate the magnetic beads, inducing either translation or rotation.

The polymer coating on magnetic beads allow for great versatility in surface modification, including roughness, hydrophilicity, surface charge, surface energy, reactivity or biocompatibility. The most common use for magnetic beads involves functionalizing the surface of the magnetic bead with a biomolecular marker that binds to a target. After the target has been bound to the magnetic bead, the target can then be indirectly manipulated via the magnetic bead. This opens up many potential applications for microscale manipulation of biological samples. Magnetic beads can be coated with antibodies to provide cell-specific targeting and manipulation.[1] The low interaction between the cell and the magnetic field makes it a safe and gentle alternative to cell manipulation via pressure controlled pipet tips. Coated magnetic beads have also been used for purification of DNA.[2]

Metals like Pt and Pd are often used as catalysts for fine chemical production or fuel cell applications yet no effective standard technique has been found for recovery of these precious metal catalysts following reactions.[3-5] Ruffert et al. demonstrated a technique using functionalized magnetic beads to recover platinum-conjugated metal nanoparticles.[6]

Microfluidic Mixing

Microfluidics and lab-on-a-chip techniques have made significant impacts in fields from medical diagnostics to chemical industries to reduce reagent cost, decrease processing and increase portability.[7-9] However, mixing is much more difficult in the low Reynolds number flow conditions experienced in microfluidic systems than in a typical larger-scale chemical laboratory setting. Thus, in order to avoid the need to rely on molecular diffusion for microfluidic mixing, a variety of passive and active mixers have been proposed.

Passive mixers enhance mixing by stretching and folding fluid interfaces to decrease the distance over which diffusion must act. However, this stretching and folding can require extensive channel lengths. Stroock et al. achieved mixing using a device utilizing staggered herringbone shaped ridges patterned into the top of microchannel so as to create chaotic flow patterns that fold the fluid into thin laminae and thus to effectively mix fluid streams.[10]

However, such a device required 500 mm or more to achieve strong mixing.[10] Other systems make use of bending the channel either in two or three dimensions but these systems still require footprints of a few millimeters to achieve significant mixing.[11-13]

Other systems make use of side channels that remove a small portion of the fluid and reintroduce it downstream to the main channel to redistribute fluid across the main channel. [14, 15] In this way a portion of the fluid is essentially transported a different region of the flow and decreasing the distance over which diffusion must occur.

All of these passive mixers rely upon fluid flow through the channel to generate mixing and thus mixing and flow rate cannot be controlled independently in real-time on the device. Increasing or decreasing the volumetric throughput of the system will alter the residence time of the fluid mixer and by extension alter the amount of mixing due to diffusion. In either case, the fluid will still achieve the same amount of folding of the fluid. If a passive mixers performance needs to be tuned independent of volumetric

throughput, it can only be done by altering the entire geometry of the system and thus fabricating an entirely new system.

Active mixers expend energy into the system to perturb the fluid and accelerate diffusion. These systems typically involve some sort of dynamic actuation either of the pumping of the system or of a transducer. This active perturbation often leaves these systems with a greater degree of complexity than passive mixers but also achieve significant mixing more rapidly.[16] Lin et al. demonstrated mixing in 1 mm by utilizing a switching pumping system operating at 1Hz between two separate reservoirs in a T-shaped microfluidic channel.[17]

This system introduces mixing creating either plug flows that can mix via diffusion or at high enough frequencies by creating sufficient force from the collision of the two fluids together to generate wave-like pattern at the interface between the two fluids that aids in mixing. This added force also represents kinetic energy added to the fluids, aiding in diffusion. Additionally, the stop and start nature of the flows make it difficult to integrate into a continuous flow system. A similar concept was presented by Niu and Lee using side channels to alternate pumping into a single main channel also containing two fluids.[18]

Here the energy added to the system is the pumping of from the side channels generating force inside the channel to accelerate mixing. However, this system still required at least 3mm of channel length to achieve strong mixing with small proteins. Campisi et al. demonstrated an electrokinetic micromixer utilizing AC osmosis and dielectrophoretic (DEP) force to induce chaotic flows in the a microfluidic channel.[19]

This system creates similar flows to that developed by Stroock et al.[10] While this system does allow for independent control of flow rate and mixing, the use of chaotic flows requires 5mm of channel length to achieve mixing. Further, the use of DEP precludes the use of many common buffers used in biological studies. The high salt concentration of common buffers interferes or blocks the DEP effect.

Several studies have investigated utilizing sonic and ultrasonic transducers which can be actuated externally to the microfluidic channel or a microfluidic chamber. Mixing has also been achieved in very short channel lengths, sub millimeter lengths, using ultrasonic actuation. However, this method increased the fluid temperature by 15 ^{0}C, and is thus incompatible with many biological or chemical applications where heating can be deleterious to the sample integrity by either killing cells, denaturing proteins or altering chemical reaction rates.[20-22]

More recent work has demonstrated mixing induced by LED illumination which overcomes heating problems but still requires a few millimeters to achieve even 50% mixing.[23] Additionally, the system requires a sheath oil flow to surround the UV sensitive aqueous phase to keep it intact prior to UV exposure. Thus after the mixing has begun the system cannot return to a baseline state.

Microfluidic Capture

Cell sorting, capture and isolation are important steps in biology, biotechnology and medicine. This is typically done to extract target cells that represent a small portion of the total cell population in a sample. The application of this cell isolation is used in both therapeutic and diagnostic practices. A therapeutic example would be the extraction and enrichment of hematopoietic stem cells for autologous cell therapies.[24] An example of a diagnostic application for cell isolation would be the capture of circulating tumor cells (CTCs) from blood. Many commercial cell sorters however have several significant limitations. First, high operation pressures could damage or kill cell samples. This poses a problem for isolating and growing new cell lines. The killing of cells is also a problem for analysis of live versus dead cells. This is especially important for food safety testing. Bacteria and pathogens will naturally tend to grow on food but common treatments of food during processing are designed to kill those potential sources of illness. A dead bacterium on the surface of a leaf of spinach is not a danger to consumers,

but a live bacterium could lead to illness or death. Thus being able to isolate cells without damaging them is very important. Another major issue in commercial cell isolation systems is the large instrumentation packages they require. This large and bulky instrumentation require a full laboratory set-up with a significant investment in money and space. These large requirements limit the availability of this cellular tool to only large centralized facilities, decreasing widespread potential use. This significant instrumentation also diminishes the use of cell isolation in point-of-care situations. Finally the capture and isolation of cells often requires pre-labeling of the cells with fluorescent markers. In situations with very low target cell concentrations, like the case of CTCs or bacteria from food safety samples this could prove difficult to guarantee all of the target population is labeled. Microfluidics offers a potential solution to the bulky nature of commercial cell isolation systems. Microfluidics offers precise spatial and temporal control via low Re flows. The miniaturization of microfluidics brings down financial costs and opens up the technique to more point-of-care applications.

One popular method for capturing and isolating cells from a fluid is to utilize size exclusionary principles. This works well if the size of the target is extreme when compared to its medium. This is also an attractive option if the target cell properties are not well understood or if a strong biomarker for the cell is not available. This technique has seen many versions. Early methods used variations on a filter system to capture and isolate cells.[25]

These variations involved pumping cells directly into a membrane that would act like a sieve to remove larger particles. These methods were limited by the filter system clogging over time, as items larger than the filter size would accumulate at surface. This could lead to clogging problems over time. The introduction of the cross flow-system, where a flow lateral to the bulk flow is used to separate materials helps to reduce clogging. In either case, a separate step is often required to clean or separate the trapped

cells from the filter. Davis et al. demonstrated modified method using an offset pillar design.[26]

This offset pillar design created preferential paths based on particle size and allowed for continuous flow separation without the need to separate cells from a filter system. Newer systems have built upon the principle of separation via physical parameters. Godin et al. presented a system to identify and separate out cells based on mass.[26] Wang et al. demonstrated a microfluidic system to separate cells based upon stiffness.[27]

Another group of cell isolation systems seek to use the controlled and stable physics of microfluidics to separate out cell populations. These systems still utilize size to separate cells from bulk fluids but do so without out the use of a filtering structure and instead relies on interactions between fluid forces and the size of the object. Kuntaegowdanahalli et al demonstrated this technique using a spiral separator.[28]

This spiral channel separates particles via the interaction between the Dean drag force and the inertial lift force and the ratio of these varies with the third power of particle diameter. The interaction between the size of the particles and the gradient of linear flow velocity across the channel due to the circular nature of the channel causes different sized particles to find a streamline that balances the two forces. Thus, similarly sized particles form a single line in the channel, which allows for easy and controlled separation by simple splitting the flow. The technique was demonstrated able to separate two cell types with 80% efficiency. A technique utilizing a similar principle was demonstrated by Lin et al. utilizing sheath flows.[29] Lin et al. were able to separate particles by shrinking the sample stream with a sheath flow.

The sample stream was constricted to smaller than the diameter of one of the particle types, inducing that particle to leave the sample stream and enter the sheath flow. A listed limitation of the system was an inability to create a smaller sample stream than

2-3 μm, thus limiting the size of particle separation. Wu et al. demonstrated alternative method utilizing sheath flow and sudden expansions to separate cells.[30]

This technique utilized a sheath flow to collapse the entire cell population into a narrow stream and followed by a sudden expansion in channel width. The lower inertia, smaller cells then migrated close to the suddenly wider wall, while the larger, higher inertia cells saw a less pronounced alteration of their path and formed a separate stream.

While size and other physically based separation systems are compatible with cell separations, they are not always applicable. In the case of Salmonella bacteria, only select strains of the bacteria actually cause illness. Some strains cause no harmful effects whatsoever. For food safety applications, the only concern is the presence of the harmful Salmonella so a size or shape exclusionary system would still capture the non-harmful bacteria and require further strain specific sorting. However, to complement the physical parameter basis for sorting, biological targets such as cells, viruses and proteins can also be sorted by utilizing immunochemistry. These methods rely on anti-sera to biological targets, similar to antibody-antigen or protein-protein binding. Much of this work involves seeding a protein to a structure inside a microfluidic channel and then flowing cells over the structure to capture or extract cells and DNA.[31-34] More recent innovative work has sought to combine magnetic microbeads with this functionalization chemistry. The biochemistry for functionalizing magnetic beads is so well established that multiple companies exist to provide pre-functionalized beads. These magnetic properties of the beads allow them to be easily manipulated inside a microfluidic device. This is particularly useful for sorting cells that have been labeled with a magnetic bead. Kang et al. utilized side channels to collect CTCs that have been labeled with magnetic beads.[35]

The principle of this device is similar to that of a cross-flow system, only instead of the trapped cells being sorted according to size exclusion; cells bound to magnetic beads are pulled by the magnetic field. Cells not bound to a magnetic bead would

experience no pull towards the side chambers. Karabacak integrated this magnetic separation principle downstream of an offset micropillar design to achieve a two stage separation.[36]

Both of these systems however rely on macro-scale laboratory setups to pre-label the target cells with the magnetic beads. It would be ideal to integrate this step on chip to reduce costs and increase portability. Some work has been done to address this. Liu et al. used an array of magnetized nickel micropillars to hold a sheet of magnetic beads in place before flowing cells over the array of magnetic beads. [37]. The beads are held in place by magnetic attraction to the nickel micropillars. The nickel micropillars are magnetized by an external magnetic field. Ideally all of the cells pumped through the system become bound to the magnetic beads. Removal of the magnetic field demagnetizes the micropillar and magnetic beads bound to the cells. The magnetic beads and magnetic beads bound to cells can then be pumped downstream for separation.

Further developing the concept of magnetic beads as a filter system, Saliba et al. utilized a small piece of magnetic material to anchor a chain of the magnetic beads using a vertically oriented magnetic field.[38] Here the need for the magnetic micropillar is removed and replaced by the self-aligned beads.

This effectively extends the reach magnetic beads beyond the floor of the channel. These are strong improvement over stationary micropillars or filters, as the beads can be de-magnetized and collected or sorted downstream. However, neither the system presented by Liu et al. or Saliba et al. completely address the issue of pre-labeling or capturing cells with magnetic beads on chip. The Liu et al. system only affects a minor portion of the total channel volume, increasing the required residence time to guarantee all cells are captured. The Saliba et al. system relies on the magnetic field interactions between the beads to maintain the pillar but could run into issues with bulk flow or particles in the bulk flow displacing beads from the pillar. Both systems require a capture region of at least 5mm in length to capture efficiently.[37, 38]

Summary

Microfluidic mixing falls into two groups: passive mixing and active mixing. Passive mixing folds the fluid over long channel lengths, and in such devices, mixing cannot be actuated independent of fluid flow. While these passive mixers are easily integrated into a microfluidic system, they are not easily tuned on chip to achieve the goal performance. Additionally, passive mixers require longer channels to achieve significant mixing.[39, 40] Active mixers typically use dynamic actuation of either the pumping of the fluid or of a transducer inside the microfluidic channel. This increases the complexity of the system but can achieve more rapid mixing than passive micromixers and can be tuned and actuated on chip independent of volumetric flow rate. Further the added complexity often has difficulty integrating with biological and sensitive chemical applications. The DEP and EOF pumping systems are not compatible with common biological buffers. The temperature increase experienced by acoustic transducer based systems make them incompatible with live cells, proteins and some chemical reactions. Therefore, there is still a gap in available microfluidic mixing technologies for a system that achieve rapid mixing in a short channel length that is also compatible with sensitive biological or chemical samples.

Particle isolation/sorting/capture technologies typically either utilize physical parameters such as size, shape, stiffness, etc. These systems exploit the well-controlled physics of microfluidics to manipulate particles or cells. However, these systems run into issues when sorting or isolating biologically different but similarly sized populations of cells. This has led to work to separate target cells utilizing antigen-antibody specific immunochemistry. Further, work has been done on separating cell populations using antibodies functionalized on the surface of magnetic beads. The antibody provides specific targeting while the magnetic bead allows for manipulation of the cell via magnetic forces. Significant work has been done to isolate cells via this indirect magnetic

manipulation but less work has been done to address how the magnetic beads become bound to the cell. The lack of description in the literature likely means the magnetic beads are attached to the target cells via incubation in a system that is not a portion of the microfluidic system described. The few systems that do attempt to bind a magnetic bead to a target cell on chip typically do so utilizing a passive system where the cell must randomly collide with a stationary bead. The low Re nature of microfluidic systems makes the likelihood of this occurrence low and as such requires larger channel lengths and residence times. Thus there is still a gap in available technologies to rapidly bind target cells to magnetic beads for cell capture/sorting/isolation applications. This work seeks to address the gaps described in microfluidic mixing and microfluidic cell capture/sorting/isolation technologies. The central hypothesis of this work is that actuating magnetic beads inside a microfluidic channel will produce significant mixing and this increase in mixing will increase the chances of a target to come into contact with the magnetic bead and thus increase the chances of the target binding to the cell via a ligand-ligand bond. The aims of this work are to develop an actuated magnetic bead system for systematic testing of the operating parameters, quantify the effectiveness of the system to mix in a microfluidic channel and quantify the effectiveness of this system to capture targets from a microfluidic channel via a ligand-ligand bond

CHAPTER 2

DEVICE DESCRIPTION

The fundamental feature of this device is the actuation of an array of magnetic beads inside a microfluidic channel. The method of actuation utilized is orbiting around a fixed location. The orbit of these microbeads is created by use of an external magnetic field coupled with microfabricated soft magnetic features. When in the presence of a permanent magnetic field, the magnetic features develop poles, regions concentrating the external magnetic field lines. The magnetic microbeads are superparamagnetic and become magnetized in the presence of the magnet field and are attracted to the poles of the magnetic features.

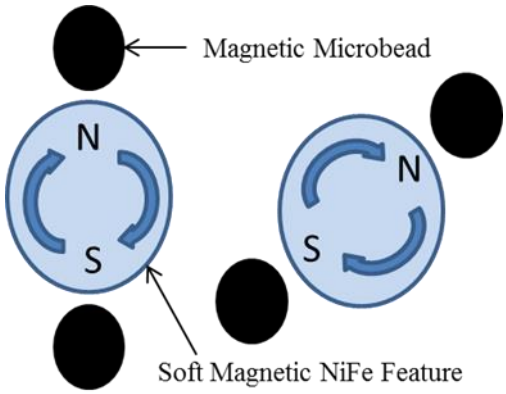

Figure 2.1 The external magnetic field magnetizes the soft magnetic feature creating magnetic poles in the feature. Magnetic beads are attracted to the poles as regions of high magnetic field gradient. If the magnetic field lines change the induced poles in the magnetic feature realign to match the field lines and the magnetic bead is pulled via magnetic attraction to the location of the new induced pole.

If the external magnetic field lines are rotated, the locations of these poles in the magnetic features rotate along with the external magnetic field. This rotation then pulls the magnetic beads, as the force of magnetic attraction will pull the bead continuously to

the new pole location. This force of magnetic attraction between the magnetic bead and the NiFe disc was indirectly measured to be approximately 1 nN (see Chapter 4). The path taken by the bead is specified by the perimeter of the magnetic feature.

The external magnet field is created by a permanent magnet attached to the shaft of a small motor. The motor used in these experiments was a stepper motor, Nanotec DB42, with a separate motor controller, Nanotec SMC136. Use of a stepper motor allowed for accurate and precise control of the magnetic field angular velocity over a wide range of motor speeds, 50 rpm to 4000 rpm. The motor is held in a custom machined mount that attaches to the back of the microscope.

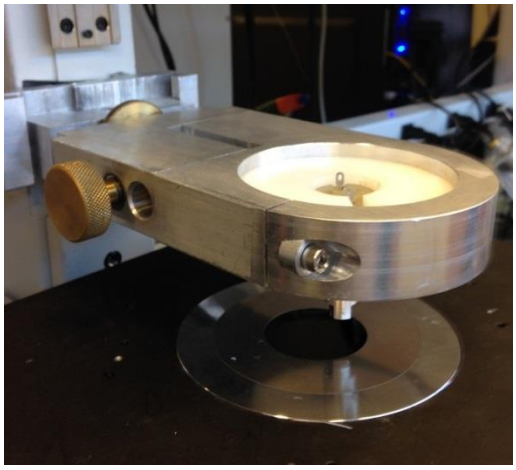

Figure 2.2 Custom motor mount allows for three axis control of motor and magnet position. The attachment to the rear of the stage minimizes vibrations to the stage at high motor frequencies. The overhanging magnet requires use of an inverted microscope to image the functioning device.

Attachment to the back rather than directly to the stage reduces vibration in the stage, improving image capture quality. This mount also contained thumb screws to allow for three axis control of the motor and magnet position in relation to the NiFe discs.

The magnetic field used in this work is created by permanent magnets. The magnets used are NdFeB, grade N52 (B444-N52 from K&J Magnetics). The magnets are cubes with 6.35mm along each edge and have a nickel finish (Figure. The measured

magnetic field at the surface of the magnet was 0.24 T. The magnetic field was measured by a DC magnetometer. The magnet was held in place by a custom machined aluminum fixture that would slip fit onto the shaft of the motor.

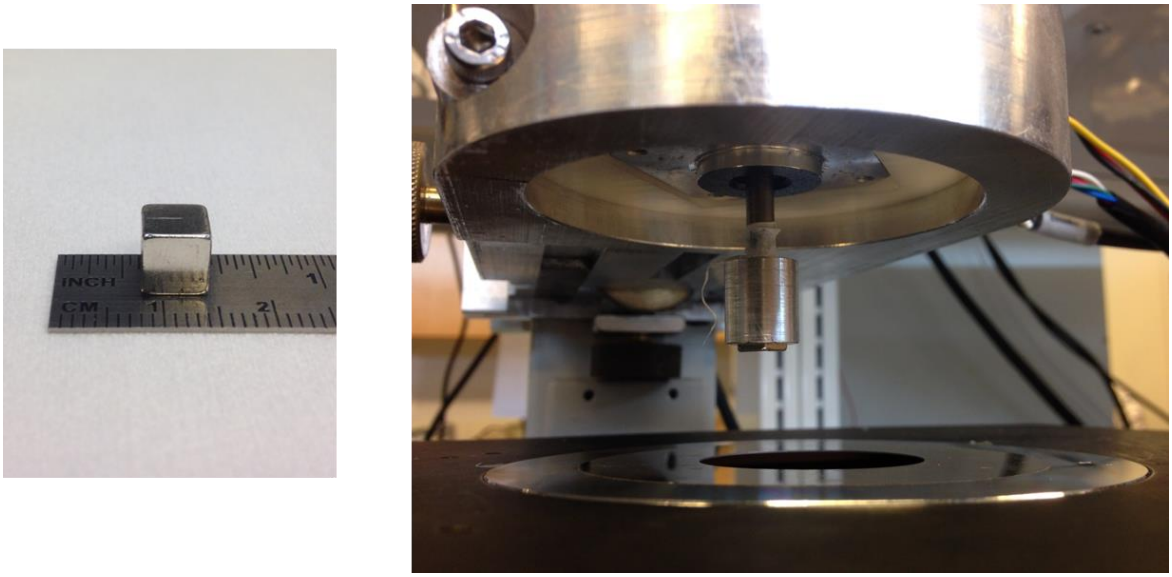

Figure 2.3 Left- image of magnet used in experiments, Right- placement of magnet in aluminum mount attached to motor shaft. Teflon tape is wrapped around the shaft to insure a tight fit with mount.

The magnetic microbeads used in these experiments are Dynabeads M-280 (Thermo-Fisher Scientific) with a surface functionalization of streptavidin. The beads are 2.8μm in diameter and have an iron oxide core with a polystyrene shell. The iron oxide core makes these beads superparamagnetic, meaning they become strongly magnetic in the presence of an external magnetic field. The fluorescent particles used in these experiments are Fluorspheres (Thermo-Fisher Scientific). Two different types of Fluorspheres were used for these experiments. For mixing experiments, the Fluorspheres were 40nm in diameter. These particles were chosen because the concentration of these particles is high enough to appear as a monochromatic stream of fluid while the particle size limits diffusion at the interface. This makes the degree of mixing easier to quantify. For capture experiments, 1.0μm diameter Fluorspheres with a surface functionalization of

biotin was used. These particles are approximately the same size as a prokaryotic cell. The streptavidin on the M-280 and the biotin on the Fluorsphere mimic the binding of an antibody to an antigen. Both the Dynabeads and Fluorspheres are commercially available with functionalization from Life Technologies, formerly Invitrogen.

Microfluidic Channel

The initial design of the PDMS microfluidic channel mold utilized a single main channel. This main channel connected on one end to a single outlet and on the other end to a bifurcated outlet. This design would provide flexibility to perform either mixing or capture experiments with the same mold design. Intersecting the main channel would be a fourth channel used for loading magnetic beads. This side channel provides a major advantage in that magnetic beads enter the channel in close proximity to the NiFe discs, increasing the chance that the magnetic bead is captured by the disc. Also, this keeps the upstream portion of the channel clean of beads or any other potential debris that might collect. This technique was applicable to both pressure driven flow (syringe pump) designs and to EOF designs.

The full microfluidic device is created by placing a fully cured and molded 10:1 polydimethylsiloxane (PDMS) microfluidic channel over a substrate with the microfabricated NiFe discs on it. The microfluidic channel is created via standard PDMS molding on an SU-8 mold on a silicon wafer (see Appendix). The PDMS channel is manually aligned to include the NiFe features. After placing the PDMS channel over the NiFe features, surfaces of the channel are passivated to prevent non-specific adsorption of beads or particles to the device. Following passivation, magnetic microbeads are pumped into the device and caught by the magnetized NiFe array. The concentration of the beads pumped into the device depended on the pumping method but ranged from 10^7 to 10^5 beads/mL. Pumping would continue until the array had been filled with magnetic beads. By keeping the external magnetic field spinning during the loading of the

magnetic microbeads, the beads are distributed across the entire array. Finally, the fluid to be used in the experiment was pumped into the array and observed via fluorescent microscopy on a Nikon Eclipse inverted microscope, a microscope where both light source and optics are below the microscope state and images are captured from reflected light. The inverted microscope was crucial for imaging as the over-hanging motor and magnet makes use of an upright microscope, where the optical light source is situated above the stage, impossible.

The exact details of device assembly, passivation depends on the pumping system of the device. Two primary device designs classified by their pumping method were used and described below (Step-by step instructions available for each design in Appendix B).

Device Assembly and Passivation

Pressure Driven Flow

Pressure driven flow is a common form of fluid pumping. This is typically performed using some sort of pressure head. This pressure head is the result of the inequality between the fluid pressures at inlets and outlets of a channel. In microfluidics, these pressure inequalities are typically created via syringe pumps that generate pressure by means of applying a steady force to a syringe, or by creating height differences between the fluid levels in two reservoirs.

Device Assembly

Early device designs utilized pressure driven flow generated by syringe pumps with a linear flow speed of 10 mm/s to 50mm/s. This is a common method used in microfluidic devices and is characterized by a parabolic flow profile. Usually holes are punched into the top of the PDMS to create access points for the tubing connections but that is not possible for this system. The combination of the overhanging magnet combined with performing the microfabrication on opaque silicon wafers required

flipping the combined structure so that the assembled device, with the PDMS on the stage and the silicon portion with the NiFe discs on top of the PDMS.

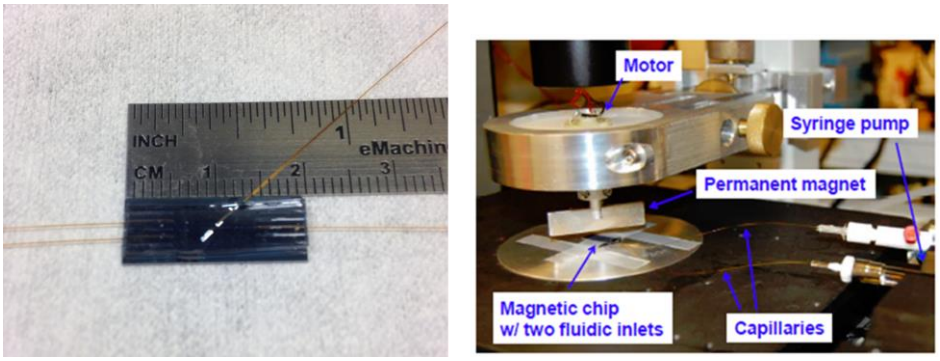

Figure 2.4 Left- image of fully assembled pressure driven flow device with tubing inserted. The tubing is held in place by smearing uncured PDMS at the channel edge before immediately curing it. Right-image of chip on stage with tubing and syringe pumps. PDMS is faced down on the stage.

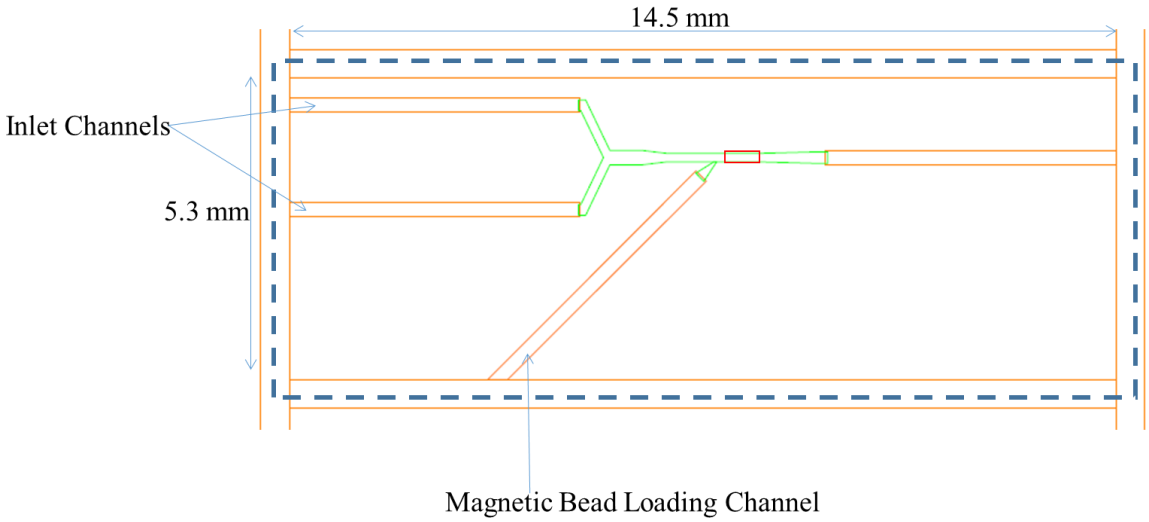

Figure 2.5 Schematic of PDMS microchannel placed over silicon to create fully microfluidic device. Small red rectangle demonstrates the not to scale region the soft magnetic features are located. The positioning of the PDMS channel over the features is performed under a dissecting microscope to insure proper alignment.

This orientation required an alternate method of inserting tubing connections. This was done by using a microfluidic channel (150µm wide by 6.5µm tall, green region

Figure 2.5) PDMS with connecting large channels (0.25mm wide by 0.25mm tall, orange regions) that were open to air. The large channels were exposed to air by cutting through portions of PDMS that had been molded onto 0.5mm wide by 0.25 mm tall regions SU-8 (cuts are marked by dashed line, Figure 2.5) after removing the fully cured PDMS sheet of multiple microfluidic channels from the mold. Tubing was placed into the large channel and sealed in place with PDMS. After the tubing has been inserted, a small volume of a 10:1 mixture of PDMS and crosslinking solution is placed near the entrance to the large channel. The uncured PDMS is pulled into the chamber via capillary forces. Placing the entire structure onto an 80ºC hot plate cures the PDMS and seals the device.

Passivation

The surfaces of the device were passivated using a co-block polymer, Pluronics F127.[41] This co-block polymer has a long carbon chain containing alternating hydrophilic and hydrophobic regions. The hydrophobic regions adsorb to the surface of the device while the hydrophilic regions fold up and are exposed to the bulk fluid. These hydrophilic regions create a barrier preventing non-specific adsorption of beads and particles to the surfaces. Passivation was achieved by incubating the tubing and channels with a 1% (w/v) solution of Pluronics F127 in phosphate buffered saline (PBS) for one hour at room temperature or overnight at 4 ^{0}C. To prevent clumping and adsorption between beads and particles, the magnetic beads and particles are placed in a solution of 0.1% (v/v) Tween-20 in PBS before pumping into the device.

Electro-Osmotic Flow

Electro osmotic flow (EOF) is flow generated via the application of an electric field across a capillary or microchannel.[42, 43] The effect is present in all channels but only generates significant pumping in small diameter channels. The effect is dependent on both the material of the microchannel and the solution in contact with the wall. The

flow rates generated scale with the voltage applied across the channel. The flow is generated by Columbic forces in the electrical double layer. A negatively-charged wall in this figure coincides with a thin, positively charged electrical double layer. The (typically nanoscale) thickness of the electrical double layer is exaggerated for the purposes of the figure. The difference between the local electrical potential and that of the bulk fluid is zero far from the wall but is finite near the wall. [41]

Device Assembly

An alternative device design utilizing electro-osmotic flow was also developed. The linear flow velocities generated via this method ranged from 10 µm/s to 100 µm/s. The exact velocity was dependent upon the voltage applied and the fluid level in the reservoirs. This system utilized NiFe discs fabricated on glass wafers (see Chapter 3) and thus could operate without flipping the assembled device. This removed the need for insertion of tubing in the side and could utilize reservoirs punched into the PDMS. To assemble the device, the PDMS microfluidic channel was removed from the mold and holes were punched into the PDMS with an 8 mm biopsy punch.

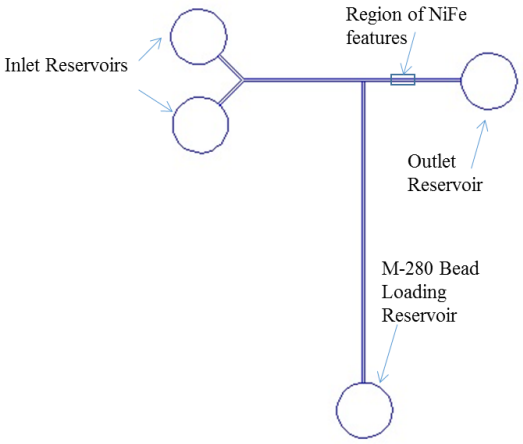

Figure 2.6 Schematic of PDMS microchannel with holes already punched used with electroosmotic flow. M-280 bead loading reservoir is 50 mm from the main channel to limit interaction with magnet.

Then the microfluidic channel is manually aligned onto a glass wafer with patterned NiFe discs placed in the channel. Adherence of the PDMS to a clean glass wafer is strong enough not to require plasma bonding of the PDMS. This is because the fluid pressures associated with EOF are very low because the reservoirs are open to the atmosphere, preventing any pressure build up.

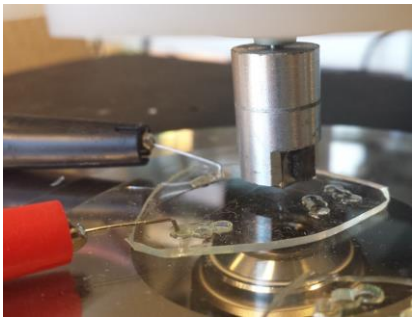

Figure 2.7 Image of assembled PDMS and glass wafer for device utilizing EOF for pumping. Voltage for EOF was generated using platinum electrodes to prevent corrosion.

Passivation

Utilizing the F127 and Tween-20 combination did not work in conjunction with the electro-osmotic flow. After initially applying a voltage, beads could be observed flowing as expected. After a short time however, the beads would begin to slow down and appear to hover stationary in an area. The particles could be observed moving slightly forward and back but never advancing in either direction. Also neighboring beads could even travel in opposite directions, indicating unusual flow conditions in the channel.

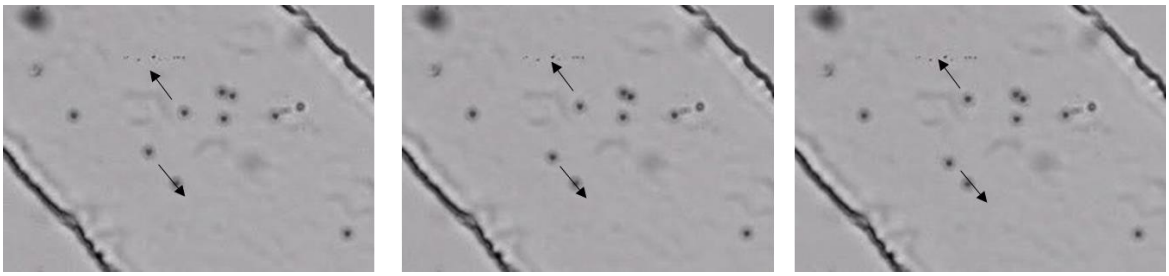

Figure 2.8 Particles begin to exhibit unusual flow characteristics in EOF pumped devices utilizing Pluronics F-127 for surface passivation. An example is shown here of neighboring particles moving in opposite directions.

Since the beads could not be pumped properly via EOF using the same solution as was used with pressure driven flow, this required a new method for passivating the surface to prevent non-specific adsorption. This would be even more important in the new system as now gravity would have the magnetic beads sitting on the bottom of the channel in contact with the glass below.

A literature review indicated that bovine serum albumen (BSA) does not change the charge of surface when adhered to a surface.[44] Since EOF utilizes interactions between surface charges and bulk fluids this indicated BSA would be compatible with EOF pumping. After experimentation, it was found using 0.1% (w/v) BSA in deionized water would prevent non-specific adsorption onto the channel surfaces as well as inhibit clumping of the magnetic beads. To fully passivate the channel, the 0.1% BSA solution would be loaded into the microfluidic channel, constructed of the assembled PDMS microchannel and glass substrate, and allowed to incubate at room temperature for 45 minutes. The glass wafer was treated with oxygen plasma prior to assembly, making the surface hydrophilic. The hydrophilicity of the surface would allow for easy wetting of the entire channel via capillary forces, without the need for pressurization.

CHAPTER 3

MICROFABRICATION

This section deals with the microfabrication of the soft magnetic features utilized in this device. Multiple methods and process flows to create different versions that all operate within the same basic principle. The size of the soft magnetic features made fabrication via standard microsystems fabrication techniques difficult. The unusual material composition of the soft magnetic features also led to many difficulties in microfabrication. This chapter addresses these issues and provides future users solutions. Detailed step-by-step procedures are available in Appendix A.

Metallization

The soft magnetic material chosen for use in this system is permalloy (NiFe), a common alloy of nickel and iron. The alloy of permalloy used here is 79% Ni 16.7% Fe and 4% Mo, from Kurt J. Lesker. Permalloy was chosen over Ni or Fe independently for its low residual magnetization and low coercivity. While the permeability of 99.95% pure Fe is comparable to permalloy, the residual magnetization is much lower in permalloy and while the residual magnetization of Ni is lower than permalloy, the permeability of permalloy is much greater than that of Ni[45]. Permalloy provides a strong alternative to either metal singly, as high permeability is required create stronger magnetic forces between the disc and the bead while low residual magnetization will allow for the external magnetic field to rotate freely through the NiFe disc at high frequencies.

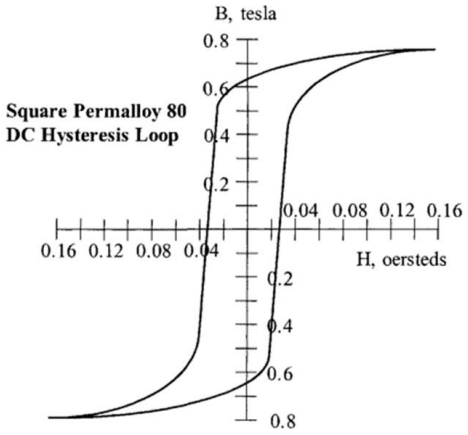

Figure 3.1 B-H Curve for permalloy. Of note are the low values as the curve crosses the H axis. This indicates there is little residual magnetization in the material. A large value would lead to excessing heating when the material is subjected to a dynamic magnetic field. It is because permalloy has such a low residual magnetization that it is often used in AC power transformers. Figure obtained from McLyman.[46]

The low hysteresis of NiFe will minimize the heat generated by the dynamic magnetization of the NiFe disc. This low hysteresis and energy loss from dynamic magnetization is the reason alloys of nickel and iron are often used in AC transformers.[46]

Liftoff Fabrication

The initial planned fabrication process for the device made use of electron beam evaporation combined with photolithography lift-off on <100> silicon wafers.

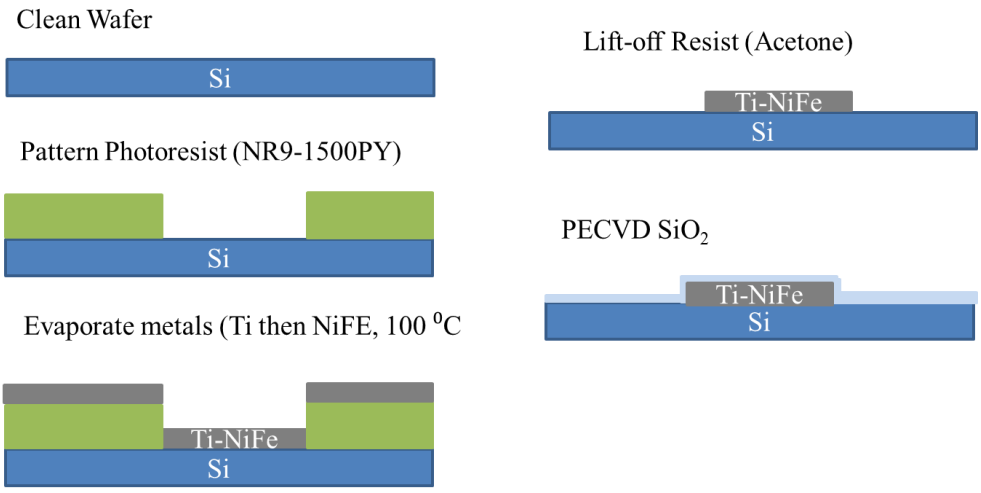

Figure 3.2 Initial metallization fabrication process flow. Not shown is a 10nm layer of Ti to act as an adhesion layer evaporated onto the wafer without breaking vacuum before the NiFe layer. The metal thickness was 350 nm and the SiO_2 thickness was 180 nm.

The wafers were first cleaned in a piranha solution (4:1 H2SO4 to H2O2) for five minutes prior to processing. This first design used very small NiFe features, 3 micron diameter circles. A negative photoresist, NR9-1500PY was chosen for its excellent sidewall profile for lift off and patterned onto silicon wafers via standard photolithography. A thin adhesion layer of 10nm of Ti was deposited prior to evaporating 350nm of NiFe.

Early attempts at e-beam evaporation using the CVC E-beam Evaporator proved unsuccessful. The evaporated NiFe film would peel off of the adhesion layer. This result was seen on both bare silicon wafers as well as patterned photoresist. The peeling was observed over a wide range of deposition rates (1-10 angstroms/s) and chamber pressures ($8*10^{-7}$ to $3*10^{-5}$ mTorr). Evaporation was even attempted via a stepwise method: depositing 50 nm at a time with 20 minutes pauses between steps.

Figure 3.3 NiFe film peeling after deposition. After e-beam evaporation the NiFe film would peel away from the Ti adhesion layer beneath it. This result was seen with various evaporation chamber conditions and substrates.

It is a fact that evaporated Ni deposits with a strong tensile stress that makes the film unstable.[47] To overcome this, energy should be added to the system via either heating the substrate or ion bombardment. It would have been possible to overcome some these issues by utilizing sputtering but the sputtering technique is not compatible with lift-off for creation of very small features.

To reduce the evaporated film stress, the e-beam evaporation was performed in a Denton Infinity E-beam Evaporator which contains an infrared (IR) heater. The Infinity utilizes a beam of electrons fired at the metal source to heat it to a temperature hot enough for the metal to evaporate and deposit as a thin film onto a surface. The IR heater is an optional feature that if activated will heat the chamber to a set temperature prior to

activating the electron beam for evaporation. The heater uses feedback from a thermocouple inside the chamber to automatically modulate the intensity and on-time of the heater. Heating the chamber to 95 °C prior to deposition and maintaining this temperature was able to keep the NiFe film attached to the Ti adhesion layer and the underlying photoresist.

Figure 3.4 NiFe film remains intact e-beam evaporation performed with the chamber heated.

This temperature is also below the glass transition temperature of NR9-1500PY, 110 °C, making this technique compatible with a lift-off technique. Scanning electron microscopy (SEM) of the produced features combined with energy-dispersive X-ray spectroscopy (EDS) using the Hitachi 3700 VP-SEM was performed on the created features, showing strong uniformity and correct material composition of metallic features.

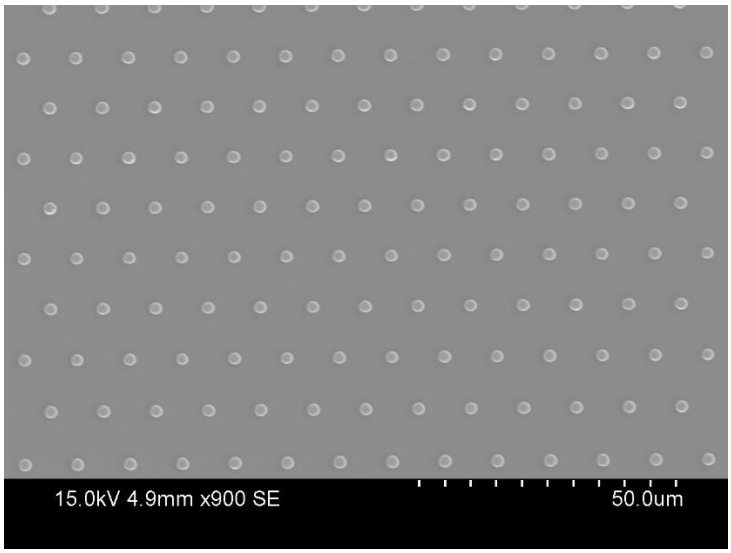

Figure 3.5 Scanning electron microscopy images of NiFe features created via lift-off. These features show strong uniformity in both size and shape.

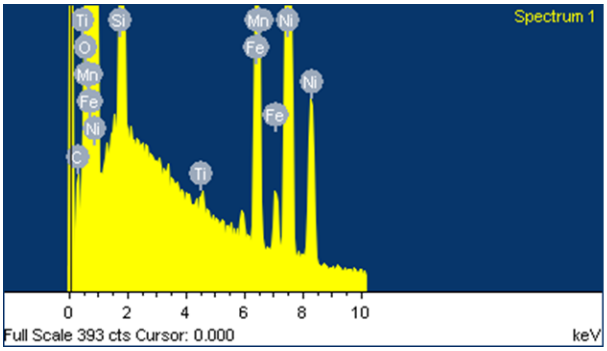

Element	Weight%	Atomic%	
C K	2.25	8.41	
O K	2.70	7.60	
Si K	12.70	20.33	
Ti K	0.31	0.30	
Mn K	0.55	0.45	
Fe K	12.72	10.24	
Ni K	68.78	52.68	
Totals	100.00		

Figure 3.6 Elemental analysis performed via EDS of NiFe features created via lift-off. The key feature is the ratio of Ni to Fe remains 5:1.

The final step in creating the features is the deposition of a 180 nm of SiO_2 over the NiFe discs. This is important for protecting the NiFe discs from oxidation upon exposure to fluids as well as helping to anchor the NiFe in place. This SiO_2 layer also provides a uniform surface for easy surface passivation to prevent non-specific adsorption in the system, which is important in bio-sampling experiments. Finally, the presence of the SiO2 layer helps to hold the NiFe features down to the substrate during cleaning between experiments, making the chips re-usable. The presence of the NiFe features already on the wafer required the deposition of the SiO_2 layer via plasma

enhanced chemical vapor deposition (PECVD). Depositing via PECVD required much lower temperature than typical CVD processes. The higher temperatures of typical CVD processes would have damaged the NiFe discs already on the wafer. The PECVD was performed at 250 °C on the Oxford PECVD and then annealed in the Lindbergh Furnace Polymer curing tube (see Appendix A for details).

Elevated NiFe Disc

An alternative fabrication methodology was developed to take try and take greater advantage of the magnetic field strength of the NiFe discs. The magnetic beads used in this device are 2.8 microns in diameter. However utilizing larger beads could potentially have greater effectiveness for mixing, by perturbing more of the fluid, and capture, by increasing the binding area. Bringing the NiFe feature off of the floor of the channel and putting it in the center plane of the magnetic beads would increase the magnetic attraction between magnetic bead and the NiFe disc, by placing the region highest magnetic field gradient closer to the center of mass of the magnetic bead.

This alternative fabrication method utilized a self-aligned process combined with wet and dry etching to create a pillar upon which the NiFe disc is placed. Figure 3.7 contains the process flow used to create such a system.

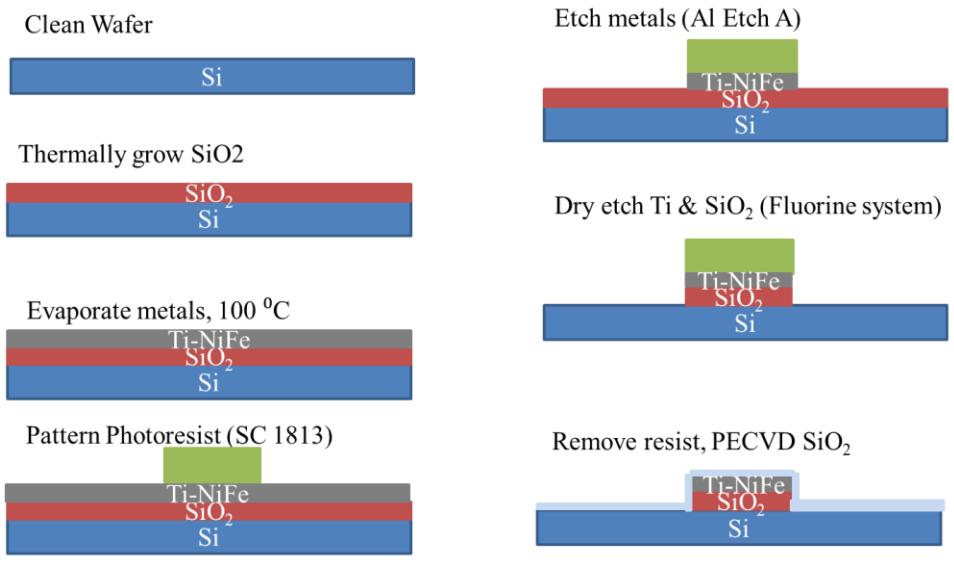

Figure 3.7 Process flow for creation of elevated NiFe features. This places the magnetic feature in the same plane as the center of the magnetic bead.

This method begins by growing silicon dioxide onto a silicon wafer then depositing the 10 nm Ti adhesion layer and the 350 nm NiFe film at 95 °C before creating a photoresist etch mask. By using a positive photoresist for the etch mask, the same photolithography mask used for the lift-off fabrication can be used in this process. Also because of the high reflectivity of the NiFe film there is little need to modify the photolithography steps from normal silicon wafer processing when using the positive resist. Aluminum Etch A was used to etch the NiFe film at room temperature (etch time ~120 minutes, no agitation). Aluminum Etch A etches NiFe at a controllable rate and is compatible with most positive resists. After etching the metal, the grown SiO2 can then be dry etched via reactive ion etching to create high aspect ratio pillars of SiO2 with the metal feature on top. This method was used to create a 2 µm NiFe disc elevated 2.3 µm into the channel on top of a 3 µm diameter wide cylinder of SiO_2.

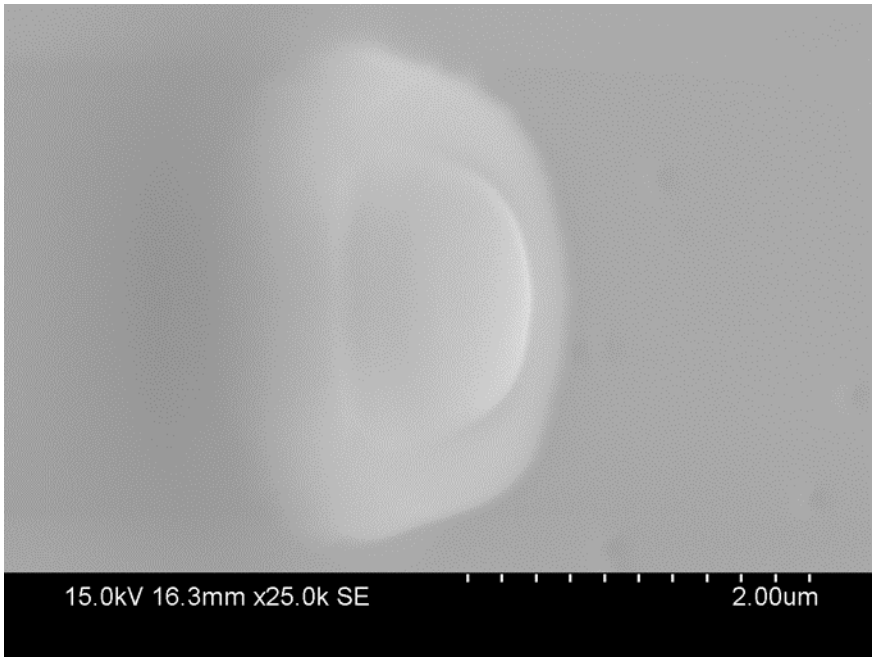

Figure 3.8 SEM image of elevated NiFe disc on top of SiO_2 pillar. The metal is a smaller diameter than the pillar because of under-etching during the wet etching step and appears as a small bump in the image.

Metallization on Glass Substrate

A version of this system was designed and fabricated for use with electro-osmotic flow (EOF). A major change from switching from a pressure driven system to an EOF system is the requirement of fabricating the NiFe discs on a glass substrate. This was required for viewing of the channel under a microscope while still maintaining a magnet over the top of the channel. To accomplish this, a fabrication process was developed on soda lime glass wafers. The soda lime glass wafers used in this work are 100mm in diameter, 700 μm thick, double-sided polish wafers from University Wafer. Performing photolithography with the negative resists proved difficult on a glass substrate so lift-off was discounted as a potential method. It was difficult to find the correct combination of baking times, temperatures, exposure and development to create the correctly sized features. Instead the wet etching method from the elevated NiFe disc method was utilized because it used a positive resist on an already reflective surface.

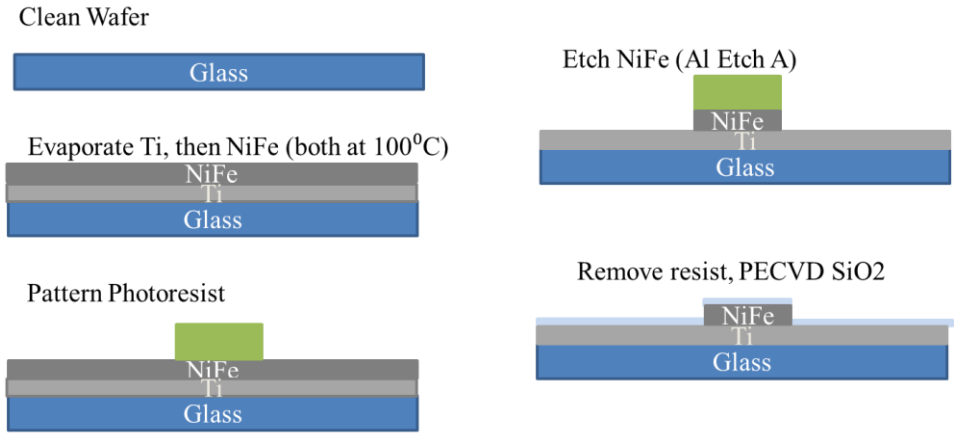

Figure 3.9 Microfabrication process flow for placing NiFe features onto a glass substrate.

The lithography of this system needed to be modified. Utilizing hard contact photolithography produced toroid shaped features instead of the required circular features.

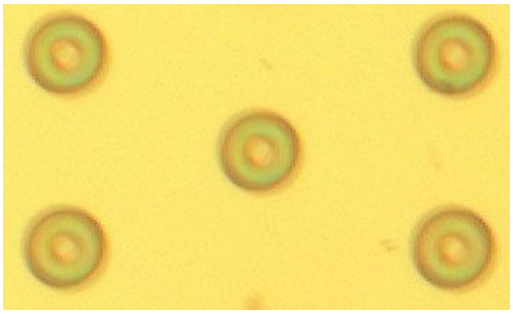

Figure 3.10 Toroid features created instead of solid circles. The toroid features were slightly oversized with a lack of material in the middle. The use of positive photoresist indicated these features were created from constructive interference from poor contact between wafer and mask.

It was discovered that the surface of the glass wafer was not maintaining good contact with the mask, creating constructive interference patterns during the exposure of the photoresist on the wafer. Using low vacuum contact solved this problem and produced the proper photoresist patterns.

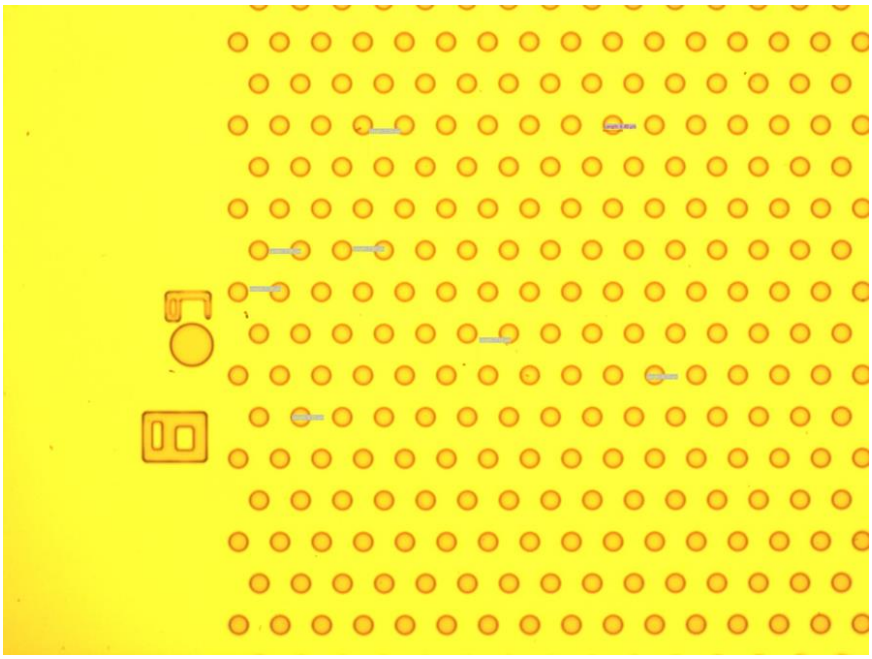

Figure 3.11 Properly sized solid circles created using low-vacuum contact with standard photolithography.

After assembly of the full device, in some preliminary experiments bubbles would form at random locations on the glass wafer when voltage was applied. The voltage applied ranged from 10 V to 250 V and always had an amperage reading of less than 0.01 mA. This low power generation in the system indicates these bubbles were not due to fluid heating. These bubbles would form in regions beneath the PDMS, between the PDMS and the glass substrate beneath and in reservoirs. The fact that the bubbles would form in regions with no fluid contact, i.e. beneath the PDMS further indicates that the bubbles did not result from heating of the fluid. The bubbles beneath the PDMS would grow while the voltage was applied and shrink when the voltage was turned off. Bubbles from the reservoirs would form and float to the top of the reservoirs while the voltage was applied.

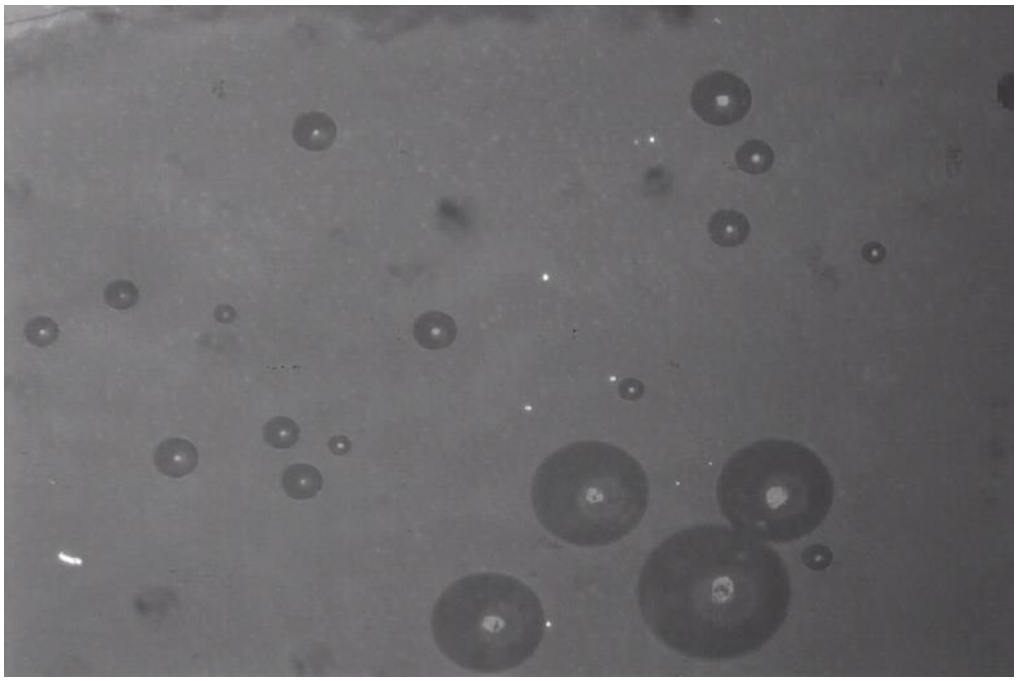

Figure 3.12 Bubbles form beneath PDMS while voltage is applied to device. The presence of the bubbles correlated with the inability of particles to pump in the device. The growing of the bubbles correlated perfectly with the presence of the applied voltage.

If these bubbles would form then no beads would pump through the device. Beads would remain suspended in the reservoir. These bubbles would never be found when attempting EOF pumping on a blank glass slide. The hypothesized problem was the combination of the PECVD deposited SiO_2 and the Ti adhesion layer that was not removed. The inconsistent formation of the bubbles was because of the random pinhole formation in the PECVD layer. The Ti adhesion layer acts as a short circuit for the applied voltage. This prevents the Debye layer from forming in the PDMS channel and without the layer no EOF pumping would occur.

To overcome this problem, a new fabrication process was developed. By heating the chamber to 250 °C, it was possible to deposit a 350 nm layer of NiFe onto a glass wafer with no adhesion layer. The film remains intact even throughout photolithography processing.

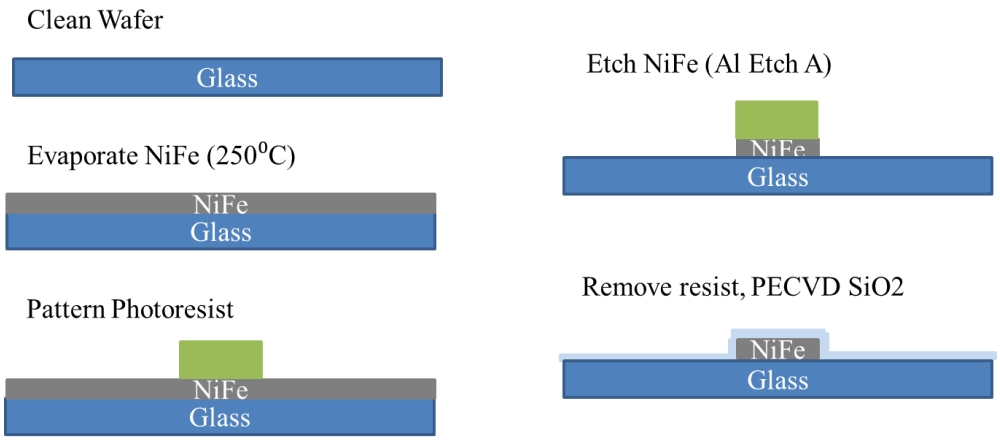

Figure 3.13 Process flow for fabrication of NiFe features on glass substrate without adhesion layer. The etch time did increase by a factor of 1.5 after evaporation at this higher temperature.

The time to etch through the NiFe the film deposited at this higher temperature does increase by a factor of 1.5. This is further proof of the improved film quality.

To prove the conformal coating of the SiO2 over the entire NiFe disc, a fully processed wafer was placed into a piranha etch solution (4 parts sulfuric acid to 1 part hydrogen peroxide) for 10 seconds. After removal, images showed the vast majority of NiFe features remained intact, indicating the SiO2 film protected the NiFe disc.

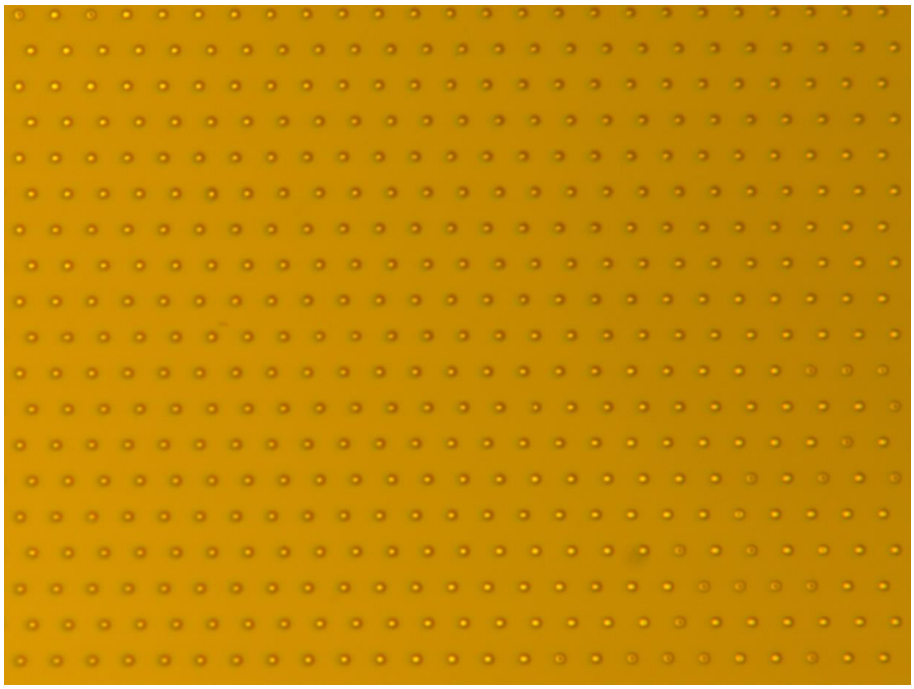

Figure 3.14 Following PECVD SiO_2 deposition, the NiFe features were protected from a piranha etch solution for 10s, indicating the SiO_2 coating is properly protecting the features.

CHAPTER 4

INDIRECT MAGNETIC FORCE MEASUREMENTS

Early experiments focused on the operating parameters of the rotating magnetic beads around the NiFe discs. The goal of this work was to obtain empirical data regarding the operating limits of the device. Of major concern was the magnetic force between the NiFe feature and the magnetic bead.

Correlation between Magnetic Bead and Magnetic Field Lines

Early modeling work from a collaborator, Dr. Wenbin Mao, showed potential problems for the magnetic bead to stay in sync with the magnetic field lines. These data suggested that the bead would not be able to maintain the same frequency of the magnetic field if the frequency became too high or if the magnetic field strength became too low.

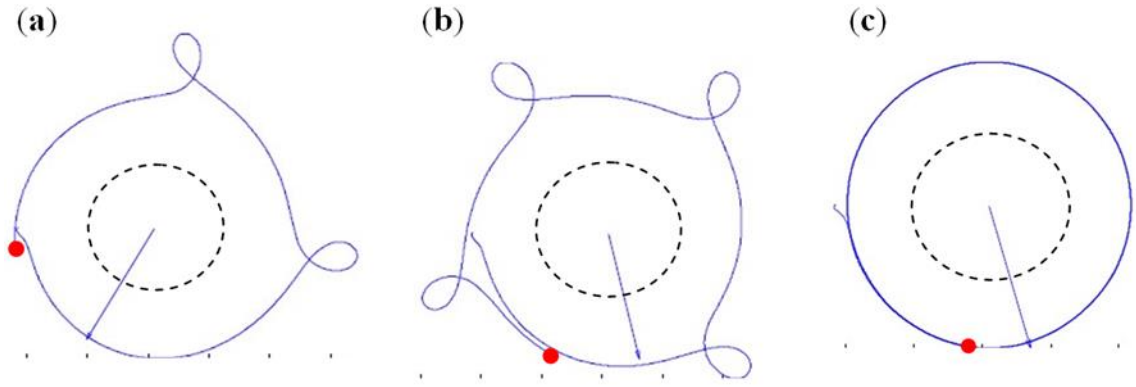

Figure 4.1 Trajectories of magnetic beads moving around static disks in a rotating magnetic field. (a) A bead completes one period around the disk during about three periods of the magnetic field (f = 8000 RPM, B = 0.063 T). (b) A bead completes one period around the disk during about four periods of the magnetic field (f = 10,000 RPM, B = 0.074 T). (c) A bead rotates with the frequency equal to that of the external magnetic field and follows nearly circular trajectory around the disk (f = 8000 RPM, B = 0.13 T). The dotted line shows the outer contour of the static disk. The dot indicates the final position of the bead, whereas the arrow shows the direction of magnetic field. Figure from Owen, et al.[48]

To ascertain the validity of this hypothesis, a series of experiments were conducted to image the magnetic bead under high speed rotation. This was accomplished by use of two linked high speed Phantom cameras (cameras used: v210 and v9.0, Vision Research, Wayne, NJ). One camera was used to image the spinning magnet and the second camera imaged the beads rotating in the device, capturing images at 2,000 frames/second. The v9.0 camera was slaved to the v210 and the time stamps between the two cameras were no more than 10 microseconds apart. By imaging the position of the magnet, the position of the magnetic field lines could be super-imposed upon the channel. Comparison of the two synced images showed how the beads were staying in sync with the rotating magnetic field.

Experiments were conducted at four magnetic field rotational frequencies, which were controlled via the motor RPM, and at two different magnetic field strengths, which was controlled by positioning the magnet further away from the chip and measuring the magnetic field strength via a DC magnetometer (AlphaLab Inc., Model 1). The magnetic field frequencies were 2,500 rpm, 5,000 rpm, 7,500 rpm and 10,000 rpm and the magnetic field strengths were measured as 0.18 T and 0.088T. The high speed camera showed the magnetic beads rotating at the same frequency as the magnetic field at both field strengths. However, a lag was observed between the position of the magnetic field lines and the position of the magnetic beads.

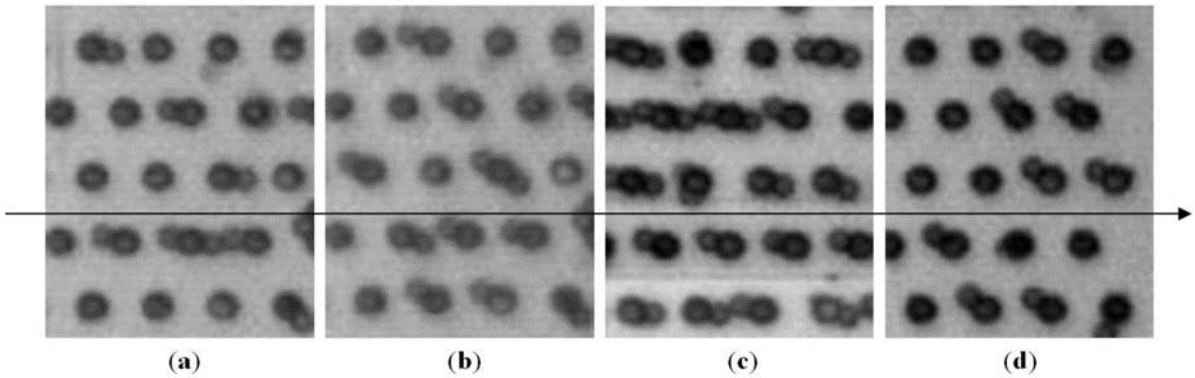

Figure 4.2 Images of microbeads circling around static discs in rotating magnetic field. The alignment of the magnetic field lines is represented by the arrow through the images. The magnetic field rotational speed and magnetic field strength felt at the chip is given beneath the images. These were the two experimental parameters varied for the experiments. (a) Speed: 2500 rpm, Mag. Field: 0188 T; (b) Speed: 10,000 rpm, Mag. Field: 0.18 T; (c) Speed: 2500 rpm, Mag. Field: 0.088 T; (d) Speed: 10,000 rpm, Mag. Field: 0.088T. Figure from Owen, et al.[48]

The magnetic beads appeared slightly out of phase with the magnetic field lines. This lag was manually measured across each experimental condition and averaged before plotting in Figure 4.3. For each data point, a minimum of 60 measurements were take (at least six frames with 10 measurements per frame).

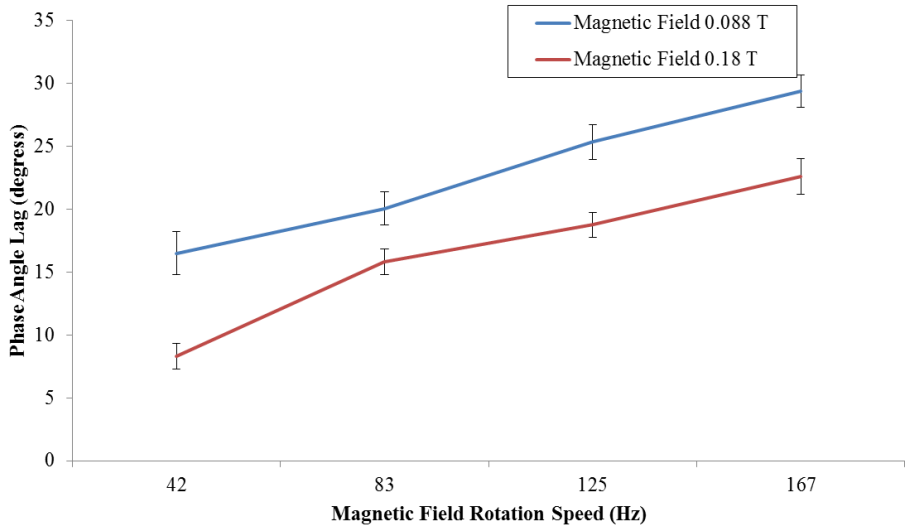

Figure 4.3 Phase angle lags for four different magnetic field rotational speed and two different magnetic field strengths. Each experimental data point represents 60 measurements across 6 time points. Error bars represent one standard deviation.

The plots exhibited a linear profile which is expected. The low Re number of the flow around the bead would place the magnetic bead in the regime of Stokes flow and as such Stokes Law

$$F_d = 6\pi\mu RV$$

where F_d is the drag force on the bead, μ is the dynamic viscosity, R is the radius of the bead and V is the flow velocity relative to the bead, determines the force on the bead. In this low Re number regime, Stokes Law says that the drag force on the particle is linearly related to velocity. In these experiments, the lag of the magnetic bead increased linearly with increasing bead velocity. In these experiments, the velocity is calculated using the frequency of the bead rotations, defined by motor rpm, and the path of the bead. The path was as a circle of radius 3 μm. This radius was the summation of radius of the NiFe feature and the radius of the magnetic bead. As the relative velocity increases, via increasing frequency over a constant path, the fluid drag force increased and pushed the bead further behind the magnetic field lines. It was interesting to note that the line created by the data points had a non-zero y-axis intercept. It is possible this is due to the very low but still non-zero coercivity of the magnetic material (see Chapter 3).

Static Force between Magnetic Bead and NiFe Feature

To further test the operating conditions of the device, the magnetic force between the magnetic bead and the NiFe disc was measured directly in the device. This was done by loading the magnetic beads into the NiFe array and then applying steadily increasing volumetric flowrates via a syringe pump. The magnetic field remained stationary during each experiment however the height of the magnet from the chip was altered between sets of experiments. Videos were recorded of these experiments and the number of beads pushed off from their position was measured. The flow would start at 0.2 μL/min, corresponding to approximately a 5 mm/s linear velocity, and increase in subsequent

videos. The flow rate required to remove 20% of the total population of magnetic beads in the image from their position by the end of 30s was chosen at the crucial cutoff.

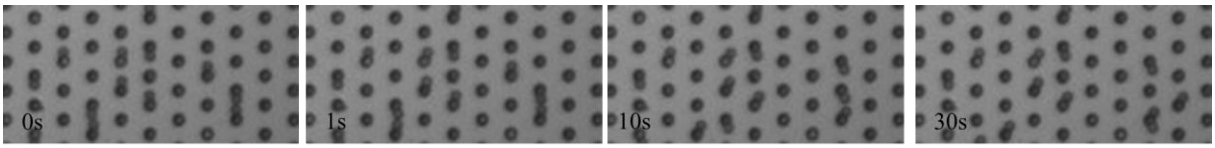

Figure 4.4 Still images taken from a video showing the change in bead position over time. Over the thirty seconds, magnetic beads can be viewed to significantly change angle. Some beads even jump to a new magnetic feature.

Since the magnetic bead was held stationary in these experiments, the velocity was calculated from the volumetric flow rate applied and the channel cross-sectional area (150 µm wide by 6.7 µm tall). The velocity was used with Stokes Law to estimate the force required to knock-off a magnetic particle from the NiFe disc. The value of the knock-off force for different magnetic field strengths is plotted in Figure 4.5. These data show that approximate 1nN of force is required to remove the magnetic bead from the 3 µm diameter NiFe disc used in these experiments.

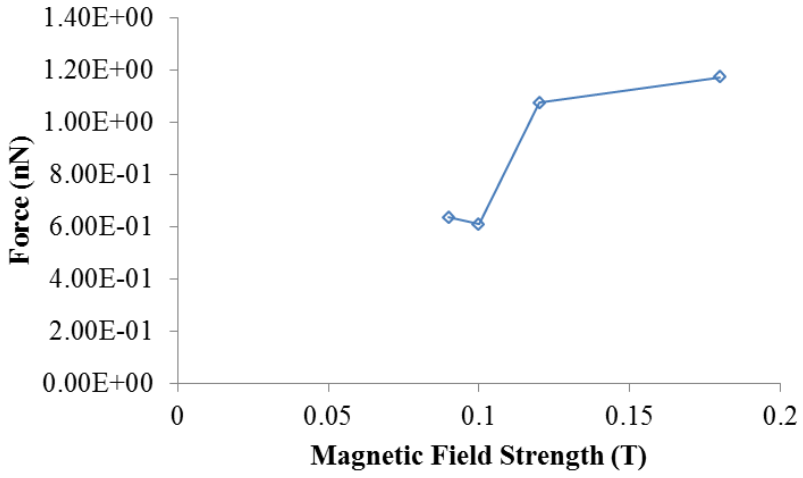

Figure 4.5 The force required to displace a significant number of magnetic beads (>20% of the total population) in 30 seconds was calculated using Stokes Law and that value was plotted for various magnetic field strengths.

This is important information for scaling up this system to handle larger flow velocities and potentially greater volumetric flow rates. These experiments show it would be not feasible to design a fluid system that applies more than 1 nN of force to the magnetic beads as this would make the magnetic beads unstable. To increase device throughput, higher volumetric flow rates would have to be achieved with larger channel cross-sections to reduce fluid linear velocity.

CHAPTER 5

MICROFLUIDIC MIXING VIA ROTATING MAGNETIC BEADS

A major aim of this work was to characterize the capacity for this rotating array of magnetic microbeads to mix fluids inside a microfluidic channel. An ideal mixing device would achieve significant mixing in a short channel length with high volumetric flow rates. In the system described, if the bulk flow is too large, there will be little effect from the rotating magnetic beads. A fluid particle in the high bulk flow rate would have little time to interact with the magnetic beads. The mixing achieved by this system will depend on the degree of interaction between the rotating magnetic beads and the bulk fluid. Two important velocities come into play when describing the interaction between the magnetic beads and the fluid in the channel. The first is the linear flow velocity derived from the volumetric flow rate of the bulk fluid. The second velocity of note is the linear velocity of the magnetic microbead as it rotates around the NiFe feature. The velocity of the magnetic microbead can be calculated from the path of the magnetic microbead and the frequency of the rotation of the external magnetic field. The path of the microbead is calculated from the center of the bead, resulting in a circle with a radius equal to the sum of the radius of the NiFe feature and the radius of the magnetic bead. Thus a dimensionless parameter

$$u = \frac{U_x}{V_b}$$

where U_x is the linear velocity of the bulk fluid pumping down the channel and V_b is the linear velocity of the magnetic microbead, can be used to describe the flow inside the array of NiFe features with rotating magnetic microbeads. The goal of this work is to investigate the value of *u* on mixing.

Bead Modification

Dynabeads M-280 from Life Technologies were the magnetic beads used for these experiments. The M-280 beads exhibit superparamagnetic properties and are pre-functionalized with streptavidin. To reduce the interaction between the M-280 functionalized protein and the nanoparticles used in these experiments, the M-280 beads were placed in a 0.6 mL polystyrene conical tube and incubated in boiling water for 30 minutes.

Mixing Metric

Mixing was measured in these experiments by utilizing variance of fluorescent intensity as an analog for concentration. This is done by pumping two streams of fluid, side by side through the channel. One stream contains a fluorescent marker while the other fluid contains nothing. In a perfectly unmixed channel, the two streams will yield a high variance, the exact number depending on the scaling of fluorescent intensity. A perfectly mixed fluid will have a variance of zero, with the fluorescent intensity perfectly distributed across the entire channel. This technique is well established in the literature.[49-53] This technique provides a method for quantification of a qualitative effect observed by eye.

The fluorescent stream chosen for these experiments was a dilution of 40nm fluorescent particles (Fluorspheres, 40nm, Yellow-Green, from Life Technologies). The size of these particles would lead to a lower diffusion rate when compared to small molecule fluorescent proteins or fluorescent dyes. This would help to keep the interface between the two fluid streams as sharp as possible.

It is important to note that the mixing results shown here via experiment and numerical simulation are contingent upon the Peclet number

$$Pe = \frac{Lu}{D}$$

where *L*is the characteristic length, *u* is the local flow velocity and *D* is the coefficient of diffusion for the particle. The coefficient of diffusion for a spherical particle can be estimated via

$$D = \frac{kT}{6\pi\mu r}$$

where *k* is Boltzmann's constant, *T* is absolute temperature, μ is the dynamic viscosity of the fluid and *r* is the radius of the particle. Any changes in the Peclet number of the system will yield differing mixing results.

Pressure Driven Mixing

The initial work investigating the capacity of the rotating magnetic microbeads to mix a fluid in a microfluidic channel utilized the pressure driven system. This experiment utilized unmodified M-280 magnetic microbeads. The fluorescent dye used was a 1:10 dilution of 40nm, yellow-green, carboxylate modified Fluorspheres (from Life Technologies). The carboxylate coating of these fluorescent particles did not interact with the streptavidin coating on the M-280 magnetic beads, making them a suitable option to study the pure mixing effectiveness of this system.

In these early experiments it was difficult to collect data. One of several problems would often occur in the process of attempting to collect data. The bead loading could prove difficult due to the sudden constriction in height from the tubing inlet area to the main channel height. The tubing inlet area had a channel height of 250 μm to accommodate the silica tubing through which the magnetic beads were pumped from the syringe. This sudden decrease in height (250 μm channel height to 6.7 μm channel height) created a low pressure region where magnetic beads would accumulate. The magnetic beads would continue to accumulate until the entire inlet area would become plugged with magnetic beads. If the NiFe array was not filled prior to that then a new chip would have to be assembled and a new experiment tried. Another problem with

operating this system was the danger of bubbles entering the system. If an air bubble entered the array area, all rotating magnetic beads would be pushed to the walls by the bubble. After the bubble had passed through some of the beads would redistribute across the array of NiFe discs but the distribution would not be as uniform as prior to the bubble. Some of these problems with bubbles could be overcome by utilizing a syringe pump at the outlet to pull fluid through the system. However this could lead to problems of more magnetic beads being pulled into the system after the experiment was already in progress.

The data collected from these experiments showed very little mixing occurring in the device. Figure 1 shows images of magnetic beads rotating at 2,500 rpm while two streams of fluid, one with fluorescent particles and the other with just DI water.

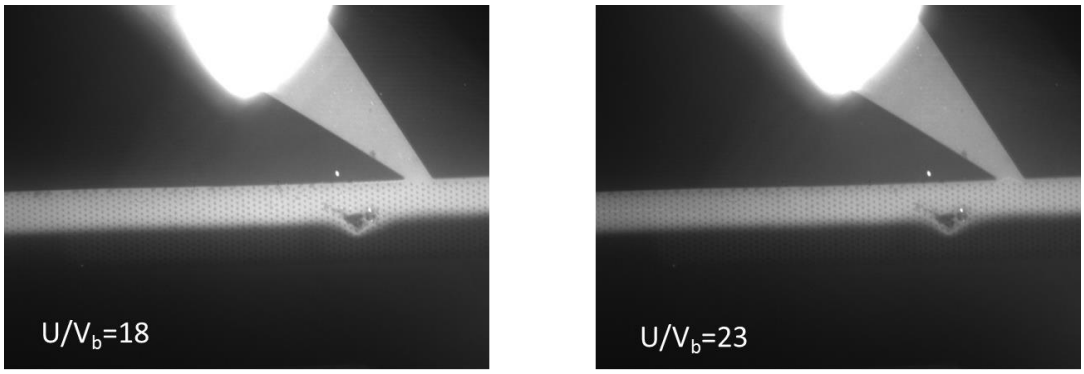

Figure 5.1 Two-stream fluid pumped over array of rotating magnetic beads. No visible mixing was observed under lowest flow conditions created by syringe pumps. Beads were rotating at 2500 rpm, fluid pumping at a linear flow velocity of 13 mm/s and 16 mm/s respectively.

The total volumetric flow rate for the two different experiments was 0.8 µL/min and 1.0 µL/min. A single syringe pump was used to pump fluid from two separate syringes, one contained DI water and one contained the fluorescent nanoparticles. The syringe pump was set to dispense 0.4 µL/min and 0.5 µL/min. This is the minimum possible flow rate that experimentally determined would still result in an interface that was not undulating and produced a sharp contrast in brightness. These data shows that

there was no observable mixing occurring in the array. The calculated ratios for these experiments, u = 18 and u =23 respectively, show that even at these achievably low flow rates, the bulk fluid velocity would still dominate the flow inside the channel and no mixing is achieved.

Electro-Osmotic Flow System

The alternate pumping system of electro-osmotic flow was used to pump for the mixing experiments. Electro-osmotic flow produces lower flow rates which would make it easier to fully investigate the range of u values for this system. Two streams were pumped via electroosmotic flow. A 90V potential were applied, so as to produce linear flow rates of 10-30 μm/s, measured from captured images. Because the flow rates are so small, gravity and surface tension can play a significant role in the linear flow velocity. This makes it difficult to predict the linear flow velocity, U, inside the channel prior to an experiment. When using EOF as the pumping system, the linear flow velocity must be determined after the experiment by examining streaklines from the fluid captured in images. The streaklines are generated by the >200ms exposure times required to capture the fluorescent images. The length of two streaklines per image are measured and used with the exposure time to calculate the average linear flow velocity in the channel. The V_b is still calculated from using the frequency of the magnetic field rotation and the path of the bead which is a circle or ellipse whose radius is the sum of the NiFe feature radius and the magnetic bead radius. One stream contained DI water with 0.1% BSA and the other contained the same but with a 0.1% concentration of fluorescent nanoparticles (Fluorspheres Yellow-Green, 40nm, from Life Technologies). It was found that the carboxylate modified Fluorspheres would not pump normally under EOF. The carboxylate-modified particles would initially pump correctly but after 30s, the nanoparticles would begin traveling towards the positive terminal while the bulk fluid traveled towards the negative terminal. This behavior was likely due to the attraction of

the particle's surface charge being greater than the inertial force of the bulk fluid. Thus, biotin coated nanoparticles of the same brand were desiccated and then re-suspended before further boiling the beads for 1 hour, to fully remove the biotin coating and eliminating any interaction with the M-280 magnetic beads. The speed of the orbit of the magnetic beads is controlled by the speed of the suspended DC motor and the effect on mixing of the two streams was recorded via Photometrics CCD camera (Cool Snap HQ).

Mixing under flow was investigated for three different array geometries. Each array geometry contained a different shape of NiFe feature. The shapes used were a 6 µm diameter circular disc, a 3 µm by 6 µm ellipse (vertical ellipse) and a 6 µm by 3 µm ellipse (horizontal ellipse).

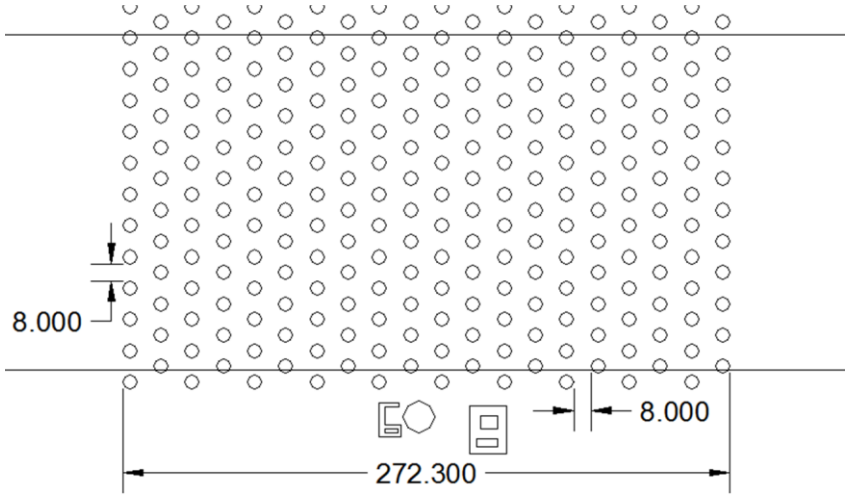

a)

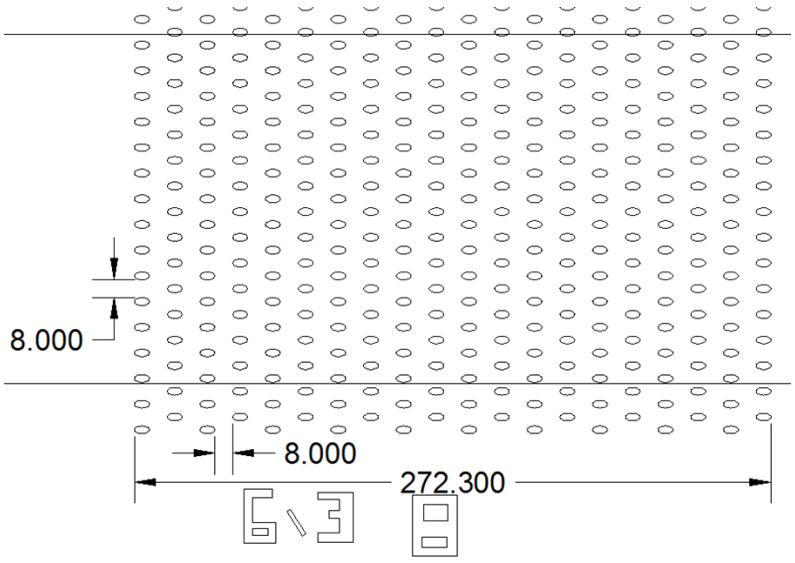

b)

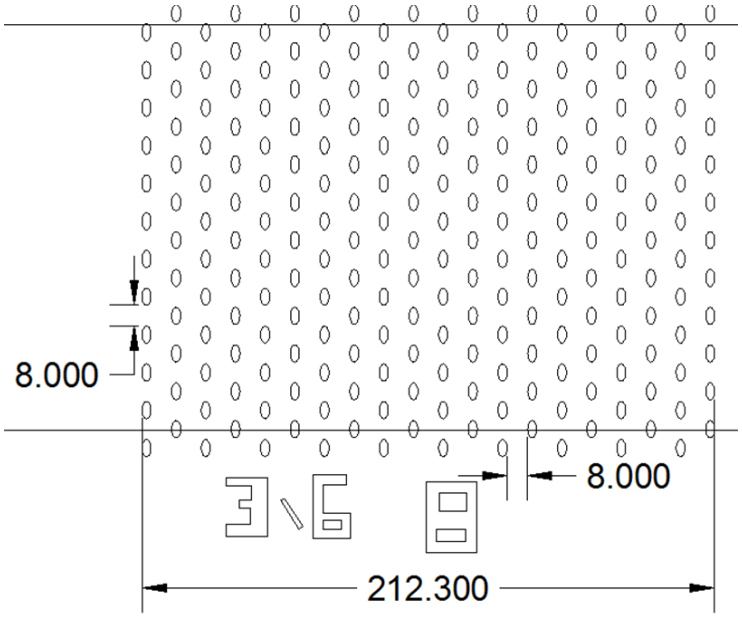

c)

Figure 5.2 Geometry of a) circular feature, b) horizontal ellipse and c) vertical ellipse arrays used in experiments. The two black lines represent the channel with width of 150 µm. The total number of features created were much wider than could fit into a channel to provide maximum flexibility in alignment of the PDMS microchannel.

The key distinction between the two ellipses geometries was whether the ellipse major axis was parallel or perpendicular to the flow. In each geometry, the number of

columns of features that the fluid would travel over was 20 and the edge to edge between rows and features within rows is 8 µm.

Stationary Fluid

Two streams were pumped over a 6 µm circular feature array with the magnetic microbeads stationary. The edge to edge spacing between rows and columns of the circles is 8 µm. The pumping was stopped, leading to rapid deceleration of the fluid. After the deceleration, the magnetic microbeads were started rotating at 4000 rpm as a video recorded the results. Still images from the video are shown in Figure 5.3. The magnetic beads are spinning clockwise in the image. The video was recorded with an inverted microscope and thus the NiFe features appear as black circles surrounded by fluorescence.

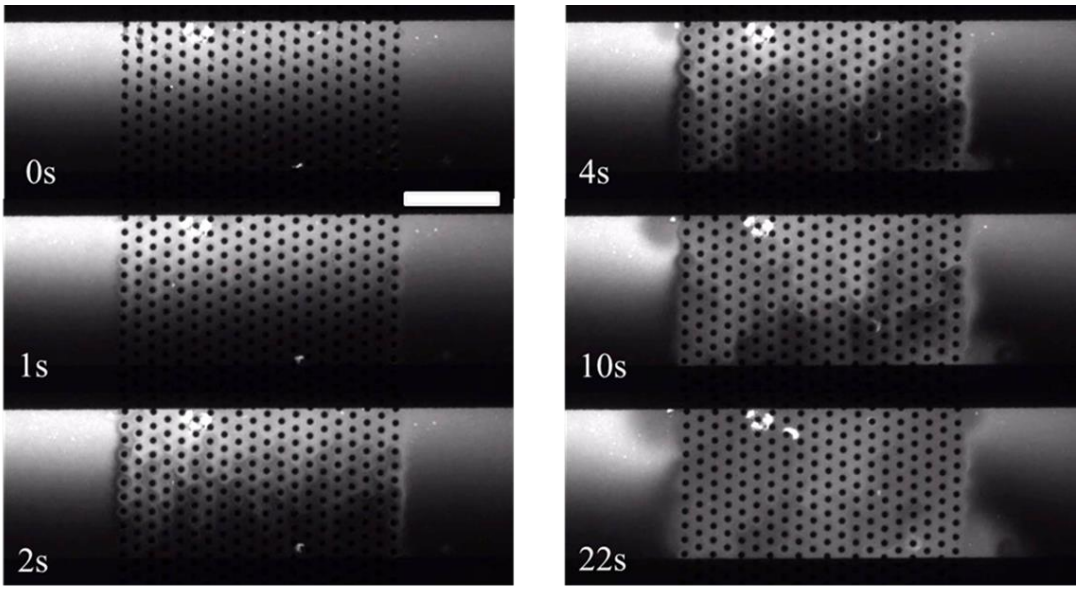

Figure 5.3 Images of bead rotation (4000rpm) creating mixing effects in stopped fluid. Fluorescence travels long column of features across the channel. Notice the collection of fluorescence in the lower right corner and the lack of fluorescence in the top left. These regions are due to a weak pumping effect from the beads at the outer edges of the array. (Scale bar 100µm)

At 0s it is possible to view some of the stationary magnetic microbeads but it later images they appear to disappear. This is due to the frame rate of the camera and the high speed (4000rpm) that the magnetic beads are rotating around the NiFe feature.

The first noticeable effects in the images of Figure 5.3 are coronae surrounding the NiFe features. These coronae form because of streamlines formed by the rotating microbeads. Periodic coronae of fluorescence form around the NiFe features and travels down the image, transporting the fluorescence across the channel. The transported fluorescence travels down a single column of NiFe features with little discernible transport to the left or right in the image. As the microbead rotates, it drags fluid with it including the fluorescent nanoparticles. This bead will then pass a neighbor bead traveling in the opposite direction and some fluid and fluorescence will be pulled to the neighbor bead. In some regions the fluorescence is transported across the channel in less than 2 seconds while in some regions it fills in more slowly. By the end of the video the coronae have disappeared, replaced with a uniform diffuse fluorescence across the entire array.

The fastest regions of transport appear to be at the outer edges of the array. Here the rapid transport effect is because the beads orbiting on the left edge of the mixing array are always moving upward when they are on the portion of their trajectories that is external to the array. This appears to result in the magnetic microbeads pulling the fluid external to the array across the channel (upward in Figure 5.3). The beads on the right edge of the array pull fluid across the channel in the opposite direction (downward in Figure 5.3) due to the same mechanism. Over time, this accounts for the accumulation of fluorescence in the bottom right corner as fluorescent fluid is pulled to the bottom of the channel. The void of fluorescence formed in the top left corner is the result of non-fluorescent fluid being pumped from the bottom to the top. This effect is minimal in a channel with a net axial flow, since in this case fluid does not stay at the edge of the array long enough to be moved across the channel by this localized effect. A similar effect of

rotating beads for pumping due to asymmetric channel geometry has already been recently described.[54] Within the array itself, the advancement of fluorescence across the channel occurs in pockets. This is likely due to irregularities in loading due to either extra or missing magnetic beads from positions.

Mixing under Flow

Additional work was done to investigate the effectiveness to mix two streams of fluid. Figure 5.4 contains still images recorded under differing *u* values for geometries utilizing the 6 μm circular feature with 8 μm space between the edges of each NiFe. Little mixing was observed by eye for a large range of *u* values.

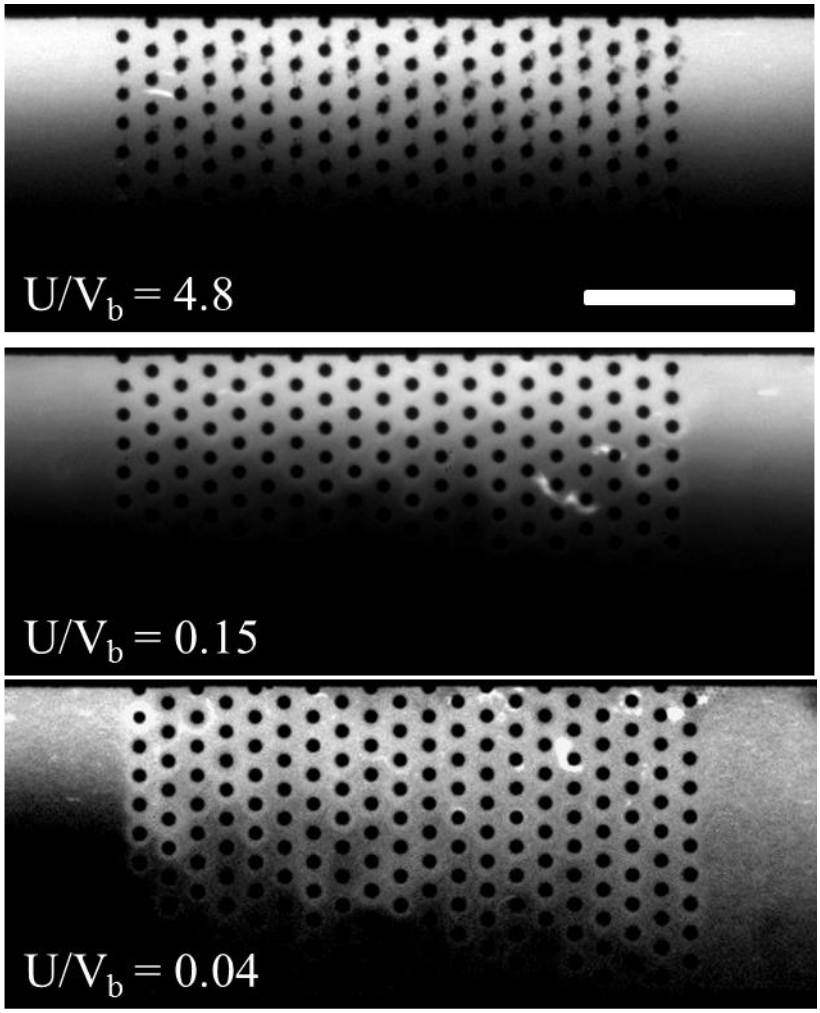

Figure 5.4 Images of the effect of the rotating magnetic beads on two streams of flow for various *u* values. Little mixing was observed by eye except for very low *u* values. Scale bar represents 100 μm.

However, strong mixing was observed by eye for very low values of *u* (Figure 5.4c) for the circular geometry. In the images of experiments utilizing the ellipses geometries, mixing was only observed in the horizontal ellipse. This mixing was observed only for the low *u* conditions, similar to what was seen in the circular features. The vertical ellipse saw no significant mixing even at low u values.

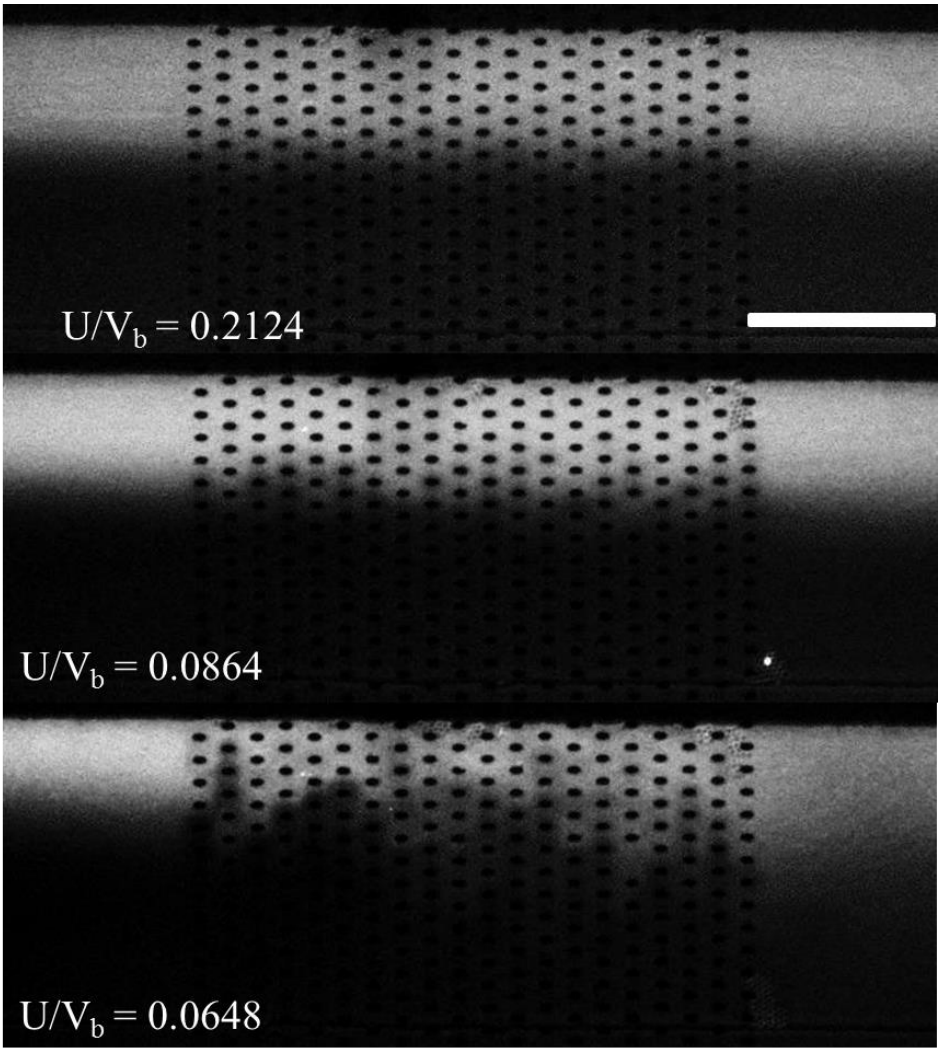

Figure 5.5 Images of the effect of the rotating magnetic beads on two streams of flow for various *u* values with the horizontal ellipse geometric array. Little mixing was observed by eye even for low *u* values.

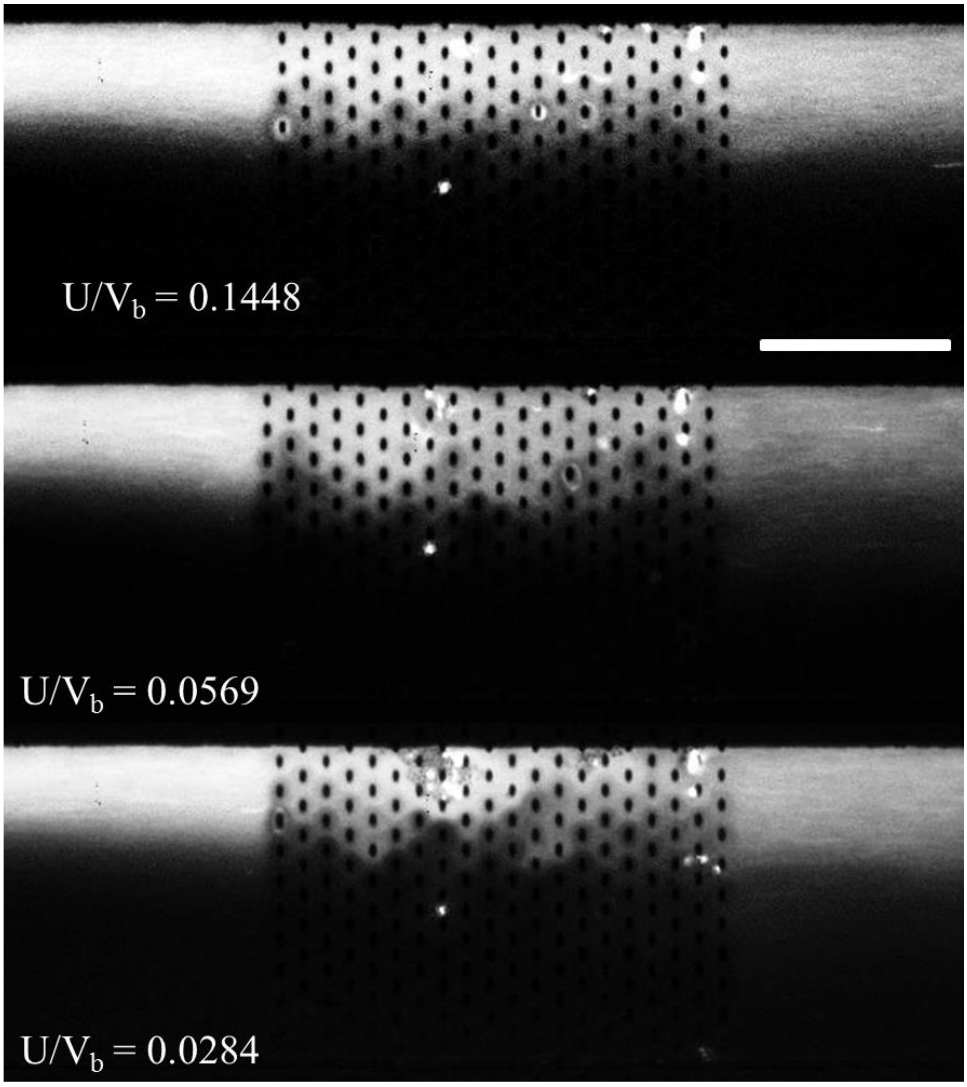

Figure 5.6 Images of the effect of the rotating magnetic beads on two streams of flow for various *u* values with the vertical ellipse geometric array. Little mixing was observed by eye.

A low *u* value corresponds to flow conditions where the speed of the magnetic microbeads is much faster than the linear velocity of the fluid particles. The area of the channel immediately after the array showed diffuse fluorescence across the entire channel width. This was in contrast to the stark regions of fluorescence and darkness in the regions immediately before the array. Similar to the effects seen in the stationary flow experiment, coronae of fluorescence surround the NiFe features. It was shown in previous mixing experiments with stationary flow that the rotation of the magnetic beads

transports fluorescence across the width of the channel creating additional coronae around NiFe features as it advances. Whereas under stationary fluid the fluorescence travels along a single column of NiFe features, under flow the fluid and fluorescence is pushed continually downstream and thus cannot travel along a single column. Instead, the fluorescent particles are pushed to the neighboring column where it is caught in the corona around the neighboring feature. As the fluorescence reaches each neighboring column some of it is transferred further across the width of the channel until it reaches the far channel wall.

For each set of flow conditions but one, multiple images (n=6) were taken of the section of the channel containing beads. To calculate mixing at the channel outlet, each image was cropped down to a 66 pixels wide by 225 pixels tall section representing the 20μm section of channel immediately after the array, and was imported into MATLAB for analysis. Each row of 66 pixels was averaged into a single intensity value to create an intensity profile across the width of the channel for each image. This averaging smooths any outlier intensity values that might result from a small cluster of nanoparticles or other non-uniformities in the flow. To further smooth out differences in fluorescent intensity across different experiments, curves were normalized to contain the same area. Each curve was normalized to the smallest area curve for that particular geometry.

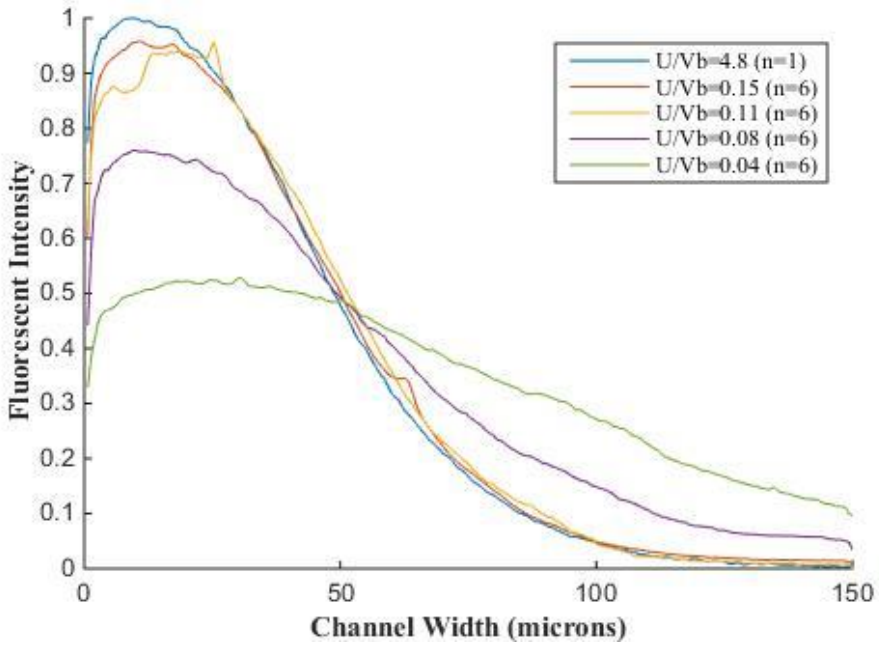

Figure 5.7 Plot of raw images of the mixed fluid created from the rotating magnetic beads in the circular array for various *u* values. Profiles were created by averaging the intensity profiles across the n number of images listed for each curve. The profiles begin to flatten as the fluid becomes more mixed, as the fluorescent intensity is more evenly distributed across the image.

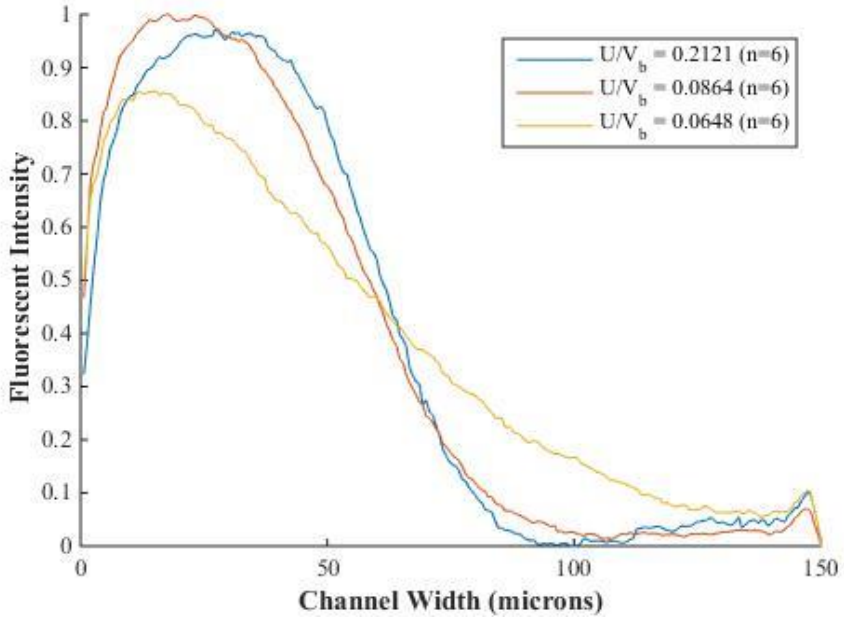

Figure 5.8 Plot of raw images of the mixed fluid created from the rotating magnetic beads in the horizontal ellipse array for various *u* values. Profiles were created

by averaging the intensity profiles across the n number of images listed for each curve. The profiles begin to flatten as the fluid becomes more mixed, as the fluorescent intensity is more evenly distributed across the image.

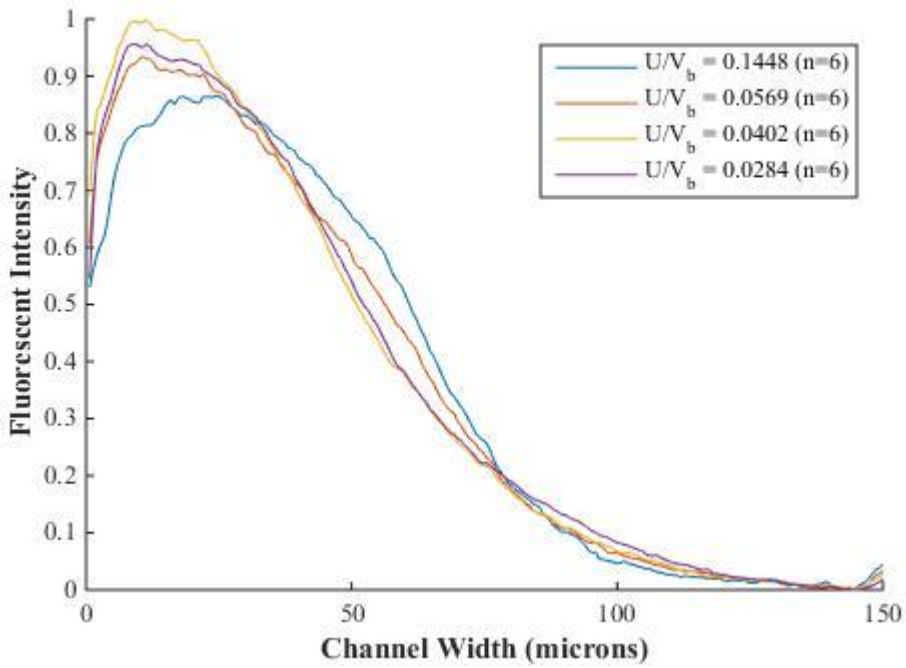

Figure 5.9 Plot of raw images of the mixed fluid created from the rotating magnetic beads in the vertical ellipse array for various *u* values. Profiles were created by averaging the intensity profiles across the n number of images listed for each curve. This geometry, the vertical ellipse, saw little flattening of the intensity profile curve for low u values.

The plots graphically represent the observed mixing, with the outlet region becoming more uniformly bright at the outlet with lower *u* values in some cases. Each of the individual n images from each curve in Figures 5.7, 5.8 and 5.9 were used to calculate mixing degree, σ, using the following equation

$$\sigma = 1 - 2\left(\sqrt{\frac{1}{N}\sum_{i=1}^{N}(\theta_i - \bar{\theta})^2}\right)$$

where θ_i is the fluorescent intensity at a point and $\bar{\theta}$ is the average fluorescent intensity across the entire channel. The multiplication by two and subtraction from one are to put the σ values on a range from 0 to 1, where 0 is perfectly unmixed and 1 is perfectly

mixed. The average σ values for each condition were plotted versus their respective *u* values and collected in Figure 5.10. Additionally, Lattice-Boltzman simulation data modeling the geometry of the circle array performed by Matthew Ballard is included in the array

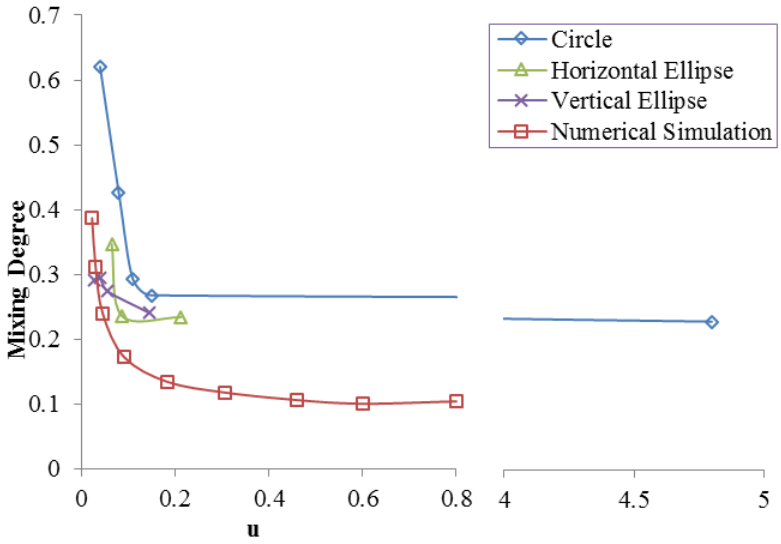

Figure 5.10 Plot of σ, mixing degree, values for the various mixing conditions attempted. Simulation data modeled the circle geometry with a perfectly unmixed fluid. The experimental curves could not be perfectly unmixed and account for the difference in baseline mixing. The important note is the sudden increase in mixing degree when $u<0.1$ which occurred in both simulation data and experimental conditions in two of the three experimental geometries.

Figure 5.11 zooms in on the low *u* region of the curve and plots the 95% confidence interval for each average mixing degree data point. The 95% confidence interval range was calculated as the average of the six images, plus or minus 2 standard errors. The equation for standard error used is

$$SE = \sqrt{\frac{SD}{n}}$$

where *SD* is the standard deviation of the data set and *n* is the number of points in the dataset.

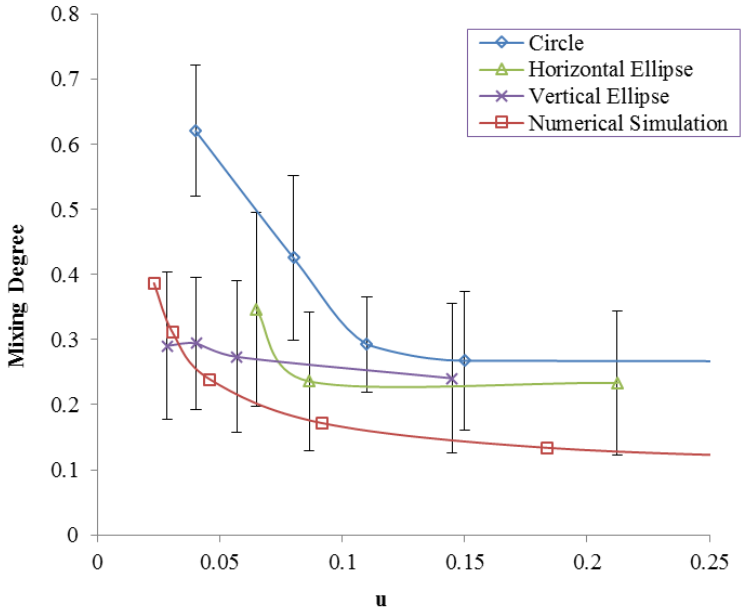

Figure 5.11 Plot of averaged mixing degree values including 95% confidence intervals, defined as plus or minus two standard errors.

These data show a stark increase in mixing for $u < 0.1$ for the circular and horizontal ellipse. The critical threshold of $u < 0.1$ was confirmed by Matthew Ballard using numerical simulation, utilizing a Lattice-Boltzman model, to be the result of transverse streamlines transporting fluid to neighboring features. No significant change in mixing degree was observed for the vertical ellipse configuration. The horizontal ellipse configuration saw a sharp increase in mixing degree when $u < 0.1$, similar to the effect seen in the 6 μm circle features. The purpose for studying mixing with the two different ellipses geometries was to identify which direction of the bead path is most crucial to induce mixing. It was originally hypothesized the vertical axis would lead to greater mixing because the magnetic bead motion is longest transverse to flow. These data did not support the hypothesis however further work is required before making any final conclusions. Several factors come into play with the differing ellipses geometries that need to be considered. First, in each ellipses geometry, the number of columns of features down the channel was fixed at 20. Put another way, a fluid particle traveling down the

channel would travel over 20 lines of ellipses. However, the different orientation of the ellipses result in a different length of the array. The vertical ellipse array covers a length of 212 µm down the channel while the horizontal ellipse covers a length 272 µm along the channel. This results in a longer effective residence time for a fluid particle to be in the region of the array. A second factor to consider is the density of the ellipse in the direction perpendicular to the flow. The horizontal ellipse array has 13-14 features across the width of the channel while the vertical ellipse array has 10-11 features spread across the channel width. The density of the actuating magnetic beads across the channel width is higher in the horizontal ellipse versus the vertical ellipse. A third variable that needs to be considered is the size of the interface between beads on neighboring features in the same column. The interface between features within the same column of the horizontal ellipses is 6 µm while the interface between features in the vertical ellipses is 3 µm. The increased interface could make it easier for particles to migrate or diffuse the short distance into the vicinity of neighboring magnetic beads for transport across the channel width. Taken together these factors require further study before definitive conclusions can be drawn between bead direction axes and mixing.

CHAPTER 6

CAPTURE OF PARTICLES IN A MICROFLUIDIC CHANNEL

Another application for the array of rotating magnetic beads is as a substrate for isolation and capture of cellular targets from microfluidic flow. It has been previously demonstrated that secondary flows can be generated inside a microfluidic channel via the rotating magnetic beads. The hypothesis of this work is that the secondary flows created by the rotating magnetic beads will increase the rate at which cellular targets will come into contact with the magnetic bead. Functionalizing the magnetic beads with a protein or antibody that binds to the cellular would then trap the cellular target to the magnetic bead. In the work described here, the same Dynabeads M-280 functionalized with streptavidin purchased from Life Technologies are used as the magnetic beads and the capture target are 1.0 μm Fluorspheres, available from Life Technologies. The Fluorspheres act as an analog for prokaryotic cells in size and are fluorescent, making them suitable for these early scale testing of the capture capacity of the rotating magnetic beads. The Fluorspheres are fluorescent latex particles with a surface functionalization of biotin. When the Fluorsphere comes in contact with the M-280, the bond between the streptavidin and the biotin simulate antibody-antigen binding.

A number of variables play a factor in determining the function of this system. The novel nature of this system however makes it difficult to predict the significance of any individual factor. This work will study the effect of three different factors on the effectiveness of capturing and isolating targets. The three factors investigated are the previously described flow ratio, *u*, the bead/channel height fraction and the spacing between the NiFe features.

Experimental Variables

Flow Ratio

The flow ratio, *u*, was previously found to have an important role in the mixing effectiveness of the rotating magnetic beads. That work showed that at low ratios, $u < 0.1$, significant mixing could be observed. For cell isolation and capture applications however, operating with a larger flow ratio would be more desirable. A larger ratio would make larger flow rates more feasible, which would be more applicable to sorting larger volumes of cellular targets more rapidly. Based upon the work done investigating the mixing effectiveness of the system, it is expected that lower *u* values will produce greater capture by introducing more contact between the magnetic beads and the cellular targets. The range of *u* values studied range from 0.05 to 0.5 and will be varied across spacing and bead/channel height fractions.

These experiments were performed using either EOF or gravity driven flow. As was mentioned in Chapter 5, it is difficult to accurately predict the linear flow velocity, U, in the channel. This value was calculated after the experiment utilizing time-lapse images and measurements of fluorescent particle path length. The U value of an experiment was calculated from averaging the measured path lengths of 4 particles over 4 seconds. The V_b value from an experiment is under strict control utilizing a stepper motor and encoder in combination to maintain a constant rotational speed of the field and by extension a constant velocity on the magnetic bead.

Bead Channel Height Fraction

It makes intuitive sense the effect of the rotating microbeads in a channel much taller than the microbeads will be much smaller. A simple way to consider this is the ratio of the diameter of the bead to the height of the channel. Thus this work defines a parameter *h*, where

$$h = \frac{diameter\ of\ magnetic\ bead}{height\ of\ microfluidic\ channel}$$

When the ratio is close to zero, the bead is insignificant compared to the entire volume. When the ratio is close to 1, the bead occupies almost the entire channel. A ratio close to zero is a poor choice because microbeads would have little effect on the fluid in the channel but a ratio close to 1 would likely have issue clogging when an actual complex sample is loaded. Further issues of availability and fabrication could constrain the size of the microbeads and it would be advantageous to know given a microbead diameter how tall could the fluid channel be and still be affected by the rotating microbeads. To better understand this, the ratio of bead diameter to channel height was varied. Bead height was kept constant and the channel height was varied by creating multiple molds via SU-8 microfabrication. The channel heights created were 5.8 µm, 9.3 µm and 12.1 µm. When compared with the magnetic bead diameter of 2.8 µm, these produce *h* values of 0.48, 0.30 and 0.23 respectively.

Spacing

The spacing between the magnetic beads has been investigated by varying the space between the rotating magnetic beads. The spacing is defined as the edge to edge spacing between rows and columns of NiFe features. The spacings studied here are 8 µm, 10 µm and 14 µm.

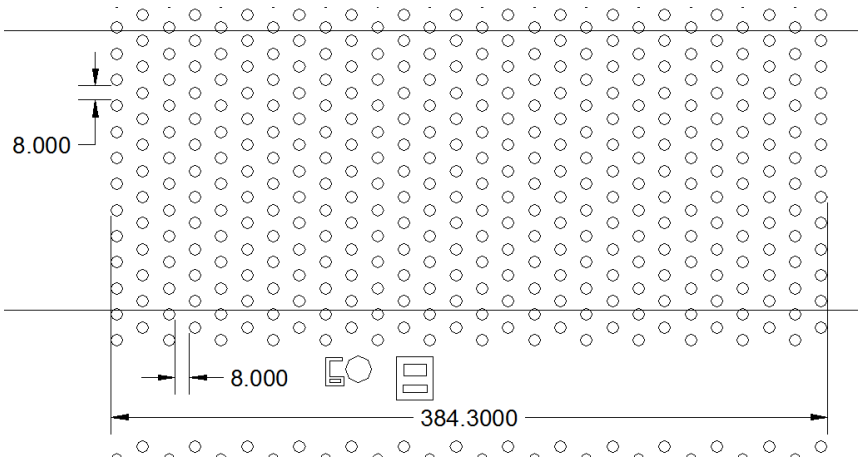

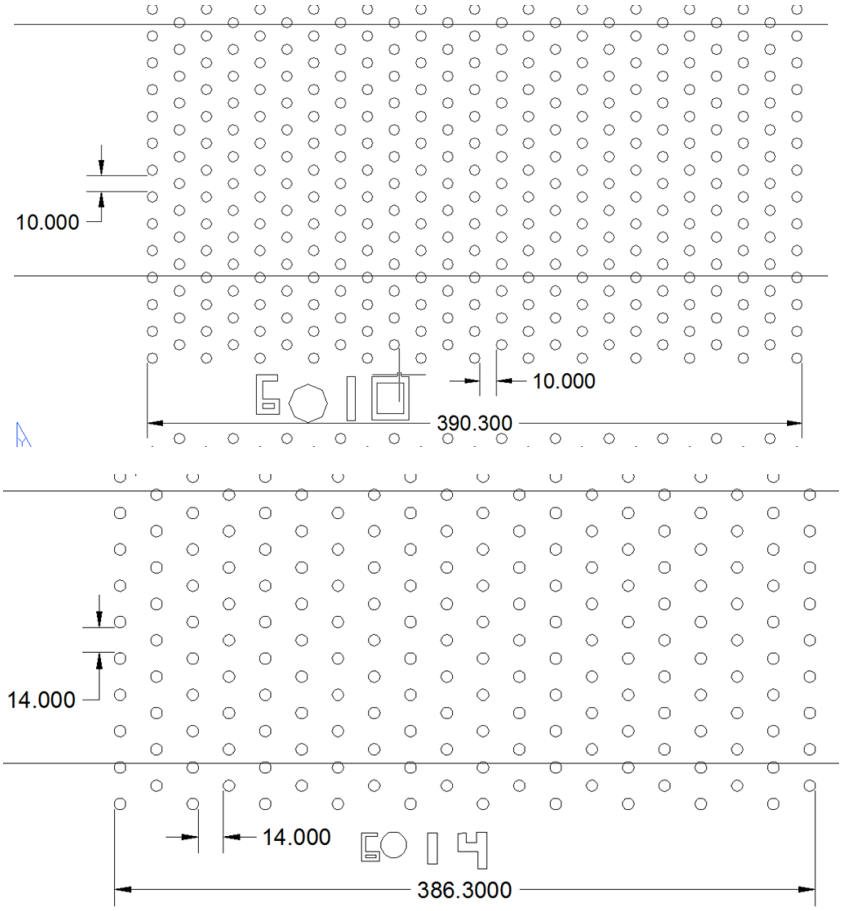

Figure 6.1 Different geometric spacings used for capture experiments. The total distance down the channel was held near constant and as such the total density of beads decreases with increasing spacing. The black lines represent the microfluidic channel over the array. The text is part of the design to make it easy to distinguish between different geometries on the wafer.

The total length down the channel occupied by the different geometries was held near constant. As such, each array has a different number of columns in the channel. This was done intentionally to create a residence time that is as uniform as possible across the different geometries. It was determined from previous experiments that if the spacing between features is too tight there are difficulties retaining captured targets. Previous experiments working with spacings of 6 µm saw an inability to hold on to the captured particles. The particle would appear to be captured and complete full circles around the

NiFe feature for a few frames and then become detached. Thus a wider spacing was chosen to allow for more stable capture.

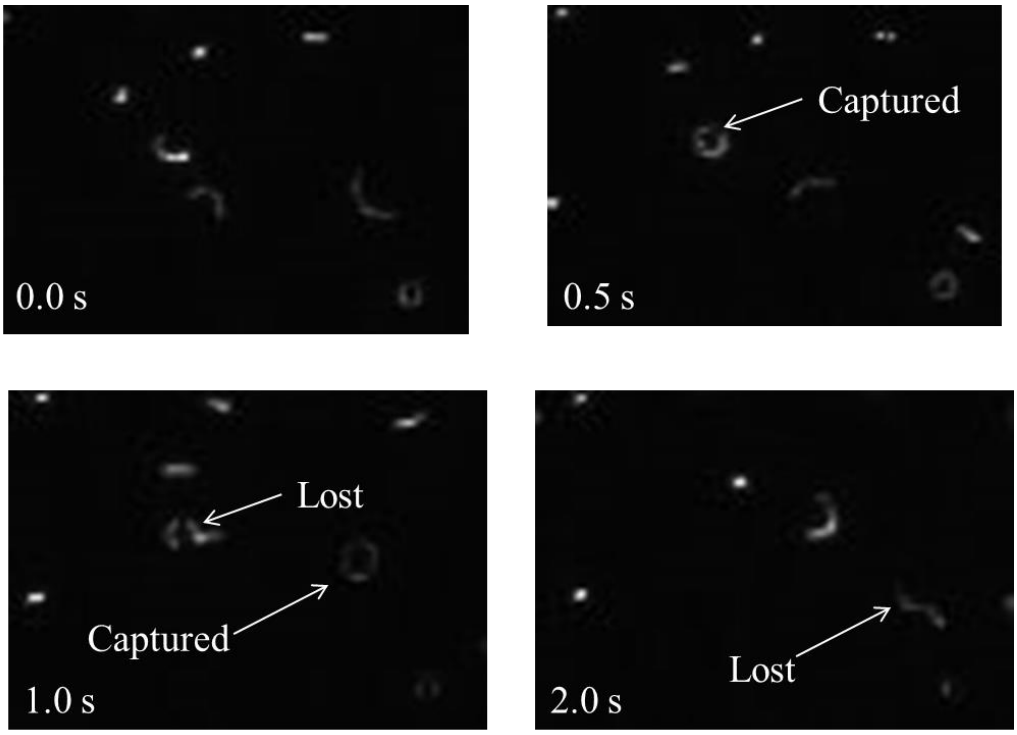

Figure 6.2 Captured particles were not held very well when using an array with a spacing of 6 µm. The particles would appear bound in a ring for a short time, usually one or two frames, before becoming detached. The number of bound particles at the end of experiments utilizing the 6 µm spacing was extremely low. The hypothesis for this low capture rate was bound fluorescent particles being hit by neighboring magnetic beads, as the spacing of 6 µm only has enough room for the two magnetic beads and no room for a 1 µm fluorescent particle.

Binding Strength

An issue of concern is the capacity of the streptavidin-biotin bond to withstand the drag created from rotation. That is will the rotation of the magnetic microbead create enough viscous drag force to mechanically break the bond. The Stokes drag equation previously described can be used to estimate the force on the fluorescent particle. µ is the dynamic viscosity of water, r is the radius of the fluorescent microsphere, and u is the velocity of the fluorescent microparticle. Assuming the fluorescent particle is traveling in

a 6 μm radius circle (the radius of the NiFe feature plus the diameter of the magnetic bead assuming the fluorescent particle is at the outer edge of the magnetic bead as it rotates) at 2,000 revolutions per minute then the drag force on the fluorescent particle is ~15 pN. Using atomic force microscopy (AFM), the measured bond strength of streptavidin-biotin is on the order of hundreds of piconewtons indicating the bond strength should be sufficient.[55]

Procedure

Assembly of the device, channel passivation and bead loading has been previously described in Chapter 2 (Further details available in Appendix B). For the capture experiments described here only three reservoirs are required: a M-280 magnetic bead loading reservoir, an outlet reservoir and a single inlet reservoir for the fluorescent particles. Magnetic beads were loaded into the array as previously described.

After loading the magnetic beads, the fluorescent particles were pumped into the array of rotating magnetic beads and time lapse images were recorded tracking the fluorescent particles (see figure 6.3). The time lapse images were used to count how many particles entered the array and how many became captured in the array. Every experiment used for data analysis had at least 20 particles enter the array and have the opportunity to be captured.

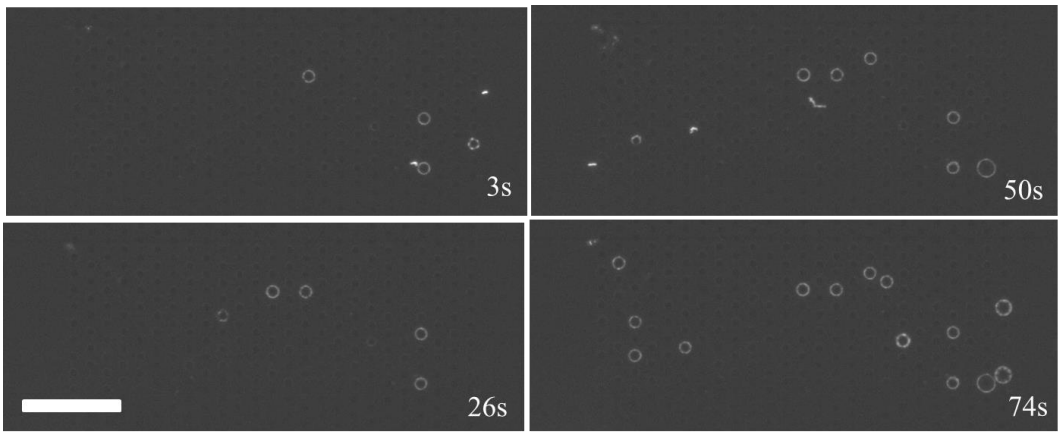

Figure 6.3 Fluorescent particles normally appear as small points of fluorescence and are easily tracked. Once the particles bind to a rotating magnetic bead however, they appear as fluorescent rings. The fluorescent particle now travels with the magnetic bead in a path around the NiFe feature at a high frequency compared to the exposure time (200ms). Scale bar represents 100 μm.

The number of particles captured was quickly calculated by subtracting the number of particles exiting the array from the number of particles entering the array. The number of particles entering and exiting the array was performed manually. This difference divided by the total number of particles entering the array gives the total number of particles captured. Using this difference instead actually counting the particles allows for more rapid analysis as the fluorescent particles captured can sometimes lose intensity and thus are difficult to track. Also, initial experiments showed some particles could move from the initial capture position making it difficult to keep an accurate count either manually or with software image analysis tools.

Preliminary Experiments

Buffer

This work initially used EOF for the pumping of the fluorescent particles. The fluorescent particles are biotin coated 1μm Fluorspheres Yellow-green (505/515). The fluorescence of these particles is visible via FITC excitation and emission fluorescent cubes. The concentration of the fluorescent particles pumped through the system is

$18*10^6$ particles/mL. This is a x1000 dilution from the stock vial solution. The particles were initially diluted in the 0.1% BSA in DI water solution used to passivate the channel and load magnetic beads. This solution was demonstrated to prevent non-specific adsorption while also being compatible with EOF pumping.

The results from these experiments showed inconsistent results. No strong trend was determined from the data.

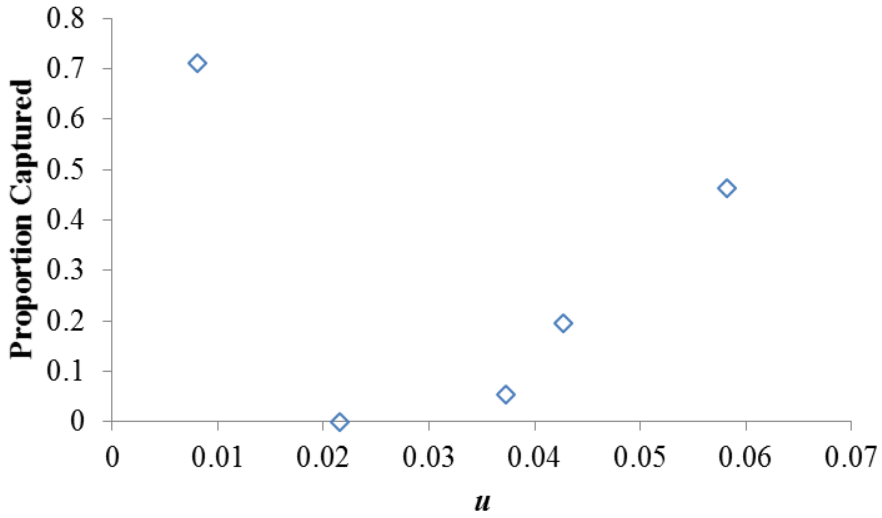

Figure 6.4 Plot of proportion of particles captured versus flow ratio, *u*. The data showed inconsistent results even in very small differences in *u*.

To test if the protein binding and capture was hindered by the applied voltage, more experiments were performed using pressure driven flow. This was accomplished by overfilling the fluorescent particle reservoir. The static pressure head proved capable of generating linear flow velocities on the order of 10 μm/s. Results from these experiments proved more consistent but still yielded very low capture efficiencies of ~20% captured. Close examination of these videos however revealed that a significant number of particles appeared to become captured, forming the characteristic ring of fluorescence, before becoming detached and exiting the array. Under the current counting algorithm these particles would be considered not captured. Further analysis was performed on four of the

videos from the gravity fed experiments to count of the particles that exited the array, how many had been captured for a short time. A short time was defined as the formation of a single ring for once complete frame. One frame represented approximately 0.4 seconds or 13 revolutions of a bead rotating at 2,000 rpm.

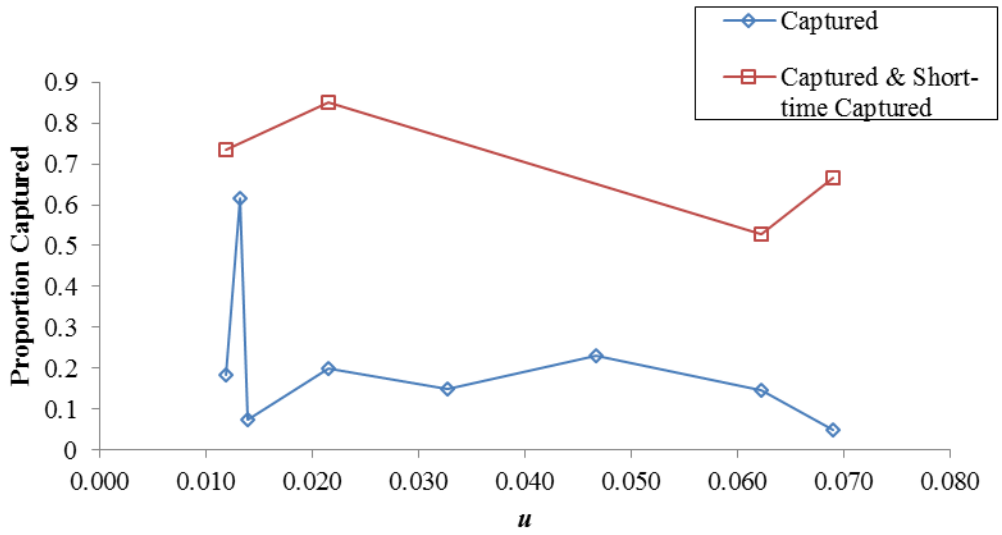

Figure 6.5 Proportion of particles captured using gravity driven flow and the DI H_2O + 0.1% BSA buffer. Particles were not captured well by the rotating beads. However, inspection of videos showed numerous particles appearing to be captured for a short time then releasing. Including these particles in the counting showed a drastic increase in the capture rate.

Using this requirement, many of the particles that exited the region were captured for a short time. Combining these particles with the captured particles, the percentage of total fluorescent particles captured for any period of time is ranges from 53%-85% in the four experimental conditions. This indicates that a significant number of fluorescent particles are coming into contact with the magnetic beads but are failing to stay bound.

Based upon this it was hypothesized that the buffer was not creating an environment for optimal binding. The use of a pressure-drive system fed by gravity makes it possible to introduce PBS into the channel without it blocking the EOF pumping effect. Thus these experiments were repeated except the fluid used to dilute the

fluorescent particles was PBS with 0.1% Tween-20, a common surfactant to keep non-specific adsorption low. These experiments show a much improved binding capacity to capture particles. Figure 6.6 shows the capture percentages for each of the three buffers used.

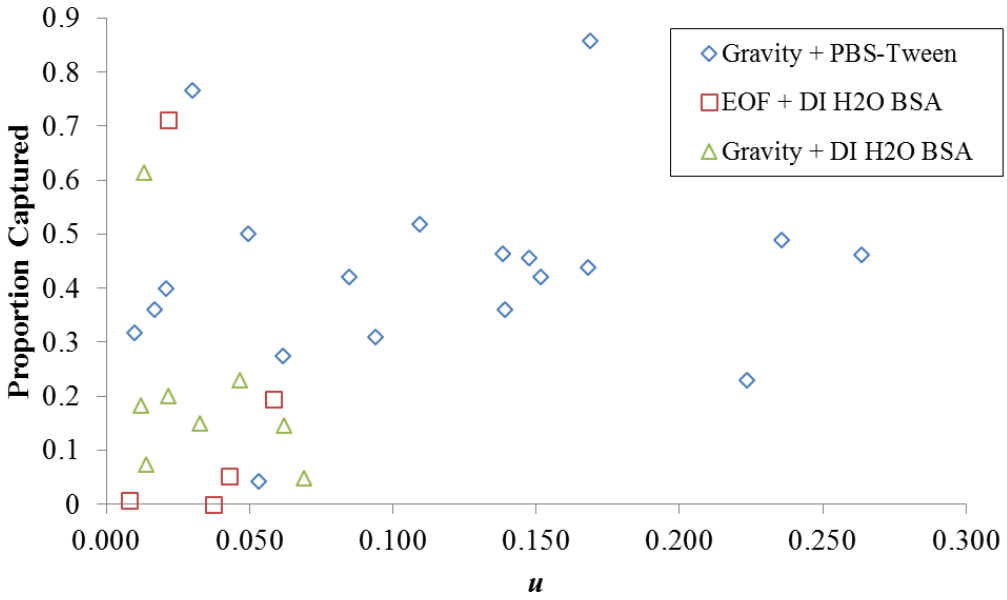

Figure 6.6 Plots of capture proportion versus *u* for different buffers. With a few outliers, the combination of PBS-Tween as a buffer and pumping by gravity showed the best capture rate.

These data do not include the particles that were caught for a short time then released. The important feature of this figure is the clustering of the capture percentages. The DI H_2O with BSA pumped via EOF exhibited very poor capture efficiency and the DI H_20 with BSA with pressure driven flow appears slightly better. The clustering of the PBS + Tween experiments indicates that the binding in DI H_2O was inherently poor and PBS was required to achieve more accurate results.

Further analysis of this data was performed to determine if the results seen in Figure 6.6 are significantly different. The data was imported into R (version 3.2.3, see Appendix D for code utilized) and then fit to a linear model with categories for different

buffer types. Analysis of variance (ANOVA) was performed on the linear fit and the results of the ANOVA are presented below.

```
Analysis of Variance Table

Response: capture
          Df  Sum Sq  Mean Sq F value  Pr(>F)
u          1 0.06775 0.067749  1.7213 0.19982
buffer     2 0.23010 0.115048  2.9230 0.06975 .
Residuals 29 1.14143 0.039360
---
Signif. codes:  0 '***' 0.001 '**' 0.01 '*' 0.05 '.' 0.1 ' ' 1
```

Figure 6.7 ANOVA Table from R documenting the probability of achieving the distribuion of data found in Figure 6.6 if the listed parameters (*u* and buffer type) are not significant. The analysis reveals that the differences in the data due to buffer are significant to the $\alpha = 0.1$ level.

The analysis of variance table indicates that the *u* value is not statistically significant at predicting the capture proportion for the buffer data given, assuming all three data sets are not statistically significant. The same calculations indicates that the category of buffer for the dataset is predictor for capture proportion to an α significance of 0.1. Separating the data into two groups, one of PBS + Tween and the other as DI H_2O + BSA and applying the same analysis indicates the two groups are statistically significant to $\alpha = 0.05$. This gives further proof to the observation that PBS + Tween as a buffer improved capture in the device.

Negative Control

To confirm the binding observed in the capture experiments is a real event, a negative control was performed utilizing magnetic beads that have the streptavidin coating neutralized as much as possible. A 100 µL 1:20 dilution of the stock M-280 magnetic bead solution in DI H_2O + 0.1% BSA was made and stored in a 600 µL conical tube. The tube was placed in a 95 ^{o}C bath of water for 1 hour. The tube was then placed under a UV lamp (Blak-Ray, Long Wave UV Lamp, Model B-100 A, 115V, 60 Hz,

2.5A) for 30 minutes before returning to the 95 °C water bath for another hour. These beads were loaded into an array. The standard 1:1000 dilution of fluorescent particles was made using DI H_2O + 0.1% Tween and an experiment was recorded. Over the course of the experiment, a total of 53 particles entered the array and all 53 exited the array, for a capture proportion of 0. The flow ratio for this experiment was 0.034. The capture rates for the three data points nearest in *u* using this geometry averaged a capture proportion of 0.55.

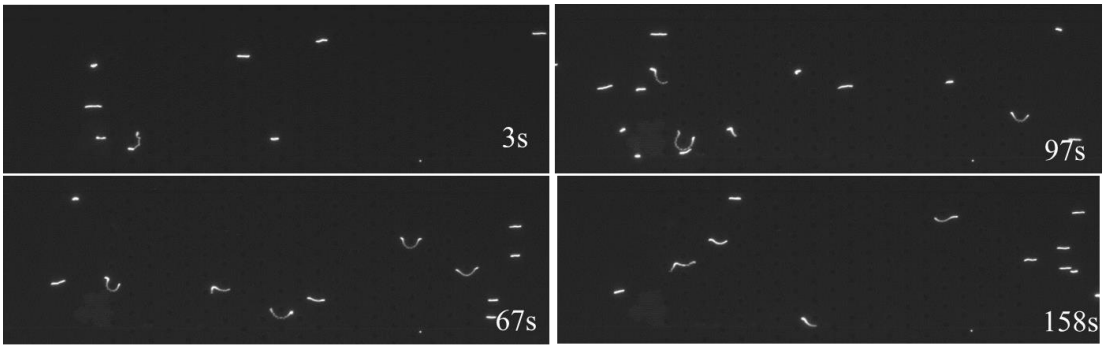

Figure 6.8 Images of a negative control experiment utilizing magnetic beads with an heat and UV light denatured protein coating. During the experiment, 0 out of 53 particles were captured (0% capture proportion). This indicates that the capture observed with unmodified magnetic beads is an actual event.

Effect of Spacing on Capture

For each of these geometries capture experiments were performed with a constant bead/channel height fraction of 0.48 (channel height of 5.8 μm). The videos were recorded and plotted in Figure 6.11 are the total captured for each of the different spacings.

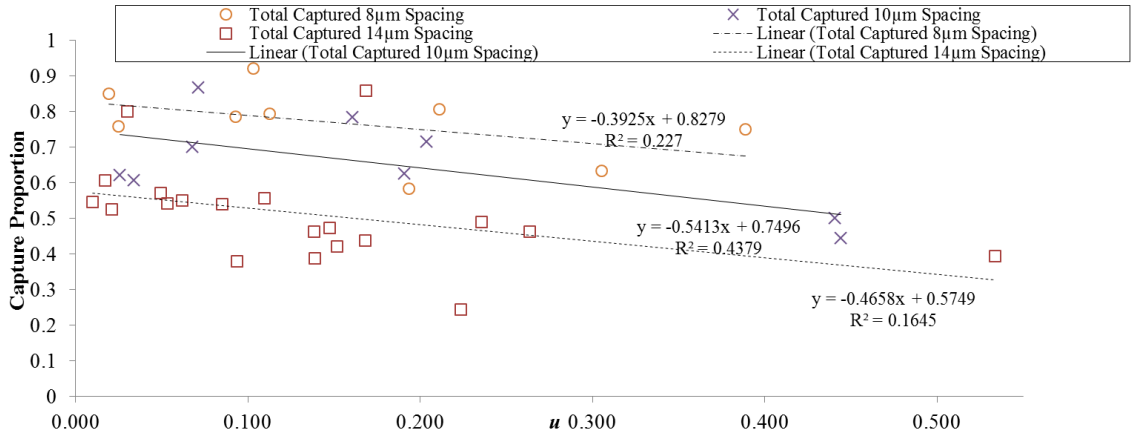

Figure 6.9 Plot of the total captured particles (captured and short-time captured) for various *u* values for three different geometric arrays. While there is strong variability amongst the data some general trends can be observed.

Three general trends are visible across each data set. First, the best total capture tended to occur with very low values of *u*. This agrees with the hypothesis that the induced secondary flow created by the magnetic beads increases the likelihood of a fluorescent particle coming into contact with the magnetic bead and having the opportunity to bind. Second, at a given value of *u* the tighter spacing leads to more binding and capture. This second observation also agrees with intuition that a tighter spacing yields a higher magnetic bead density. The third observation is that the capture rate is weakly dependent upon *u* for all three spacings in the range of *u* values investigated. All three data sets have a slope ranging from -0.54 to -0.39. These slopes correspond to a relationship between capture proportion and the value of *u*. These trendlines for the data are roughly parallel across all three geometries. The major differences between the curves the y-intercept value.

To determine the significance of these observations, the data was again imported into R to test the significance of the data sets. Table 6.3 Represents the ANOVA table calculated via R (code for analysis in Appendix D).

```
Analysis of Variance Table

Response: capture
          Df  Sum Sq  Mean Sq F value    Pr(>F)
u          1 0.04762 0.047618  3.5642   0.06735 .
spacing    2 0.49204 0.246018 18.4146 3.435e-06 ***
Residuals 35 0.46760 0.013360
---
Signif. codes:  0 '***' 0.001 '**' 0.01 '*' 0.05 '.' 0.1 ' ' 1
```

Figure 6.10 ANOVA Table from R of capture proportion data for the three different spacings investigated. The analysis indicates that spacing is a signifier of significance for predicting capture proportion based on *u* to $\alpha = 0.001$.

This data indicates that the spacing of the features is significant to $\alpha = 0.001$ when predicting capture proportion when using *u*. Utilizing the summary of the entire data, it is possible to see how individual spacing geometries compare. Note, in this analysis R utilizes the 8 µm spacing geometry as the reference data set for comparison.

```
Call:
lm(formula = capture ~ u + spacing, data = myspacing)

Residuals:
     Min       1Q   Median       3Q      Max
-0.23782 -0.06382  0.00093  0.04118  0.35692

Coefficients:
               Estimate Std. Error t value Pr(>|t|)
(Intercept)     0.83144    0.04460  18.642  < 2e-16 ***
u              -0.34886    0.10524  -3.315  0.00214 **
spacingfourteen -0.27235    0.04618  -5.897 1.05e-06 ***
spacingten     -0.11693    0.05349  -2.186  0.03559 *
---
Signif. codes:  0 '***' 0.001 '**' 0.01 '*' 0.05 '.' 0.1 ' ' 1

Residual standard error: 0.1156 on 35 degrees of freedom
Multiple R-squared:  0.5358, Adjusted R-squared:  0.496
F-statistic: 13.46 on 3 and 35 DF,  p-value: 5.312e-06
```

Figure 6.11 Summary of linear model fit from R to capture data for different spacings. The reference data set was the 8 µm spacing geometry. This analysis indicates that the 10 µm and 14 µm spacing arrays are statistically significant to $\alpha = 0.01$ and $\alpha = 0.001$, respectively.

These results show that the 10 µm and 14 µm spacing geometries are statistically significant to $\alpha = 0.01$ and α essentially zero respectively when compared to the 8 µm spacing geometry. A second ANOVA is performed between just the 10 µm and 14 µm spacing geometries to determine the significance between those two data sets.

```
Analysis of Variance Table

Response: capture
          Df  Sum Sq  Mean Sq F value   Pr(>F)
u          1 0.08039 0.080391  5.4887 0.027067 *
spacing    1 0.15929 0.159288 10.8753 0.002824 **
Residuals 26 0.38081 0.014647
---
Signif. codes:  0 '***' 0.001 '**' 0.01 '*' 0.05 '.' 0.1 ' ' 1
```

Figure 6.12 ANOVA table from R comparing the statistical difference between the 10 µm and 14 µm spacing geometries. This analysis indcates that the capture proportion data from the two different geometris is statistically significant to $\alpha = 0.01$.

This ANOVA results indicate that the 10 µm and 14 µm spacing geometries are also statistically significant to the $\alpha = 0.01$ level.

Effect of Spacing on Clumping

One major issue discovered with these different geometry experiments was the clumping together of magnetic beads after the fluorescent particles have been introduced. Images of the array before and after capture show this effect.

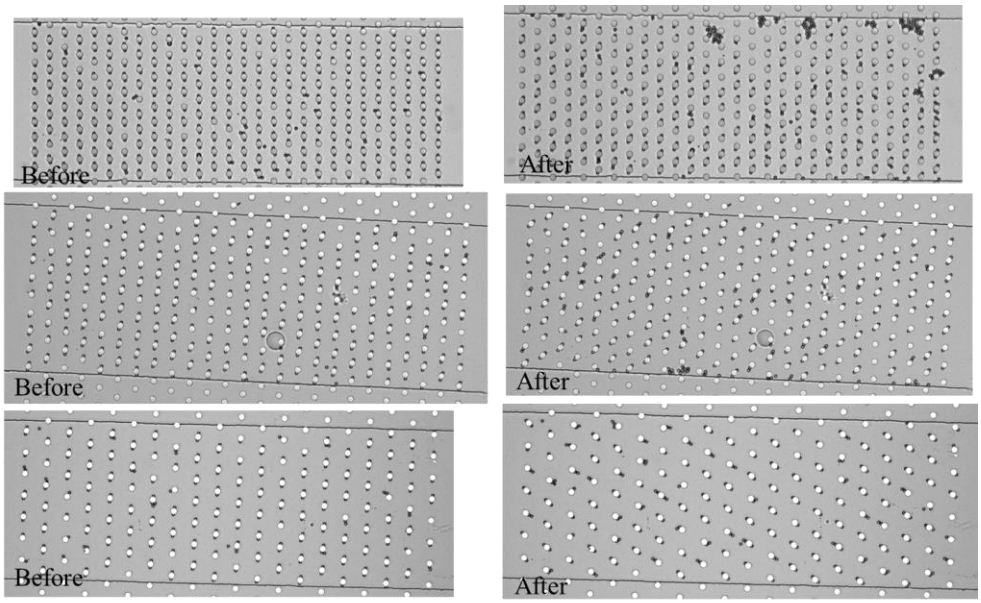

Figure 6.13 Before and after images of three different experiments with three different geometries. The tighter the spacing the more clumping was observed. Clumps of magnetic beads also tended to collect near the walls of the channel.

The clumping appears to worsen with the smaller spacing. Over time, some arrays would have such large degree of clumping that the array loses the capacity to interact with the fluid. A potential reason for this could be the fluorescent particles themselves acting as an adhesive between neighboring magnetic beads. Under ideal conditions there would be no interaction between the neighboring magnetic beads with bound fluorescent particles. The 8 μm spacing between the NiFe features can accommodate two 2.8 μm beads and two 1 μm fluorescent particles with clearance. However, it is very difficult to completely remove all excess beads and the presence of a small number of them could lead to clumping problems. These clumped beads are no longer actuated by the magnetic field so it is unlikely that they would be released upon removal of the magnetic field.

Height Dependence

A single geometric array, the 10 μm spacing between features, was used to study the influence of the bead diameter/channel height ratio. The values of *h* are 0.48, 0.30 and

0.23 (corresponding to channel heights of 5.8 µm, 9.3 µm and 12.1 µm). A plot of the total capture proportion in these experiments is presented in Figure 6.13.

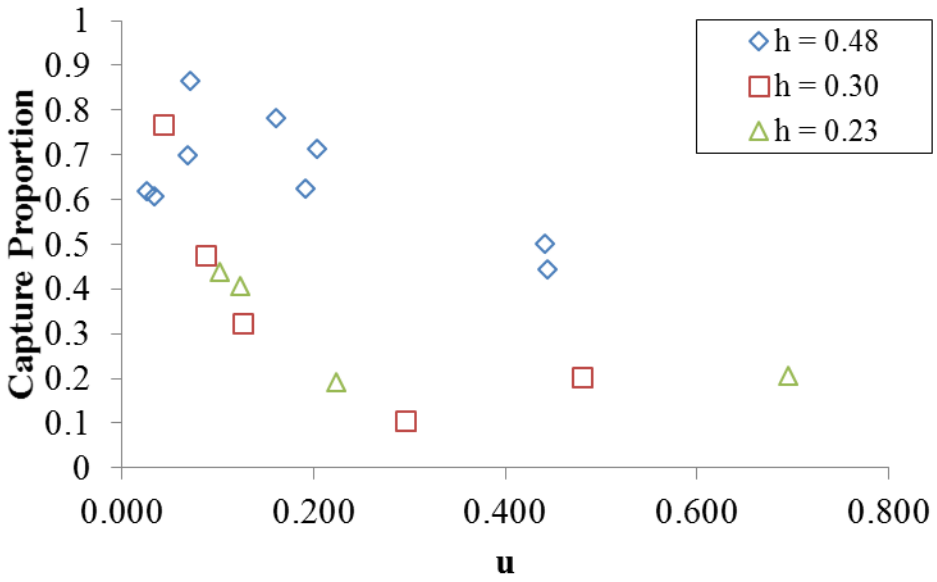

Figure 6.14 Plot of total captured versus *u* for three different *h* values. The geometry used was the 10 µm spacing array. In the experiments where the magnetic bead occupied a 30% or less of the total channel height, the capture proportion exhibited a non-linear relationship. This is in contrast to the shorter channel height experiment which exhibited a linear relation.

The $h = 0.48$ data is repeated from the previous experiments but the other ratios represent new data. The two smaller *h* values exhibited a markedly different shaped curve from what was seen in the larger height ratio. The $h = 0.48$ data was shown to exhibit a roughly linear trend with a slope of -0.54 (capture proportion/*u*). In the two lower *h* cases the data exhibits a logarithmic trend. The capture proportion decreases to an asymptotic level of approximately 0.2 captured with increasing *u* values. When $u < 0.20$, the capture proportion increases rapidly with decreasing *u* values. A small *u* value represents a condition where the magnetic beads are moving much faster than the bulk fluid. This effect indicates that the rotation of the magnetic beads does improve the capture rate of

the array. Current work is being done by Matthew Ballard to model the fluid behavior inside this channel and ascertain the exact cause of this effect.

To investigate the significance between the data sets, a quadratic regression was applied to the data for capture proportion for different heights. To simplify the analysis, the data was separated into two groups, one containing the h=0.48 data and the second group containing the h = 0.30 and h=0.23 data. The name of the category was called line.

```
Analysis of Variance Table

Response: capture
          Df  Sum Sq Mean Sq F value    Pr(>F)
u          1 0.29788 0.29788 17.9204 0.0008348 ***
I((u)^2)   1 0.02004 0.02004  1.2057 0.2907180
line       1 0.33503 0.33503 20.1553 0.0005094 ***
Residuals 14 0.23271 0.01662
---
Signif. codes:  0 '***' 0.001 '**' 0.01 '*' 0.05 '.' 0.1 ' ' 1
```

Figure 6.15 ANOVA table from R of capture proportion data for varying *h* values. The ANOVA data indicates there is a significant difference between the two types of data in the line category. The line category is separated into the *h* =0.48 (reference set) data in one part and the combined *h* = 0.30 and *h* = 0.23 data in the other part The significance level was $\alpha = 0.001$.

An additional analysis between the *h* = 0.30 and *h* = 0.23 data revealed little statistical difference between the data sets.

```
Analysis of Variance Table

Response: capture
          Df   Sum Sq  Mean Sq F value  Pr(>F)
u          1 0.138736 0.138736 14.3764 0.01274 *
I((u)^2)   1 0.131982 0.131982 13.6765 0.01403 *
height     1 0.009601 0.009601  0.9949 0.36433
Residuals  5 0.048251 0.009650
---
Signif. codes:  0 '***' 0.001 '**' 0.01 '*' 0.05 '.' 0.1 ' ' 1
```

Figuree 6.16 ANOVA table from R comparing significance of difference between *h* =0.30 and *h* =0.23 values. No significance difference can be found between the two data sets.

It is possible that the diffference in height fraction between these two experiments was not significant enough to demonstrate a difference in the acapturing efficiency of the system. Further work could be done to investigate with different channel height fractions to identify statistically significant differences in the data.

Variability in System

The dynamic nature of this device leaves it open to potential sources of variability from one experiment to the next. One potential source comes from the loading of the magnetic beads. It is very difficult to insure perfect loading of the magnetic beads (a single bead at each induced pole in every NiFe feature) because of the lack of direct control of bead distributions. Increasing the magnetic field rotation to over 4,000 rpm while under flow was seen to through off many excess magnetic beads but was not a guarantee of perfect distribution.

Calculation of Flow Ratio

The calculation of the flow ratio, *u*, has some inherent instability. This instability comes from the determination of the numerator of the ratio, U, the linear flow velocity. The magnetic bead velocity, V_b, is kept very stable by the stepper motor and encoder used to keep the beads rotating at a constant rate around a fixed path. The variability in U primarily stems from the distribution of the linear velocity values experienced by the fluorescent particles. The linear velocity is calculated from measuring the path of the linear particles over as many frames as possible in the region of the channel prior to the array of magnetic beads. This path length is combined with the time stamps of the frames to determine the linear velocity of the particle and by extension the linear velocity of the fluid flow. Typically, this measurement and calculation is performed manually, due to the unstable frame rate of the camera capture and non-standard intervals between images taken. The manual nature of the measurement necessitates only measuring a subset of the

total particles entering the array and using the average velocity of this subset. To demonstrate the potential range of U values, the velocity of every particle in three experiments was measured. All of these particles were measured in the region upstream of the magnetic array. The three videos selected represent the range of estimate U values.

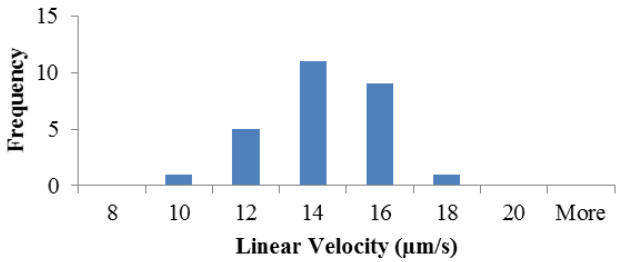

6.17 Histogram of all calculated U values from an experiment were the estimated U = 12.2 µm/s. Average of all measured velocities was 13.2 µm/s with a standard deviation of 1.9 µm/s.

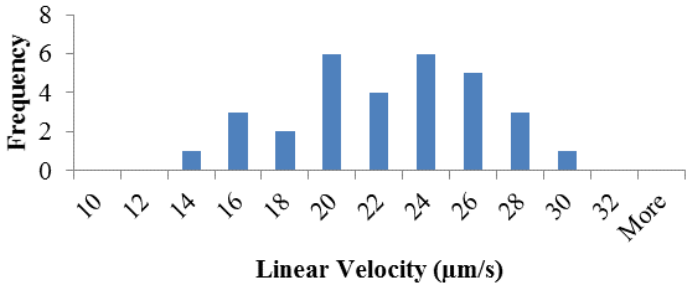

6.18 Histogram of all calculated U values from an experiment were the estimated U = 24.8 µm/s. Average of all measured velocities was 21.8 µm/s with a standard deviation of 3.8 µm/s.

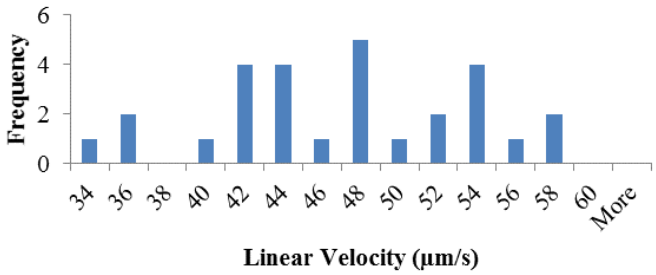

6.19 Histogram of all calculated U values from an experiment were the estimated U = 50.1 µm/s. Average of all measured velocities was 46.1 µm/s with a standard deviation of 6.6 µm/s.

In each of these experiments, the estimated U value for each experiment was within one standard deviation of the measured average. However the range of potential U values could vary by as much as a factor of two. If the V_b velocity is low then this, variability in U could lead to a large deviation in *u*.

It is important to note that the variability in the *u* value has no effect on the capture proportion for a given experiment. The number of captured particles is calculated independent of the *u* value. The variability in *u* only affects the position of the data point across the x-axis. This is important in developing a model relating *u* and the capture proportion and should be considered.

Binding Stability

Investigation of the time bound for particles bound to magnetic beads was investigated for three different experiments. This was done by manually counting the number of frames the particle remained bound before detaching from the magnetic bead. This data was recorded in Figure 6.14. The data shows a rough bell curve centered at a binding time of ~1.5s. The resolution of the binding times is hampered by the frame rate of the camera utilized to record the fluorescent images. The camera could only capture at a rate of approximately 2 frames per second.

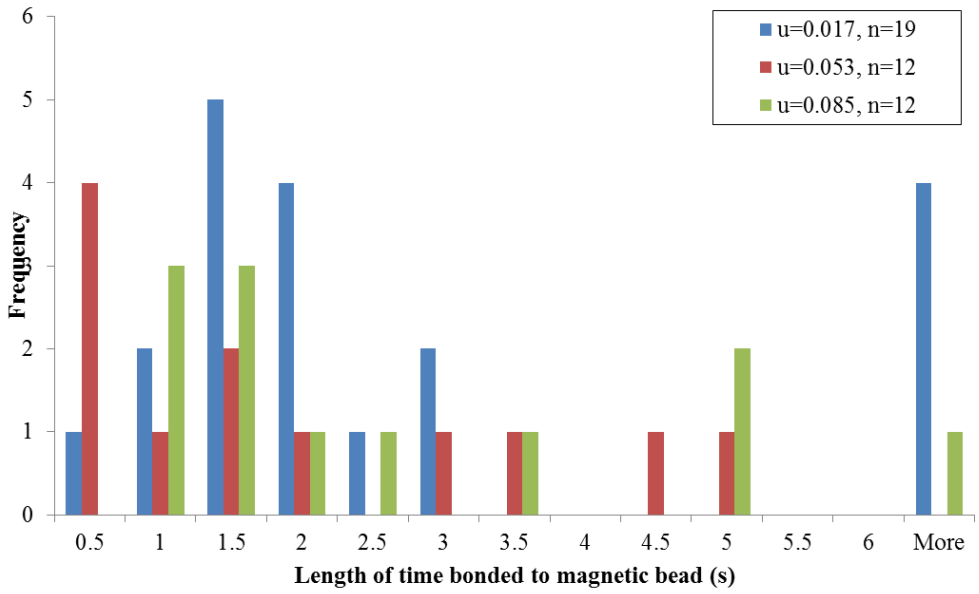

Figure 6.20 Histogram of length of binding times for short time captured particles. Data demonstrates a rough bell curve shape centered at a 1.5 second bond time.

While inspecting the PBS +Tween buffered experiments for particles that were captured for a short time, it was observed that the greatest number of short time captured particles occurred at low *u* ratios (Figure 6.21). This suggested that something was happening at low ratios to weaken the binding. (Figure 6.22)

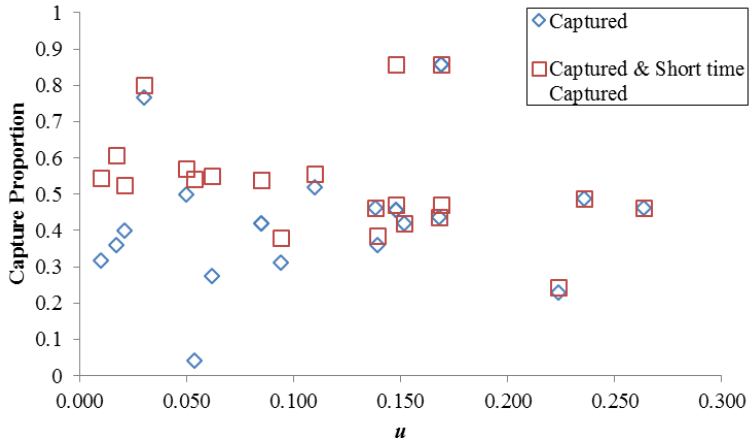

Figure 6.21 The capture rate when considering stably captured particles only and the capture rate when considering stably captured particles plus particles captured for a short time.

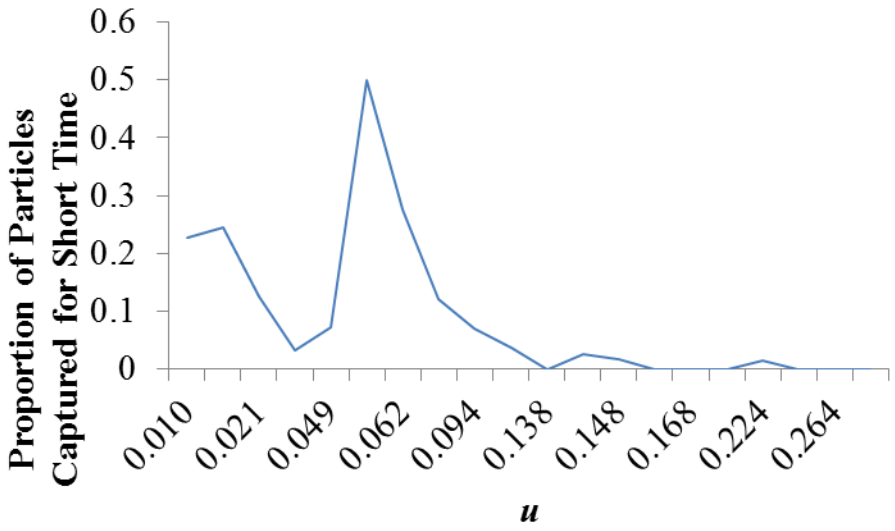

Figure 6.22 Plot of proportion of total particles only captured for a short time. These data indicate that the rate of particles captured for a short time decreased with increasing *u* value.

The ratio *u* is composed of two different velocities, the linear flow velocity and the magnetic bead linear velocity. These data was plotted versus each these factors to determine if there is a relationship between either of the velocities and the discrepancy.

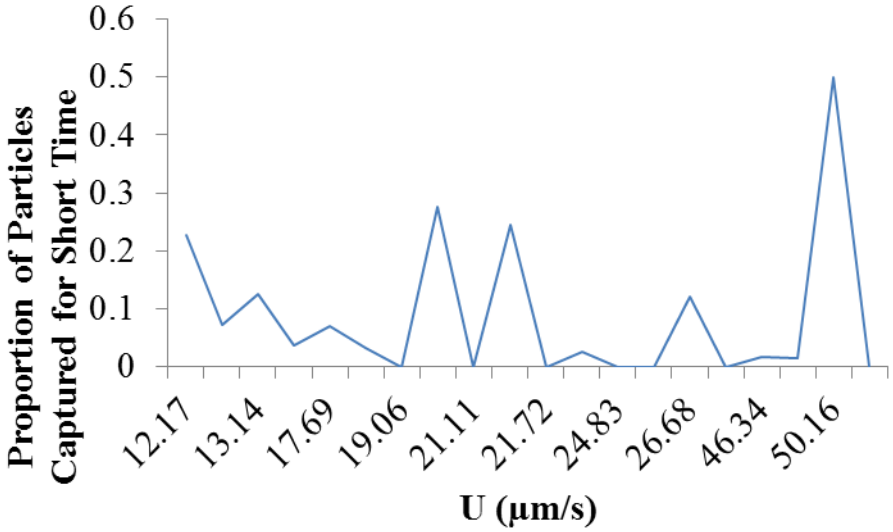

Figure 6.23 Plot of the proportion of short-time captured particles versus linear flow velocity of the bulk fluid. Note the x-axis is not equal spacing between data points.

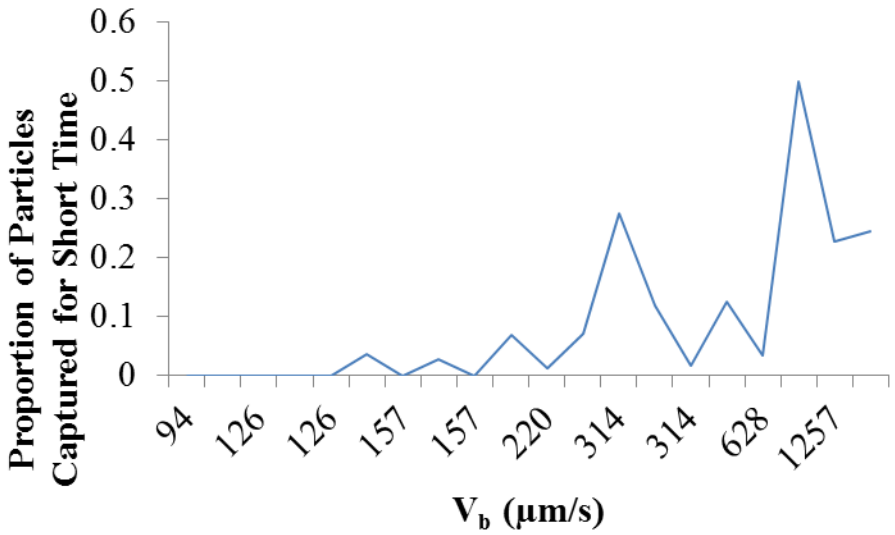

Figure 6.24 Plot of the proportion of short-time captured particles versus magnetic bead linear velocity. Note the x-axis is not equal spacing between data points.

The plot of capture and short time capture versus linear flow velocity showed very little pattern. The plot of capture and short-time capture showed that the largest difference between the two occurred in conditions where the magnetic bead velocity was more than 300 µm/s. This data was investigated using a t-test to determine if the data exhibited any significance. First the data was separated into two groups using U = 40 µm/s as a cutoff. The results of the t-test are presented Table 6.1.

Table 6.1 T-test results of short-time captured proportion, sorted by linear flow velocity, U. The t-Stat < t Critical two-tail, indicates the null hypothesis cannot be rejected and there is no difference between the data with $\alpha = 0.05$ significance. The linear flow velocity does not appear to have any significant effect on the proportion of short-time captured particles.

t-Test: Two-Sample Assuming Unequal Variances
using U = 40 μm/s cutoff, $\alpha = 0.05$

	U > 40 μm/s	*U < 40 μm/s*
Mean	0.132378378	0.076912843
Variance	0.060114158	0.009078226
Observations	4	16
Hypothesized Mean Difference	0	
Df	3	
t Stat	0.444137646	
P(T<=t) one-tail	0.343513342	
t Critical one-tail	2.353363435	
P(T<=t) two-tail	0.687026684	
t Critical two-tail	3.182446305	

The t-test results show that the linear flow velocity has no significant effect when separating the data into two sets, separated by a cutoff value of U = 40 μm/s, at a confidence level of 95%. The data was then organized according to magnetic bead velocity, V_b and grouped into two sets using V_b = 300 μm/s as the cutoff between the two groups.

Table 6.2 T-test results of short-time captured proportion, sorted by magnetic bead velocity, V_b. The t-Stat > t Critical two-tail, indicates the null hypothesis can be rejected and there is a difference between the data with $\alpha = 0.05$ significance. The linear flow velocity appears to have any significant effect on the proportion of short-time captured particles.

t-Test: Two-Sample Assuming Unequal Variances
using V_b = 300 μm/s cutoff, $\alpha = 0.05$

	V_b>300μm/s	V_b<300μm/s
Mean	0.192813462	0.018134275
Variance	0.024531624	0.000743412
Observations	8	12
Hypothesized Mean Difference	0	
df	7	
t Stat	3.123055815	
P(T<=t) one-tail	0.008385916	
t Critical one-tail	1.894578605	
P(T<=t) two-tail	0.016771831	
t Critical two-tail	2.364624252	

The results of this t-test confirm the observation that there is a correlation between the velocity of the magnetic beads and the rate of short-term captured particles. This makes intuitive sense when considering that the magnetic bead velocity is an order of magnitude larger than the linear flow velocity.

CHAPTER 7

CONCLUSION

This work has fabricated, demonstrated and tested the use of rotating magnetic beads inside a microfluidic channel. This work provided several innovations in the areas of microfabrication, microfluidic mixing and particle capture.

Microfabrication

Permalloy is not an uncommon material in microfabrication. However, permalloy is often deposited via electroplating if it is to be patterned.[56-58] While this method is well-established electroplating has difficulties with creating high resolution features at scales <10 μm. Additionally, pinholes in the photoresist in the electroplating process can lead to excessive growth of permalloy in regions it is not desired. Additional groups have utilized evaporation at room temperature to create films but these films are often <100nm in thickness. [59-61] Further, these films are often only used for evaluation and are not usually patterned to create an array of features. Other work attempting to micropattern permalloy utilized sputtering to deposit the material combined with wet etching.[62] These methods also have difficulty in creating high resolution small features. Very recent work has demonstrated the capacity to pattern NiFe films utilizing e-beam lithography, sputtering and liftoff.[63] However, e-beam lithography is very expensive and not a widely available tool for MEMS microfabrication. This work has demonstrated the tensile stress inherent in evaporated Ni films that has already been confirmed and measured. [64] This was demonstrated by the peeling of the evaporated NiFe film from the underlying layer when exposed to atmosphere or placed under fluid. This work demonstrated a method for microfabricating permalloy features 3 μm in diameter with high resolution. Further, this was done using standard photolithography techniques,

making it lower cost and more widely accessible by other researchers. Additionally, a method for evaporating a permalloy film without an adhesion layer that could be micropatterned was developed. Previous work has evaporated permalloy films under heating conditions and in the presence of a magnetic field to demonstrate development of magnetic anisotropy.[65] A current literature search has not yet revealed any work demonstrating the micropatterning of an evaporated NiFe film. This method could be made compatible with liftoff if an appropriate mask is used to withstand the elevated temperatures. The new methods for microfabrication developed in this work have already been used by other Georgia Tech Institute for Electronics and Nanotechnology researchers to develop new magnetically actuated microsystems.[66]

Microfluidic Mixing

The physics of low Re flows makes the mixing of two fluids inside a microfluidic channel an ongoing problem. Much work has already been done to develop new techniques to achieve mixing in microfluidic systems.[16, 40] Most of these systems utilize passive mixing techniques. These passive systems stretch and fold the fluid, either by inducing secondary flows inside the main flow or by splitting and recombining flows by use of additional channels. This is primarily done to increase the interface between the two fluids and decreasing the length over which diffusion must occur. The major advantages of these systems are straightforward fabrication and integration with the primary flow. However, passive mixers often require on the order of several millimeters of channel length to achieve significant mixing, which can be a drawback for time-sensitive reactions. Also, a passive mixer cannot be controlled independent of the primary flow rate. It is not possible to tune the mixing on chip because the mixing is purely by the physics and fluid mechanics of the primary flow. As a contrast, active mixers, mixers that utilize some form of actuator to disturb the fluids to induce mixing, can achieve rapid mixing in short channels on the order of 1 mm. Further these systems often make use of

DEP, EOF or ultrasonics which are not compatible with cellular work. This work has demonstrated and quantified the capacity to actuate magnetic beads with a rotating magnetic field. The actuation has been demonstrated to have significant effect on fluid behavior inside a microfluidic channel. This system demonstrated significant mixing of two streams of fluid in <300 μm of channel length. This length is almost an order of magnitude shorter than what is commonly seen for passive mixers and shorter than most active mixers. The capacity to actuate mixing independent of fluid flow was demonstrated as another advantage over common passive microfluidic mixers. In fact, the degree of mixing can be directly tuned by adjusting the rotational velocity of the magnetic field. Finally, the operating frequency is much less than acoustic mixers leading to less chance for heating in the system. The reason permalloy is often used in AC transformers is because its low residual magnetization reduces hysteresis in the feature leading to less heating under a dynamic magnetic field.[46] This property is taken advantage of in the device presented in this work. Finally, the method of actuation of the beads described here is easily integrated with cells and chemical reactions without altering either.

This work demonstrated the effect of varying the geometry of the permalloy features. It was shown that the vertical ellipse had no effect on mixing while the horizontal ellipse could achieve some significant mixing. Based upon numerical modeling performed by a collaborator, Matthew Ballard, transverse streamlines were identified as the reason for the mixing generated by this system. This provides a key piece of evidence in identifying why the horizontal ellipse performed better. First, the horizontal ellipse had a much smaller radius of curvature at the points were the magnetic bead would be moving transverse to the bulk flow. This much smaller radius of curvature combined with the constant rotational frequency gives the bead a much higher linear velocity at those points which could lead to a stronger streamline generation.

Particle Capture

A popular method to manipulate and separate targets in a microfluidic channel is to use ligand functionalized magnetic beads. The functionalization can provide strain specific targeting via immunochemistry. The magnetic beads can then be manipulated on chip via magnetic fields to separate them and the bound targets. However, a gap in the literature exists discussing how to get this magnetic bead onto its target. There has been some work on this subject by Liu et. al. and Saliba et al. [37, 38] However these systems utilize static magnetic beads. The Liu et. al. system uses pillars coated with magnetic beads that occupy 1/5 of the channel height and needs a channel length of 5 cm to achieve 70%-90% capture. The Saliba et. al. system improves the cellular capturing to 80% utilizing chains of magnetic beads that cover almost the entirety of the channel height. However this system still required > 5 mm of channel length to achieve the stated capture efficiency. The system presented in this work hypothesized that actuating the beads would lead to greater mixing of the fluid and as a result of mixing increase the capture efficiency. This increased capture efficiency is the result of more of the fluid having the opportunity to come in contact with the magnetic beads. This would increase the chance of targets in the fluid to become bound to the magnetic beads. In the system of rotating magnetic beads presented here, capture rates have been demonstrated with >90% efficiency in a channel where the beads occupy 0.48 of the total channel height. It was demonstrated that for a short array length, approximately 400 μm, the system is relatively inflexible to the ratio of flow velocity to the magnetic bead linear speed. Across three different geometries, an average trend of -0.46/u was found when operating with u< 0.5. This demonstrates that the greatest chance of capture correlates to low u values. These low u values however must be balanced by considering the rotational velocity of the magnetic bead. Significant captured particle detachment was observed in experiments where the magnetic bead linear velocity was >300 μm/s. Additionally, it was demonstrated that decreasing the spacing between the NiFe features in this design by 2

μm would yield approximately 8% increase in capture efficiency. This factor however also needs to be balanced by excessive clumping of magnetic beads with captured particles in smaller spacing arrays. Finally, it was demonstrated that increasing the channel height had a large effect on the shape of the capture proportion versus *u* curves. When the *u* value dropped below 0.2 for channels with heights three or four times the bead diameter, *h*= 0.30 or 0.23, the capture rate dropped to 20%. This was a rapid drop from the 50% capture rate found for similar *u* values with *h*=0.48. However with $u<0.2$ the capture rate in the *h*=0.30 and *h*=0.23 channels, the capture proportion increases sharply to the same capture rate as seen in the *h*=0.48 channel.

Future Work

This work presents early fabrication, validation and testing of an array of rotating magnetic beads in a microfluidic system. However, many more variables are still available for testing. A first and obvious choice is the modification of the NiFe features themselves. This work presented a fabrication method for evaporating a NiFe film without an underlying adhesion layer. The chamber temperature utilized was 250 °C to achieve this result. Additional work to determine a lower temperature to still achieve the no adhesion layer film could make the system compatible with some photoresists with high glass transition temperatures. This would then allow for fabrication of features via liftoff with no adhesion layer.

Another avenue for future work that needs investigation is the geometry of the array. The system presented here used only 20 columns of NiFe features to actuate the magnetic beads for mixing experiments and as many as 28 columns for capture experiments. The total channel span of the array was never more than 400 μm. Expansion of the array would likely have an improvement on the device functioning In a longer array with more columns of features more magnetic beads could be loaded and produce even greater mixing by providing a longer residence time for the transport of fluid across

the channel via the transverse streamlines. Positioning of the NiFe features closer together could make for easier transport between magnetic microbeads and increase the number of transverse streamlines. This observation was supported by the results seen from the horizontal ellipse data.

The array of rotating magnetic beads also demonstrated capture of particles utilizing a bond between streptavidin and biotin. This system was chosen for the off-the-shelf availability of beads and particles with the protein coating. In order to test the capture ability of this device with cells, new magnetic bead aptamer coatings will need to be developed and tested to bind with cells or other biological targets. These coatings will need to be customized to capture particular strains of bacteria. For example, not every strain of Salmonella is dangerous so antibodies to target specific antigens need to be developed. The physical bond strength of these new coatings would have to also be studied. This work has shown that the binding strength of streptavidin-biotin was not strong enough to withstand some of the inertial forces in this system but this protein-protein bond is well established as one of the strongest and most stable currently known. The bond strength of these new coatings will need to be investigated.

The current work shown was limited by the ability to only capture either fluorescent or bright field images. This made it difficult to monitor both the magnetic beads and the fluorescent particles simultaneously. In future experiments it would be ideal to utilize an optical system capable of capturing both images simultaneously.

Further work could be done to investigate the upper limit for still achieving strong capture with taller and taller channels. A tall channel will allow for high volumetric throughput of the system needed for processing large volumes in a timely manner. Finding the minimum h value, alternatively the maximum channel height, to still achieve capture rates. The new h values will need to be considered for longer arrays as well as different u values.

Finally, additional methods for pumping fluid and actuating the magnetic beads need investigation. The current system of performing capture experiments utilizes a combination of EOF and gravity driven flow and a stationary array with a DC motor over it does not lend itself to portability for point-of-care use. One potential option to overcome the combination of these problems is the integration of a static magnetic field into a CD-microfluidic device. This design would have the array move in relation to the field which would in turn move the magnetic beads inside the channel. This new system would require work re-calibrating the array design to address the orientation of the field, insuring a smooth progress by the beads around the feature.

APPENDIX A

Microfabrication

Wafer Cleaning

1. Obtain a wafer. Either soda lime glass wafer, 100 mm, 500 µm thick double-sided polish, or a silicon <100>, 100 mm, 700 µm, test grade wafer, single side polish.
2. Place wafer in piranha etch solution (4:1 H_2SO_4 to H_2O_2) at 115 °C for 5 minutes to remove any contaminants
3. After 5 minutes, carefully remove wafer from piranha solution. Wait 30 seconds before rinsing with deionized (DI) water. Rinsing the wafer too soon after heated piranha etch can lead to cracking or breaking of the wafer due to thermal stress.
4. Dry wafers with nitrogen air gun. If not used immediately, store vertically in wafer box until needed and clean with nitrogen air gun before use.

Metallization

1. Vent electron-beam evaporator chamber. Remove any excess debris from chamber. Electron-beam evaporator used in this study was the Denton Infinity, in the Georgia Tech Institute for Electronics and Nanotechnology Marcus Nanotechnology Building, Inorganic Cleanroom.
2. Place cleaned and dried wafer into the chamber.
3. Pump down chamber to less than $2*10^{-6}$ mTorr.
4. Program tool to turn on heater and begin heating the chamber. Have the tool heat the chamber to the chosen temperature prior to beginning evaporation. If depositing NiFe without an adhesion layer, heat the chamber to 250 °C prior to evaporation. If performing lift-off fabrication, evaporate Ti (5-10 nm) followed by NiFe, heat chamber to 95 °C prior to evaporation.
5. Program tool for evaporation at 3 angstroms/s deposition rate for NiFe layer (and Ti layer if needed). Ti adhesion layer should 10 nm thick. NiFe layers have been made up to 350 nm thick. Be sure to confirm thickness via another tool to confirm evaporator is achieving correct thickness.
6. Following evaporation, allow chamber to cool to 80 °C prior to venting chamber.
7. Remove wafer from tool, being careful to note which side contains metal. Store vertically in wafer holder.

Photolithography

Photolithography steps were performed utilizing the BLE Spinner for spincoating and the Karl Suss TSA Mask Aligner. Both tools are located in the Georgia Tech Institute for Electronics and Nanotechnology Marcus Nanotechnology Building, Inorganic Cleanroom.

Lift-off Photolithography

1. Spincoat NR9-1500PY resist at 4000 rpm, acceleration 1500rpm/s, total time excluding acceleration and deceleration 40s
2. Bake wafer with resist at 150 °C for 80 seconds in the Thermo Fisher oven in the Marcus cleanroom. Note silicon wafers will rapidly cool after removal from heat. Glass wafers will require longer returning to close to room temperature.
3. Expose at 385nm wavelength, with a dose of 190mJ/cm^2. Measure UV intensity through mask.
4. Post exposure bake at 110°C for 4 min in the same Thermo Fisher oven in the Marcus cleanroom. Note silicon wafers will rapidly cool after removal from heat. Glass wafers will require longer returning to close to room temperature.
5. Place wafer in RD6 resist developer for 12 seconds with gentle agitation. Quickly remove wafer and rinse in DI water for 1.5 min. Dry off with nitrogen gun. Wafer may be stored vertically in wafer box.

Photoresist Mask for Metal Etching

1. Spincoat SC1813 at 3000 rpm, 1000 rpm/s acceleration, for 30s excluding acceleration and deceleration .
2. Place silicon wafer on 110 ºC hotplate for 1 minute. If applying resist to glass wafer with metallization already performed, set hot plate to 115 ºC hotplate and bake wafer for 1 minute.
3. Expose 405nm wavelength with a dose of 180 mJ/cm^2. Measure UV intensity through mask. Note if using glass wafer: be sure to utilize Low-Vacuum Contact Mode to insure good contact between wafer and mask and prevent constructive interference (see Chapter 3). If utilizing silicon wafer, Hard Contact Mode is sufficient.
4. Place wafer in MF319 developer for 1min with gentle agitation or until features are fully developed.
5. Wafer may be stored vertically in wafer box.

Silicon Dioxide PECVD

Silicon dioxide was deposited over the entire wafer (both glass and silicon) utilizing the Oxford PECVD Right, located in the Georgia Tech Institute for Electronics and Nanotechnology Marcus Nanotechnology Building, Inorganic Cleanroom. The standard 250 ºC recipe on the tool was used. A deposition time of 90s was experimentally determined to produce a 180nm thick layer of SiO_2. Care must be taken when removing the wafer so as to not thermally shock and crack the wafer. The SiO_2 layer was strengthened via annealing utilizing the Lindbergh Furnace Polymer-curing tube in the Georgia Tech Institute for Electronics and Nanotechnology Joseph M. Pettit Microelectronics Research Center Cleanroom. The procedure utilized was annealing for 30 minutes at 300 ºC, with a 2 ºC/minute heating rate and a 20 ºC/minute cooling rate specified for the tool. Actual cooling inside the tube will take hours and entire annealing process is recommended run overnight.

SU-8 250 µm Tall Channels

SU-8 Photoresist is very viscous in general and SU-8 2100 is especially viscous. This can lead to difficulties getting precise thicknesses. The complicated interplay of volume of material and spin speed can be difficult to control. While higher speeds might intuitively give thinner photoresist thicknesses, SU-8 will actually increase its resistance to flow with increasing shear-rates. Since it is often used for creating specific features heights to use in PDMS molding this can led to trial and error. It is recommended to avoid features that are near the bottom of the particular SU-8 resist thickness profile. If SU-8 must be removed from a wafer, utilize piranha etch solution (4 parts H_2SO_4 : 1 part 30% H_2O_2). This will remove resist but will also sometimes leave faint outline of removed resist.

1. Spin coat with SU-8 2100 at 500 rpm for 7 sec (not including100 rpm/s acceleration) and then at 1200 rpm for 30 sec (not including 300 rpm/s)
2. Prebake the wafer at 72 °C (start from the room temperature and ramp it up to 72 °C at 60 °C /hr rate) for 8 hours. Let it cool down to room temperature on its own.
3. Expose the wafer at 360 mJ/cm^2.
4. Post bake at 90 °C. Utilizing the same ramp scheme for step 2.
5. Place wafer in SU-8 Developer with gentle agitation. Watch for removal of SU-8 resist. This may take as many as 30 minutes.

APPENDIX B

Device Assembly & Experimental Procedure

PDMS Molding

Polydimethylsiloxane (PDMS) is a silicone based organic polymer. It is commonly used in creation of microfluidic channels via molding utilizing a microfabricated master. Typically this master is created via SU-8 photolithography on a silicon wafer. A commercial name for PDMS is Sylgard 184. Sylgard 184 comes in two pieces, a base and a crosslinker. The exact ratio of base to crosslinker affects the stiffness of the final PDMS structure.

1. Put a 10:1 ratio (by volume) of base to crosslinker in a disposable dish. Mix the base and crosslinker for 5 minutes.
2. Pour mixture over master. Place under vacuum to remove bubbles.
3. After removing bubbles, PDMS can fully cure after 1 hour in 80 ºC oven for large volumes (~10 mL). Small volumes (<1 mL) can cure in 5 minutes on a hot plate. If left at room temperature the PDMS will almost fully cure overnight. Placing the PDMS mixture at 4 ºC will slow the curing.

Pressure Driven Flow Device

1. After the NiFe features have been deposited onto a silicon wafer, dice the wafer into appropriate chips.
2. Cut microfluidic channel out of molded PDMS.
3. Place PDMS microfluidic channel onto chip, insuring NiFe features are placed in the microfluidic channel by utilizing a dissecting microscope. Natural adhesion of PDMS will hold it in place.
4. Insert tubing into side channels. Smear a small droplet of sealant to hold tubing in place. Sealant can either be uncured mixture of PDMS or UV crosslinked epoxy. After smearing drop of sealant, pay close observation and cure sealant after ½ of inserted tubing (or sooner if sealant has low viscosity) is covered by sealant. Immediately cure the sealant, either by placing the entire chip onto an 80 ºC hotplate if using PDMS or by UV light.
5. Passivate system by pumping in 0.1% Pluronics F127 in PBS solution into the device via one tube. Keep other tubes open to atmosphere and insure bubbles of fluid form at them. This indicates the entire system is exposed to the Pluronics solution. Leave to incubate in channel for 1 hour.
6. Begin pumping in magnetic beads into system. Have overhanging magnet already spinning at 20000rpm. This will help break up clumps of magnetic beads. As low a flow rate as possible is recommended (0.05 µL/min was typically utilized).
7. Repositioning of rotating magnet is often required to fully distribute magnetic beads across the array. This is because the magnet is not positioned in relation to the chip automatically.

8. Once array has been filled with magnetic beads begin pumping in experimental fluids.

Electro-Osmotic Flow Device

Device Assembly

1. Cut microfluidic channel out of molded PDMS. Puncture holes in microfluidic channel sheet using biopsy punch.
2. Place PDMS microfluidic channel onto chip, insuring NiFe features are placed in the microfluidic channel by utilizing a dissecting microscope. Natural adhesion of PDMS will hold it in place.
3. To passivate channel, fill one reservoir with a 0.1% (w/v) BSA in DI H_2O. If the wafer is pre-treated with oxygen plasma, the fluid should rapidly fill the channel via capillary forces. Pressurizing the reservoir by pressing on it can help pump the fluid into the channel. Once the fluid has reached the other reservoirs, fill those as well with the 0.1% BSA in DI H_2O solution. Leave to incubate for 1 hour.
4. Add 1-3 L of a 1:10 dilution of M-280 magnetic beads stock solution to bead loading reservoir.
5. Add electrodes to reservoirs and begin pumping magnetic beads. Voltages required will vary depending on channel conditions but for these experiments 250V was typically used. The amperage of the system should be low (<0.01 mA). If it is not, there is a problem in the system.
6. Repositioning of rotating magnet is often required to fully distribute magnetic beads across the array. This is because the magnet is not positioned in relation to the chip automatically.
7. After magnetic beads are loaded, stop voltage and remove 50% of fluid from M-280 bead loading reservoir. This will create a gravity driven flow to force any excess magnetic beads back towards the loading reservoir.
8. Add solutions as needed to reservoirs as needed depending on experiment.

Mixing Experiment

Remove solution form one of the inlet reservoirs and add in 1:10 dilution of 40nm Fluorspheres in 0.1% BSA in DI H_2O. (Note: carboxylate-modified 40nm Fluorspheres will not pump correctly via EOF. Carboxylate-modified particles will pump correctly for a few seconds before reversing flow and pumping towards the positive terminal.) Use a single positive electrode split between the two inlet reservoirs for pumping. A voltage of 30 V was typically used. Balancing the two flows is not easy. It can be tweaked by adding or decreasing the volumes in the reservoir. Continually tweak until fluids are near balanced and then begin recording images. Take multiple images spaced 3 seconds apart for repeated measurements. The raw images are rotated if needed and cropped into a standard size, 66 pixels (approximately 20 μm down the channel) by 225 pixels (the width of the channel). These images are imported into MATLAB for quantitative analysis (see Appendix C).

Capture Experiments

Create a 1:1000 of 1 μm Fluorspheres with biotin surface modification in PBS with 0.1% (v/v) Tween-20. Empty one inlet reservoir and overfill the reservoir. This work used a 5

mm biopsy punch to create the reservoir and added 40 µL to the reservoir to over fill it. This yielded flow velocities on the order of 20 µm/s. Wait for gravity to pump the fluorescent particles to the array and being taking time-lapse images. The images in this work were recorded using a Photometrics Cool Snap HQ camera utilizing Nikon Elements software. The time lapse images were recorded ~2 frames/second. The approximation is due to weaknesses in the computer processing capacity but is overcome because the recorded images are stored with a time-stamp in the .nd2 format. This file format, .nd2, can be read into ImageJ via a readily available plugin. Capture rates were determined from manually counting the number of fluorescent particles entered the array and the number of fluorescent particles that had the opportunity to exit the array.

APPENDIX C

Mixing MATLAB Analysis Code

Images are cropped into a standard size as described in Appendix B. Two sets of code are used, one to create a single composite curve from the multiple images at each experimental condition, the second to measure the mixing degree from each individual image. The code looks similar for each and both are presented here. The example given is for creation of the circular geometry data.

Creation of Composite Curve Plots

Importing Images and Creation of Composite Curve

```
clear
clc
%%
%import image files
%loads the images as a double
I_in_raw1=cast(imread('3000rpm_200ms_1_pre.jpg'),'double');
I_out_raw1=cast(imread('3000rpm_200ms_1_post.jpg'),'double');
I_in_raw2=cast(imread('3000rpm_200ms_2_pre.jpg'),'double');
I_out_raw2=cast(imread('3000rpm_200ms_2_post.jpg'),'double');
I_in_raw3=cast(imread('3000rpm_200ms_3_pre.jpg'),'double');
I_out_raw3=cast(imread('3000rpm_200ms_3_post.jpg'),'double');
I_in_raw4=cast(imread('3000rpm_200ms_4_pre.jpg'),'double');
I_out_raw4=cast(imread('3000rpm_200ms_4_post.jpg'),'double');
I_in_raw5=cast(imread('3000rpm_200ms_5_pre.jpg'),'double');
I_out_raw5=cast(imread('3000rpm_200ms_5_post.jpg'),'double');
I_in_raw6=cast(imread('3000rpm_200ms_6_pre.jpg'),'double');
I_out_raw6=cast(imread('3000rpm_200ms_6_post.jpg'),'double');

%%
for i=1:size(I_in_raw1,1);

    I_intotal(i)=
(mean(I_in_raw1(i,:))+mean(I_in_raw2(i,:))+mean(I_in_raw3(i,:))+mean(I_
in_raw4(i,:))+mean(I_in_raw5(i,:))+mean(I_in_raw6(i,:)))/6;
end
for j=1:size(I_out_raw1,1);
    I_outtotal(j)= (mean(I_out_raw1(j,:))+
mean(I_out_raw2(j,:))+mean(I_out_raw3(j,:))+mean(I_out_raw4(j,:))+mean(
I_out_raw5(j,:))+mean(I_out_raw6(j,:)))/6;
end
%%
if min(I_intotal)>min(I_outtotal);
    I_inmin=I_intotal-min(I_intotal);
    I_outmin=I_outtotal-min(I_outtotal);
elseif min(I_intotal)<min(I_outtotal);
    I_inmin=I_intotal-min(I_intotal);
    I_outmin=I_outtotal-min(I_outtotal);
else
```

```
    I_inmin=I_intotal-min(I_intotal);
    I_outmin=I_outtotal-min(I_outtotal);
end
%%
if mean(I_inmin)>mean(I_outmin);
    I_infinal=I_inmin*mean(I_outmin)/mean(I_inmin);
    I_outfinal=I_outmin;
elseif mean(I_inmin)<mean(I_outmin);
    I_outfinal=I_outmin*mean(I_inmin)/mean(I_outmin);
    I_infinal=I_inmin;
else

end

I_out_3000rpm=I_outfinal;
I_in_3000rpm=I_infinal;
Save('3000RPM.mat','I_out_3000rpm',I_in_3000rpm')
```

Scaling of Curves and Creation of Composite Curves Plot

```
%%Read in previously saved data
load('3000rpm.mat')
load('0rpm.mat')
load('1500rpm.mat')
load('1500rpm-1.mat')
load('2000rpm.mat')
%%
   %It has previously been determined that I_3000rpm_out has the
   %smallest total area.
    I_1500rpmout=I_out_1500rpm*mean(I_out_3000rpm)/mean(I_out_1500rpm);
    I_0rpmout=I_out_0rpm*mean(I_out_3000rpm)/mean(I_out_0rpm);
    I_3000rpmout=I_out_3000rpm;
    I_15001rpmout=I_out_1500*mean(I_out_3000rpm)/mean(I_out_1500);
    I_2000rpmout=I_out_2000*mean(I_out_3000rpm)/mean(I_out_2000);
%%
max_out=max([max(I_0rpmout),max(I_1500rpmout),max(I_3000rpmout),
max(I_15001rpmout), max(I_2000rpmout)]);
I_3000=I_3000rpmout./max_out;
I_1500=I_1500rpmout./max_out;
I_0=I_0rpmout./max_out;
I_1501=I_15001rpmout./max_out;
I_2000=I_2000rpmout./max_out;

%%
plot([1:1:length(I_0)]*150/length(I_0),I_0)
hold on
plot([1:1:length(I_1500)]*150/length(I_1500),I_1500)
plot([1:1:length(I_1501)]*150/length(I_1501),I_1501)
plot([1:1:length(I_2000)]*150/length(I_2000),I_2000)
plot([1:1:length(I_3000)]*150/length(I_3000),I_3000)
legend('U/Vb=4.8 (n=1)','U/Vb=0.15 (n=6)','U/Vb=0.11 (n=6)','U/Vb=0.08
(n=6)','U/Vb=0.04 (n=6)')
xlabel('Channel Width (microns)')
ylabel('Fluorescent Intensity')
```

Calculation of Mixing Degree of Individual Images

Importing of Images and Creation of Curve

```
clear
clc
%%
%import image files
%loads the images as a double

I_in_raw1=cast(imread('3000rpm_200ms_1_prearray.tif'),'double');
I_out_raw1=cast(imread('3000rpm_200ms_1_postarray.tif'),'double');

%%
for i=1:size(I_in_raw1,1);
    I_intotal(i)= (mean(I_in_raw1(i,:)));
end
for j=1:size(I_out_raw1,1);
    I_outtotal(j)= (mean(I_out_raw1(j,:)));
end
%%
if min(I_intotal)>min(I_outtotal);
    I_inmin=I_intotal-min(I_intotal);
    I_outmin=I_outtotal-min(I_outtotal);
elseif min(I_intotal)<min(I_outtotal);
    I_inmin=I_intotal-min(I_intotal);
    I_outmin=I_outtotal-min(I_outtotal);
else
    I_inmin=I_intotal-min(I_intotal);
    I_outmin=I_outtotal-min(I_outtotal);
end
%%
if mean(I_inmin)>mean(I_outmin);
    I_infinal=I_inmin*mean(I_outmin)/mean(I_inmin);
    I_outfinal=I_outmin;
elseif mean(I_inmin)<mean(I_outmin);
    I_outfinal=I_outmin*mean(I_inmin)/mean(I_outmin);
    I_infinal=I_inmin;
else

end

I_out=I_outfinal;
I_in=I_infinal;
save('0p04-1.mat', 'I_in','I_out') %saves recorded curve for evaluation
%in separate piece of code. The title of the .mat file needs to be
%changed for
```

Calculation of Mixing Degree

```
clear
clc
clear
counter=0;
% This piece of code can be repeated in a single script to create a
%single vector containing all of the mixing degree values.
load('0p04-1.mat')
counter =counter+1;
```

```
%the 10.9232 is the same scaling performed in the composite curves to
%create composite curves with the same area. In the composite curves
this
%is done by scaling by mean(I_out_3000rpm), the value of which is
10.9232.
I_out2=I_out*10.9232/mean(I_out)
%The 31.4043 is the max from I_out_0rpm curve and is used to scale all
the
%curves on the same axis.
I_outscale=I_out2./31.4043;
%%
mixed=mean(I_outscale);%
sig=sqrt(mean((I_outscale-
mixed*ones(size(I_outscale,1),size(I_outscale,2))).^2));
md(counter)=1-2*sig
```

APPENDIX D

Capture Significance R Code

Data from the capture experiments was imported into R (version 3.2.3) for analysis to determine significance. Below is an example of the typical code used for analysis. The third (and sometimes fourth) column represents a factor that categorizes the data into different groups. In some analysis, a single data set would be proved significantly different from the other two sets. The meta group of the tow similar datasets were joined into a single group and compared to the other using another category signifier.

Code to determine buffer significance

```
> library(xlsx)
Loading required package: rJava
Loading required package: xlsxjars
> mybuffer <- read.xlsx("buffer.xlsx", 1)
> class(mybuffer$buffer)
[1] "factor"
> fitbuffer = lm(capture ~ u+buffer, data=mybuffer)
> anova(fitbuffer)
Analysis of Variance Table

Response: capture
          Df  Sum Sq  Mean Sq F value  Pr(>F)
u          1 0.06775 0.067749  1.7213 0.19982
buffer     2 0.23010 0.115048  2.9230 0.06975 .
Residuals 29 1.14143 0.039360
---
Signif. codes:  0 ‘***’ 0.001 ‘**’ 0.01 ‘*’ 0.05 ‘.’ 0.1 ‘ ’ 1
```

Code for determining significance of spacing

```
> library(xlsx)
Loading required package: rJava
Loading required package: xlsxjars
myspacing <- read.xlsx("capture.xlsx", 1)
> class(myspacing$spacing)
[1] "factor"
> head(myspacing)
            u   capture  spacing
1 0.009682174 0.5454545 fourteen
2 0.016951377 0.6065574 fourteen
3 0.020915851 0.5250000 fourteen
4 0.030046788 0.8000000 fourteen
5 0.049371893 0.5714286 fourteen
6 0.053217560 0.5416667 fourteen
> tail(myspacing)
           u   capture spacing
34 0.1125509 0.7931034   eight
35 0.1935600 0.5833333   eight
36 0.2109010 0.8055556   eight
```

```
37 0.3054697 0.6341463   eight
38 0.3887573 0.7500000   eight
39 0.9769976 0.5857143   eight

> fitspacing = lm(capture ~ u+spacing, data=myspacing)
> anova(fitspacing)
Analysis of Variance Table

Response: capture
          Df  Sum Sq  Mean Sq F value    Pr(>F)
u          1 0.04762 0.047618  3.5642   0.06735 .
spacing    2 0.49204 0.246018 18.4146 3.435e-06 ***
Residuals 35 0.46760 0.013360
---
Signif. codes:  0 ‘***’ 0.001 ‘**’ 0.01 ‘*’ 0.05 ‘.’ 0.1 ‘ ’ 1
> summary(fitspacing)

Call:
lm(formula = capture ~ u + spacing, data = myspacing)

Residuals:
     Min       1Q   Median       3Q      Max
-0.23782 -0.06382  0.00093  0.04118  0.35692

Coefficients:
                Estimate Std. Error t value Pr(>|t|)
(Intercept)      0.83144    0.04460  18.642  < 2e-16 ***
u               -0.34886    0.10524  -3.315  0.00214 **
spacingfourteen -0.27235    0.04618  -5.897 1.05e-06 ***
spacingten      -0.11693    0.05349  -2.186  0.03559 *
---
Signif. codes:  0 ‘***’ 0.001 ‘**’ 0.01 ‘*’ 0.05 ‘.’ 0.1 ‘ ’ 1

Residual standard error: 0.1156 on 35 degrees of freedom
Multiple R-squared:  0.5358,   Adjusted R-squared:  0.496
F-statistic: 13.46 on 3 and 35 DF,  p-value: 5.312e-06
> myspacing2<-myspacing[myspacing$spacing!="eight",]
> head(myspacing2)
           u   capture  spacing
1 0.009682174 0.5454545 fourteen
2 0.016951377 0.6065574 fourteen
3 0.020915851 0.5250000 fourteen
4 0.030046788 0.8000000 fourteen
5 0.049371893 0.5714286 fourteen
6 0.053217560 0.5416667 fourteen
> tail(myspacing2)
           u   capture spacing
24 0.07139238 0.8666667     ten
25 0.16095727 0.7826087     ten
26 0.19081172 0.6250000     ten
27 0.20357752 0.7142857     ten
28 0.44077737 0.5000000     ten
29 0.44408160 0.4444444     ten
> fitspacing2 = lm(capture ~ u+spacing, data=myspacing2)
> anova(fitspacing2)
Analysis of Variance Table
```

```
Response: capture
          Df  Sum Sq  Mean Sq F value   Pr(>F)
u          1 0.08039 0.080391  5.4887 0.027067 *
spacing    1 0.15929 0.159288 10.8753 0.002824 **
Residuals 26 0.38081 0.014647
---
Signif. codes:  0 ‘***’ 0.001 ‘**’ 0.01 ‘*’ 0.05 ‘.’ 0.1 ‘ ’ 1
```

REFERENCES

[1] N.T. Thanh, Magnetic Nanoparticles: from Fabrication to Clinical Applications: CRC press; 2012.

[2] L. Zhang, S. Qiao, Y. Jin, H. Yang, S. Budihartono, F. Stahr, et al., Fabrication and size-selective bioseparation of magnetic silica nanospheres with highly ordered periodic mesostructure, Advanced Functional Materials, 18(2008) 3203-12.

[3] E.G. Castro, R.V. Salvatierra, W.H. Schreiner, M.M. Oliveira, A.J. Zarbin, Dodecanethiol-stabilized platinum nanoparticles obtained by a two-phase method: Synthesis, characterization, mechanism of formation, and electrocatalytic properties, Chemistry of Materials, 22(2009) 360-70.

[4] S.E. Eklund, D.E. Cliffel, Synthesis and catalytic properties of soluble platinum nanoparticles protected by a thiol monolayer, Langmuir, 20(2004) 6012-8.

[5] J. Chen, B. Lim, E.P. Lee, Y. Xia, Shape-controlled synthesis of platinum nanocrystals for catalytic and electrocatalytic applications, Nano Today, 4(2009) 81-95.

[6] C. Ruffert, N.C. Bigall, A. Feldhoff, L. Rissing, Investigations on the separation of platinum nanoparticles with magnetic beads, Magnetics, IEEE Transactions on, 50(2014) 1-4.

[7] L.-M. Fu, R.-J. Yang, C.-H. Lin, Y.-J. Pan, G.-B. Lee, Electrokinetically driven micro flow cytometers with integrated fiber optics for on-line cell/particle detection, Analytica Chimica Acta, 507(2004) 163-9.

[8] T. Kamei, N.M. Toriello, E.T. Lagally, R.G. Blazej, J.R. Scherer, R.A. Street, et al., Microfluidic Genetic Analysis with an Integrated a-Si:H Detector, Biomed Microdevices, 7(2005) 147-52.

[9] M. Tabuchi, M. Ueda, N. Kaji, Y. Yamasaki, Y. Nagasaki, K. Yoshikawa, et al., Nanospheres for DNA separation chips, Nat Biotech, 22(2004) 337-40.

[10] A.D. Stroock, S.K. Dertinger, A. Ajdari, I. Mezić, H.A. Stone, G.M. Whitesides, Chaotic mixer for microchannels, Science, 295(2002) 647-51.

[11] Y.Z. Liu, B.J. Kim, H.J. Sung, Two-fluid mixing in a microchannel, International Journal of Heat and Fluid Flow, 25(2004) 986-95.

[12] D. Therriault, S.R. White, J.A. Lewis, Chaotic mixing in three-dimensional microvascular networks fabricated by direct-write assembly, Nat Mater, 2(2003) 265-71.

[13] V. Mengeaud, J. Josserand, H.H. Girault, Mixing processes in a zigzag microchannel: finite element simulations and optical study, Analytical chemistry, 74(2002) 4279-86.

[14] B. He, B.J. Burke, X. Zhang, R. Zhang, F.E. Regnier, A picoliter-volume mixer for microfluidic analytical systems, Analytical Chemistry, 73(2001) 1942-7.

[15] J. Melin, G. Giménez, N. Roxhed, W. van der Wijngaart, G. Stemme, A fast passive and planar liquid sample micromixer, Lab on a Chip, 4(2004) 214-9.

[16] C.-Y. Lee, C.-L. Chang, Y.-N. Wang, L.-M. Fu, Microfluidic mixing: a review, International journal of molecular sciences, 12(2011) 3263-87.

[17] C.-H. Lin, L.-M. Fu, Y.-S. Chien, Microfluidic T-form mixer utilizing switching electroosmotic flow, Analytical chemistry, 76(2004) 5265-72.

[18] X. Niu, Y.-K. Lee, Efficient spatial-temporal chaotic mixing in microchannels, Journal of Micromechanics and Microengineering, 13(2003) 454.

[19] M. Campisi, D. Accoto, F. Damiani, P. Dario, A soft-lithographed chaotic electrokinetic micromixer for efficient chemical reactions in lab-on-chips, Journal of Micro-Nano Mechatronics, 5(2009) 69-76.

[20] G.G. Yaralioglu, I.O. Wygant, T.C. Marentis, B.T. Khuri-Yakub, Ultrasonic mixing in microfluidic channels using integrated transducers, Analytical Chemistry, 76(2004) 3694-8.

[21] Z. Yang, S. Matsumoto, H. Goto, M. Matsumoto, R. Maeda, Ultrasonic micromixer for microfluidic systems, Sensors and Actuators A: Physical, 93(2001) 266-72.

[22] R.H. Liu, R. Lenigk, R.L. Druyor-Sanchez, J. Yang, P. Grodzinski, Hybridization enhancement using cavitation microstreaming, Analytical Chemistry, 75(2003) 1911-7.

[23] A. Venancio-Marques, F. Barbaud, D. Baigl, Microfluidic mixing triggered by an external LED illumination, Journal of the American Chemical Society, 135(2013) 3218-23.

[24] M.J. Tomlinson, S. Tomlinson, X.B. Yang, J. Kirkham, Cell separation: Terminology and practical considerations, Journal of tissue engineering, 4(2013) 2041731412472690.

[25] H.M. Ji, V. Samper, Y. Chen, C.K. Heng, T.M. Lim, L. Yobas, Silicon-based microfilters for whole blood cell separation, Biomed Microdevices, 10(2008) 251-7.

[26] J.A. Davis, D.W. Inglis, K.J. Morton, D.A. Lawrence, L.R. Huang, S.Y. Chou, et al., Deterministic hydrodynamics: taking blood apart, Proceedings of the National Academy of Sciences, 103(2006) 14779-84.

[27] G. Wang, W. Mao, R. Byler, K. Patel, C. Henegar, A. Alexeev, et al., Stiffness dependent separation of cells in a microfluidic device, PLoS One, 8(2013) e75901.

[28] S.S. Kuntaegowdanahalli, A.A.S. Bhagat, G. Kumar, I. Papautsky, Inertial microfluidics for continuous particle separation in spiral microchannels, Lab on a Chip, 9(2009) 2973-80.

[29] C.-H. Lin, C.-Y. Lee, C.-H. Tsai, L.-M. Fu, Novel continuous particle sorting in microfluidic chip utilizing cascaded squeeze effect, Microfluidics and nanofluidics, 7(2009) 499-508.

[30] Z. Wu, B. Willing, J. Bjerketorp, J.K. Jansson, K. Hjort, Soft inertial microfluidics for high throughput separation of bacteria from human blood cells, Lab on a Chip, 9(2009) 1193-9.

[31] Z. Wang, S.Y. Chin, C.D. Chin, J. Sarik, M. Harper, J. Justman, et al., Microfluidic CD4+ T-cell counting device using chemiluminescence-based detection, Analytical chemistry, 82(2009) 36-40.

[32] Y. Xu, J.A. Phillips, J. Yan, Q. Li, Z.H. Fan, W. Tan, Aptamer-based microfluidic device for enrichment, sorting, and detection of multiple cancer cells, Analytical chemistry, 81(2009) 7436-42.

[33] U. Dharmasiri, S. Balamurugan, A.A. Adams, P.I. Okagbare, A. Obubuafo, S.A. Soper, Highly efficient capture and enumeration of low abundance prostate cancer cells using prostate-specific membrane antigen aptamers immobilized to a polymeric microfluidic device, Electrophoresis, 30(2009) 3289-300.

[34] J.P. Gleghorn, E.D. Pratt, D. Denning, H. Liu, N.H. Bander, S.T. Tagawa, et al., Capture of circulating tumor cells from whole blood of prostate cancer patients using geometrically enhanced differential immunocapture (GEDI) and a prostate-specific antibody, Lab on a chip, 10(2010) 27-9.

[35] J.H. Kang, S. Krause, H. Tobin, A. Mammoto, M. Kanapathipillai, D.E. Ingber, A combined micromagnetic-microfluidic device for rapid capture and culture of rare circulating tumor cells, Lab on a Chip, 12(2012) 2175-81.

[36] N.M. Karabacak, P.S. Spuhler, F. Fachin, E.J. Lim, V. Pai, E. Ozkumur, et al., Microfluidic, marker-free isolation of circulating tumor cells from blood samples, Nature protocols, 9(2014) 694-710.

[37] Y.J. Liu, S.S. Guo, Z.L. Zhang, W.H. Huang, D. Baigl, M. Xie, et al., A micropillar-integrated smart microfluidic device for specific capture and sorting of cells, Electrophoresis, 28(2007) 4713-22.

[38] A.-E. Saliba, L. Saias, E. Psychari, N. Minc, D. Simon, F.-C. Bidard, et al., Microfluidic sorting and multimodal typing of cancer cells in self-assembled magnetic arrays, Proceedings of the National Academy of Sciences, 107(2010) 14524-9.

[39] V. Hessel, H. Löwe, F. Schönfeld, Micromixers—a review on passive and active mixing principles, Chemical Engineering Science, 60(2005) 2479-501.

[40] E.A. Mansur, Y. Mingxing, W. Yundong, D. Youyuan, A state-of-the-art review of mixing in microfluidic mixers, Chinese Journal of Chemical Engineering, 16(2008) 503-16.

[41] V.N. Luk, G.C. Mo, A.R. Wheeler, Pluronic additives: a solution to sticky problems in digital microfluidics, Langmuir, 24(2008) 6382-9.

[42] S. Hanasoge, R. Devendra, F.J. Diez, G. Drazer, Electrokinetically driven deterministic lateral displacement for particle separation in microfluidic devices, Microfluidics and Nanofluidics, 18(2015) 1195-200.

[43] S. Hanasoge, F.J. Diez, Vortex chain formation in regions of ion concentration polarization, Lab Chip, 15(2015) 3549-55.

[44] G. Yin, Z. Liu, J. Zhan, F. Ding, N. Yuan, Impacts of the surface charge property on protein adsorption on hydroxyapatite, Chemical Engineering Journal, 87(2002) 181-6.

[45] W.F. Brown, Handbook of Chemistry and Physics: McGraw-Hill; 1958.

[46] W.T. MCLYMAN, Transformer and Inductor Handbook, 3 ed., Idlwild, CA: Marcel Dekker; 2004.

[47] E. Klokholm, J. Freedman, Magnetostress effects in evaporated Ni films, Journal of Applied Physics, 38(1967) 1354-6.

[48] D. Owen, W. Mao, A. Alexeev, J. Cannon, P. Hesketh, Microbeads for Sampling and Mixing in a Complex Sample, Micromachines, 4(2013) 103-15.

[49] L.-H. Lu, K.S. Ryu, C. Liu, A magnetic microstirrer and array for microfluidic mixing, Microelectromechanical Systems, Journal of, 11(2002) 462-9.

[50] T.J. Johnson, D. Ross, L.E. Locascio, Rapid microfluidic mixing, Analytical chemistry, 74(2002) 45-51.

[51] S. Oberti, A. Neild, T.W. Ng, Microfluidic mixing under low frequency vibration, Lab on a Chip, 9(2009) 1435-8.

[52] G.H. Seong, R.M. Crooks, Efficient mixing and reactions within microfluidic channels using microbead-supported catalysts, Journal of the American Chemical Society, 124(2002) 13360-1.

[53] S.-C. Wang, Y.-W. Lai, Y. Ben, H.-C. Chang, Microfluidic mixing by dc and ac nonlinear electrokinetic vortex flows, Industrial & engineering chemistry research, 43(2004) 2902-11.

[54] W.T. van den Beld, N.L. Cadena, J. Bomer, E.L. de Weerd, L. Abelmann, A. van den Berg, et al., Bidirectional microfluidic pumping using an array of magnetic Janus microspheres rotating around magnetic disks, Lab on a Chip, (2015).

[55] J. Wong, A. Chilkoti, V.T. Moy, Direct force measurements of the streptavidin–biotin interaction, Biomolecular engineering, 16(1999) 45-55.

[56] H.J. Cho, K.W. Oh, C.H. Ahn, P. Boolchand, T.-C. Nam, Stress analysis of silicon membranes with electroplated permalloy films using Raman scattering, Magnetics, IEEE Transactions on, 37(2001) 2749-51.

[57] R. Anthony, C. O'Mathúna, J.F. Rohan, MEMS based electrochemical process for fabrication of laminated micro-inductors on silicon, Microelectronic Engineering, 155(2016) 33-8.

[58] M.Z. Ahmed, M. Bhuyan, A.T. Islam, B.Y. Majlis, Design and fabrication of a MEMS 3D micro-transformer for low frequency applications, Asian Journal of Scientific Research, 8(2015) 237-44.

[59] Y. Wei, S. Akansel, T. Thersleff, I. Harward, R. Brucas, M. Ranjbar, et al., Exponentially decaying magnetic coupling in sputtered thin film FeNi/Cu/FeCo trilayers, Applied Physics Letters, 106(2015) 042405.

[60] H. Matsuyama, D. Nara, R. Kageyama, K. Honda, T. Sato, K. Kusanagi, et al., Spin-polarized scanning tunneling microscopy experiments on the rough surface of a polycrystalline NiFe film with a fine magnetic tip sensitive to a well-defined magnetization component, AIP Advances, 6(2016) 035122.

[61] P. Jiang, Y.K. Koh, Accurate measurements of cross-plane thermal conductivity of thin films by dual-frequency time-domain thermoreflectance (TDTR), arXiv preprint arXiv:151104852, (2015).

[62] G.C. Hartman, R. Fitch, Y. Zhuang, Nonreciprocal magnetostatic wave propagation in micro-patterned NiFe thin films, Microwave and Wireless Components Letters, IEEE, 24(2014) 484-6.

[63] B.K. Kuanr, L.M. Malkinski, M. Yu, D. Scherer, R. Camley, Z. Celinski, Dynamic study on Nanometer size square Permalloy (NiFe) antidot arrays; use as Monolithic Microwave localize band-pass filter, une, 13(2016) 15.

[64] M. Hemmous, A. Layadi, A. Guittoum, N. Souami, M. Mebarki, N. Menni, Structure, surface morphology and electrical properties of evaporated Ni thin films: Effect of substrates, thickness and Cu underlayer, Thin Solid Films, 562(2014) 229-38.

[65] D.O. Smith, M.S. Cohen, G.P. Weiss, Oblique-incidence anisotropy in evaporated permalloy films, Journal of Applied Physics, 31(1960) 1755-62.

[66] S. Hanasoge, D. Owen, M. Ballard, P.J. Hesketh, A. Alexeev, Magnetically actuated cilia for microfluidic manipulation, Bulletin of the American Physical Society, 60(2015).

VITA

DREW L. OWEN

OWEN received his BS in Mechanical Engineering, MS in Bioengineering and PhD from Georgia Tech. He was a Sam Nunn Security Program Fellow in 2014. When he is not working, he enjoys testing himself in board games and rugby.